Report of Master Thesis
Lift Coefficient of an Accelerating Wing with Ground Effect
ME55035 2022/2023

B.Eng Shanwei Zhou - 5563526

Supervisors:

Prof.dr.ir. Jerry Westerweel

Ing. E.F.J. (Edwin) Overmars

Process and Energy Department

University of Technology Delft

Delft, August 2023

Acknowledgement

This research is done with a great help of my supervisors: Prof.dr.ir. Jerry Westerweel and Ing. E.F.J. (Edwin) Overmars, who are involved in the whole process of the research.

Apart from my supervisors, brilliant advice is also given by colleges in 3ME: Dr.ir. M. J. B. M. Pourquie, G. Mulder, G. Jacobi, Jesse Reijtenbagh, Nicola Savelli, Tzu-Yao Huang and Ning Ji.

Also, thanks to the financial and moral support from my family members.

Abstract

A F1 car is always in a dynamic flow when racing. The most common case would be acceleration, deceleration and turning a corner. Due to the new rule by FIA since 2021, ground effect is much more significant for F1 car. Limited by the experimental set-up of F1 teams, flow under the car and accelerating flow are hard to be measured quantitatively.

This research is on an accelerating wing with ground effect. The airfoil representing the front wing is from a real F1 car, the Tyrrell 026. Prediction of downforce and flow field in steady phase was done by conformal mapping (potential flow theory), SST $k-\omega$ and 2D-DES CFD simulation. A force and PIV measurement was done to investigate the dynamic flow behaviour.

The connection between force and flow field was discussed, considering the measured residual force and the added mass force. A conclusion is drawn with suggestion on setting the optimal clearance of an F1 car's front wing on track, to improve the racing performance of the car.

Keywords: PIV, Ground Effect, Accelerating Flow, Added Mass Matrix

Nomenclature

Abbreviations

f plane Virtual Plane

Y plane Physical Plane

2D Two Dimensional

3D Three Dimensional

AOA Angle of Attack

CFD Computational Fluid Dynamics

DES Detached Eddy Simulation

F/T transducer Force/Torque transducer

F1 Formula One

FIA Fédération Internationale de l'Automobile / International Automobile Federation

KERS Kinetic Energy Recovery System

PDF Probability Density Function

PIV Particle Image Velocimetry

PSP Pressure Sensitive Paint

R.M.S.E. Root Mean Square Error

RANS Reynolds-Averaged Navier–Stokes equations

SST Shear Stress Transport

TSP Temperature Sensitive Paint

WFGC Warped Face Gradient Correction

Greek Variables

α	Angle of mean flow velocity	rad
β	Angle between vector from center of circle to the point corresponding trailing edge and real axis in f plane	rad
ε	Thickness parameter in Van de Vooren and de Jong transformation	
Γ	Circulation	$m^2 s^{-1}$
γ	A point in f-plane in Crowdy transformation used to control the radius and angle of attack of circular arc	
Γ_{max}	Spanwise maximum circulation around a wing	$m^2 s^{-1}$
μ	Mean	

μ_c	Center of circle	
ω	Vorticity	s^{-1}
ϕ_i	velocity potential of unitized velocity around the object moving in i direction	$m^2\,s^{-1}$
Ψ	Streamfunction	$m^2\,s^{-1}$
ρ	density	$kg\,m^{-3}$
σ	Root mean square error	
τ	Trailing edge angle	rad
τ_x	x direction wall shear stress	Pa
θ	Transition angle of circle in f plane from origin	rad

Non-dimensional Numbers

$Æ$	Corrected aspect ratio	
$Æ_{\text{actual}}$	Physical aspect ratio	
Γ^*	Non-dimensional circulation	
ω^*	Non-dimensional vorticity	
C_{τ_x}	Wall shear stress coefficient	
C_L	Lift coefficient	
C_P	Pressure coefficient	
M_∞	Mean flow mach number	
t^*	Non-dimensional time	
x^*	Non-dimensional distance	

Physics Constants

g	Gravitational acceleration on Earth	$9.8\,m\,s^{-2}$

Roman Variables

C_1	Camera 1	
C_2	Camera 2	
C_3	Camera 3	
P_1	Laser sheet position 1	
P_2	Laser sheet position 2	
P_3	Laser sheet position 3	
$\underline{\underline{AM}}$	Added mass matrix	kg
$\underline{F_{AM}}$	Added mass force	N

A	Constant used to rotate or rescale the domain in Crowdy transformation	
a	Radius of circle	m
a_∞	Residue of conformal map	
ac	Acceleration of wing	$\mathrm{m\,s^{-2}}$
b	Spanwise length for wing	m
$b_{\text{corrected}}$	Corrected spanwise length for wing	m
C	Chord length of airfoil	m
d_{wall}	Distance from wing to wall	m
f_{te}	Point in f plane corresponding to the airfoil trailing edge	
$F_{z_{\Gamma+AM}}$	Added downforce calculated by circulation and added mass force	N
F_{z_Γ}	Downforce calculated by circulation	N
$F_{z_{F/T}}$	Downforce measured by F/T transducer	N
$F_{mh_{\text{Brennen}}}$	Added mass force by Brennen	N
$F_{mh_{exp}}$	Residual force measured in experiments	N
g	Real axis of f plane	
H	Distance from the bottom of wing to the ground	m
h	Image axis of f plane	
h_{EP}	Height of endplates	m
i	Imaginary part	
L	Lift force	N
l	Discretized side length around the wing	
l	Chord length parameter in Van de Vooren and de Jong transformation	m
l_{wing}	Integration route around the wing	
n	Component of unit velocity at a certain point of the accelerating object	
P	Prime function	
P_∞	Static pressure in the free stream	Pa
P_s	Static pressure at a certain point	Pa
Q	Mean flow velocity as a function of time	$\mathrm{m\,s^{-1}}$
q	The radius of inner circle of the annular in f plane in Crowdy transformation	
q_j	local velocity at certain direction	$\mathrm{m\,s^{-1}}$
Q_∞	Mean flow velocity as a constant	$\mathrm{m\,s^{-1}}$

R	Distance from origin to the center of circle	
S	z direction shadow area of a wing	m^2
s	Constant used to shift the domain in Crowdy transformation	
t	Time	s
T_{gap}	Waiting time between experiments	min
W	Complex potential	$\mathrm{m}^2\,\mathrm{s}^{-1}$
W_U	Complex potential of uniform flow	$\mathrm{m}^2\,\mathrm{s}^{-1}$
W_Γ	Complex potential of circulation	$\mathrm{m}^2\,\mathrm{s}^{-1}$
X	Leading-edge suction force	N
x	Real axis of Y plane	
Z	Pressure difference force	N
z	Image axis of Y plane	

Contents

List of Figures

List of Tables

1 Introduction

1.1 Research Background

The starting position in formula 1 is relatively important comparing with other moment in the race [1]. Race before the first corner will have a significant position switch and will dominate in the following race [2]. In the field of aerodynamic, better understanding on the flow around an accelerating F1 car is still required (see subsection 1.2).

There are 6 main performance parameters for F1 cars. From modern lap-time simulation, if the performance parameters could be changed by a percentage, effects on lap times are shown in Table 1.1. The reference is a 2013 F1 car on an average of race track in the 2013 season [3].

TABLE 1.1: Effect of changing performance parameters on estimated lap time [3].

Performance Parameters	Changed Percentage	Effect on Lap Time
Grip – from tyres, suspension, etc.	10%	3.2%
Vehicle mass	10%	1.9%
Centre of gravity	10%	>0.4%
Engine and transmission of power	10%	1.5%
Electronics, hydraulics, pneumatics	KERS off	0.5%
Aerodynamics	10%	1%

Aerodynamics is not the most effective performance parameter for the general performance of an F1 car. F1 racing is governed and sanctioned by Fédération Internationale de l'Automobile (FIA), the International Automobile Federation (in English) [4]. Due to the FIA ruling, there is not much room to differentiate in the design of the engine, tyres, electronics or mass of F1 cars [5]. A further discussion on the importance of aerodynamics for F1 racing is shown in Appendix A.

In conclusion, aerodynamics is important for F1 cars in three ways.

- Technically, the aerodynamics is ranked the fourth important performance parameter, see Table 1.1.
- Realistically, due to the ruling in F1 racing, aerodynamics has the most room to differentiate in the design among racing teams, which means the aerodynamics part is far more important than "the fourth most important" in practice.
- Practically, high speed corners are common in F1 racing, where aerodynamics have a significant effect on high speed performance of F1 cars.

The goal of aerodynamic development is to create more downforce without a corresponding increase in drag [6].

1.2 Research Motivation

In the development of an F1 car, the correlation problem is a problem for every team. Correlation, in basic terms, is trying to match the data that you measure off the car against your simulator data (by Computational Fluid Dynamics (CFD) or wind tunnel). Where teams have problems is when their simulator data doesn't describe well what happens in reality (on the race track). Reducing the mismatch can improve the teams' development efficiency, and helps teams approach their development goal in the limited time [7].

F1 cars are usually tested in a wind tunnel, with moving ground and fixed car bodies. Dynamic motion (like accelerating, decelerating and cornering of the car) is hard to be resolved in this kind of wind tunnel [8]. Information about the flow around a car in dynamic motion can be only measured during pre-season testing (in 3 days). It's always too late to find the correlation problem between simulator data and on-track data [7]. A development environment which can measure the flow around an object in dynamic motion could solve the correlation problem.

There are 6 major components that have significant effect on the aerodynamics performance of an F1 car as shown in Table 1.2. This shows that the front wing has the second largest contribution to the total downforce of an F1 car.

TABLE 1.2: The downforce and drag from major components relative to aerodynamic of a 2009 Sauber Ferrari F1 car by percentage of impact on full car figure if removed [3].

Name of Components	Downforce	Drag
Front wing assembly	28%	20%
Front wheel, suspension and brake duct	-1%	10%
Chassis, bodywork, etc.	-8%	10%
Floor and diffuser	53%	13%
Rear wheel, suspension and brake duct	3%	18%
Rear wing assembly	25%	29%
Total	100%	100%

In general, there are three motivations for researching the front wing, as shown in the following list [3, 9].

- The front wing generates a significant amount of downforce.
- The front wing is important for the whole flow structure around an F1 car.
- The flow field around the front wing is relatively easy to research on, with a laminar homogeneous in-flow condition, which is easy to represent in an experiment.

There are three motivations for researching on accelerating flow, created by an accelerating object, as shown in the following list [10, 11, 12].

- F1 cars are always in dynamic motion like accelerating, decelerating and cornering when racing, see Figure A.1.
- Lack of experimental research on flow field around an F1 front wing in acceleration.
- Existing dynamic model (like the model of calculating added mass force) doesn't allocate existing experimental data very well.

The experimental set-up introduced in section 3 can measure the flow around an object in dynamic motion. With the knowledge from this research, measurement of more complex components in more complex flow conditions will be done and developed to the whole car's flow field measurement in acceleration, deceleration and turning.

The front wing of Tyrrell's 026 is used in this research. Previous research on continuous flow with ground effect has been done on this airfoil experimentally and simulationally [13, 10].

1.3 Research Objectives

The research objective is to have a better understanding of an accelerating wing with ground effect to improve the aerodynamics performance of an F1 car at the start of a race.

The lift coefficient of the wing will be investigated by potential flow theory, 2D-CFD simulation, and force measurement at different clearances to the ground, with a fixed angle of attack (AOA).

A 2D-CFD simulation and 2D-PIV measurement will be done to investigate the flow field around the wing. Both RANS and DES turbulence models will be applied in 2D-CFD simulation, to investigate the level of 3D flow structure [14]. An approach of building up the link between the flow field and predicted/measured downforce at the acceleration phase, transition phase and steady phase of the flow will be done. To record the flow development in the whole time series, 2 out of 3 cameras used in PIV measurement will be attached with a robot arm, and move together with the wing.

Based on the results obtained, recommendations for optimizing the wing's ground clearance will be provided. Additionally, suggestions for future research on dynamic flow and ground effect will be discussed.

2 Lift Coefficient with Ground Effect in Steady Flow

2.1 Conformal Mapping

2.1.1 Approach by Joukowski Wing

To generate exact solution of the Tyrrell front wing (by potential flow), mapping from the airfoil on the Y plane (physical plane $Y = x + iz$) to circle on the f plane (virtual plane $f = g + ih$) is the first step.

The Joukowski transformation is used to do conformal mapping as shown in Equation 2.1.

$$Y = f + \frac{C^2}{16f}, \tag{2.1}$$

where C is the chord of the airfoil at 0 angle of attack.

The Joukowski airfoil has a cusped trailing edge. For the Tyrrell 026's front wing, the trailing edge angle $\tau = 0.0845\,\text{rad} = 4.839°$. Possible flow conditions near the trailing edge with finite trailing edge angle in viscous flow are close to the flow conditions with a cusped trailing edge in inviscid flow. The trailing edge angle could be ignored in potential flow analysis for this wing [15].

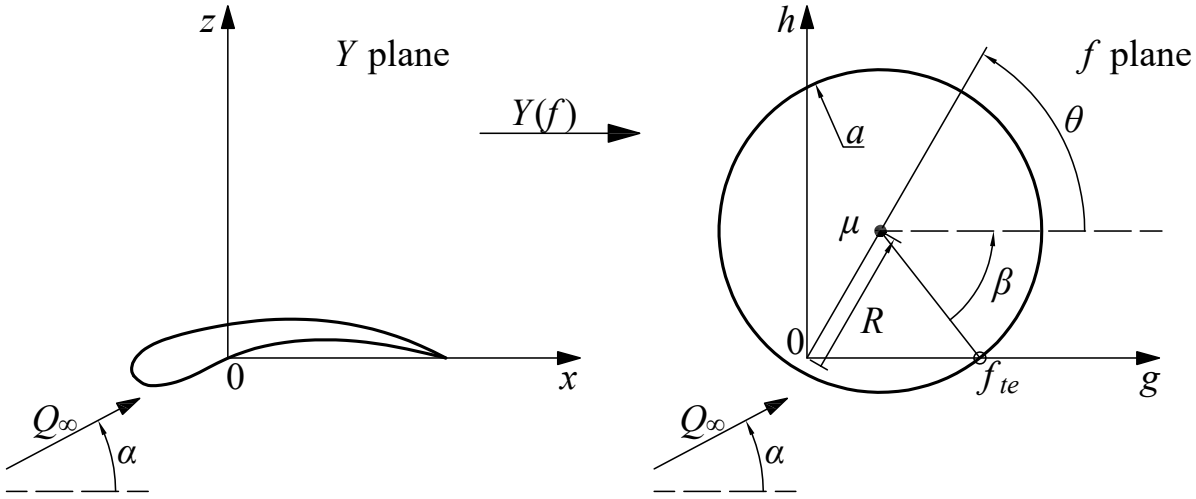

FIGURE 2.1: Joukowski transformation: mapping of an airfoil to a circle. The point $f_{te} = C/4$ corresponds to the trailing edge of the airfoil. The point μ is the centre of the circle in the f plane. The angle β is the angle between the vector pointing from μ to f_{te} and the x axle. Vector R points from the origin point to μ. Q_∞ represents the mean flow velocity. The angle α is the angle between the mean flow velocity and the chord line of the wing (in the figure aligned with x direction).

The Joukowski transformation has two free parameters: the radius of the circle in the f plane a, and the center of the circle μ [16]. This means not any specific type of airfoil can be mapped to a certain circle in the f plane as shown in Figure 2.1. For the experimental model of Tyrrell's front wing, the chord was set to be $C = 0.1108\,\text{m}$.

The result of conformal mapping by the Joukowski transformation is shown in Figure 2.2.

In this case, if the suction surface is better matched, the profile at the pressure surface is less accurate. With $a = 0.0277\,\text{m}$, $R = 0.00297\,\text{m}$ and $\theta = \pi/6$, the airfoil better matches the suction surface of the Tyrrell's front wing (which is considered more important based on previous research by pressure gradient is larger at suction side).

2.1.2 Lift Coefficient Calculation

For the 2D Joukowski wing, the circulation around the wing can be calculated by Equation 2.2 [16],

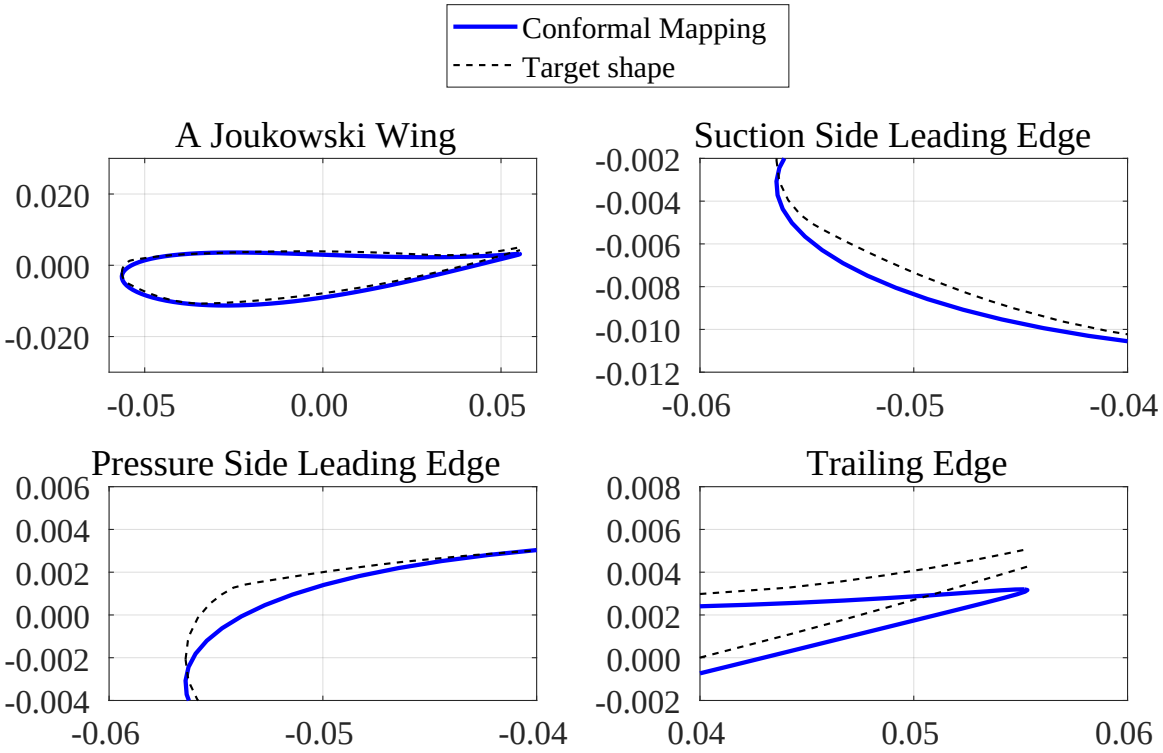

FIGURE 2.2: An airfoil created by Joukowski transformation to match the profile of Tyrrell 026's front wing with $a = 0.0277$ m, $R = 0.00297$ m and $\theta = \pi/6$rad. The length unit in this figure is m. The horizontal axis represents x axis in Y plane with the vertical axis represents z axis.

$$\Gamma = 4\pi a Q_\infty \sin(\alpha + \beta). \tag{2.2}$$

The 2D lift coefficient C_l is calculated by Equation 2.3 [16],

$$C_l = \frac{L}{\frac{1}{2}\rho Q_\infty^2 C}, \tag{2.3}$$

where L corresponds to the lift force of the wing, C corresponds to the chord length of the wing, Q_∞ corresponds to the mean flow velocity (velocity at infinity, as shown in Figure 2.1), ρ is the density of the mean flow.

The lift force in free stream L is given by Equation 2.4 [16]:

$$L = \rho Q_\infty \Gamma. \tag{2.4}$$

The lift force with ground effect $L_{\text{G.E.}}$ is given by Kundu [17] in Equation 2.5,

$$L_{\text{G.E.}} = \rho Q_\infty \Gamma - \frac{\rho \Gamma^2}{4\pi H}, \tag{2.5}$$

where H represents the ground clearance of the wing, the definition see Figure 3.1a.

The direction of lift force calculated by Equation 2.4 & Equation 2.5 is perpendicular to the flow direction, as shown in Figure 2.3.

For 3D rectangular wing with endplates, the aspect ratio Æ should be corrected by Equation 2.6 [18],

$$\text{Æ} = \text{Æ}_{\text{actual}} \left(1 + 1.9 \frac{h_{\text{EP}}}{b}\right), \tag{2.6}$$

where b represents the spanwise of the wing, h_{EP} is the height of endplates attached on the wing.

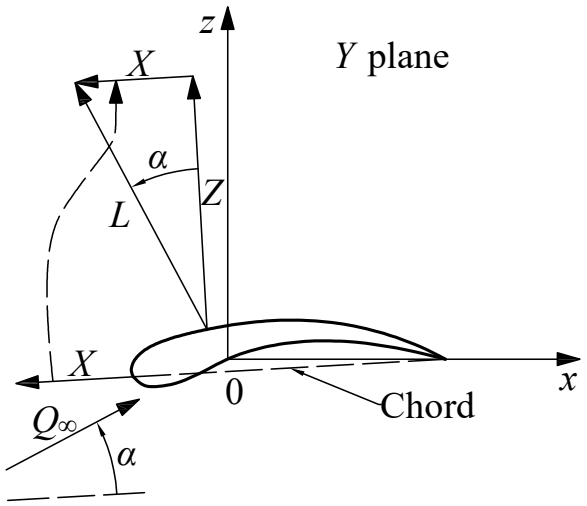

FIGURE 2.3: Definition of Lift force direction. X represents leading-edge suction force, in chord line direction pointing forward. Z represents pressure difference force, perpendicular to chord line. L represents lift force, perpendicular to flow direction. α represents the angle between Z and L, named angle of attack (AOA).

$Æ\mathrm{R}_{\mathrm{actual}}$ is defined by Equation 2.7,

$$Æ\mathrm{R}_{\mathrm{actual}} = b/C. \tag{2.7}$$

The 3D lift coefficient C_L is given by M. Hepperle in Equation 2.8 [19],

$$C_L = \frac{C_l}{\sqrt{1-M_\infty} + 2/Æ\mathrm{R}}, \tag{2.8}$$

where M_∞ corresponds to the free stream mach number, given by,

$$M_\infty = \frac{Q_\infty}{c_{\mathrm{water}}}, \tag{2.9}$$

where c_{water} corresponds to the speed of sound in water.

As shown in Figure 2.4, calculated by Equation 2.5 and Equation 2.8. To make the calculation result comparable with the experimental result by experimental set-up introduced in section 3, the value of c_{water}, Q_∞, b and h_{EP} is chosen to be $c_{\mathrm{water}} = 1500\,\mathrm{m\,s^{-1}}$, $Q_\infty = 0.5\,\mathrm{m\,s^{-1}}$ and $b = 0.55\,\mathrm{m}$ and $h_{\mathrm{EP}} = 0.05\,\mathrm{m}$. Compare with the lift coefficient in the free stream, at the angle of attack $\alpha = -6.60°$ the ground effect will be reduced to less than 10% when $H/C > 0.469$.

As shown in Figure 2.5, for this typical wing (inverse wing) lower angle of attack will have a stronger ground effect on downforce.

2.1.3 Flow Field

The complex potential for circulation and uniform flow around the Joukowski wing is calculated by Equation 2.10 and Equation 2.11 respectively [16],

$$W_\Gamma(f) = \frac{i\Gamma}{2\pi}\log(f/a), \tag{2.10}$$

$$W_U(f) = Q_\infty\left(f + \frac{a^2}{f}\right), \tag{2.11}$$

where f represents the coordinate of the points in the circle in the $f-$plane, a represents the

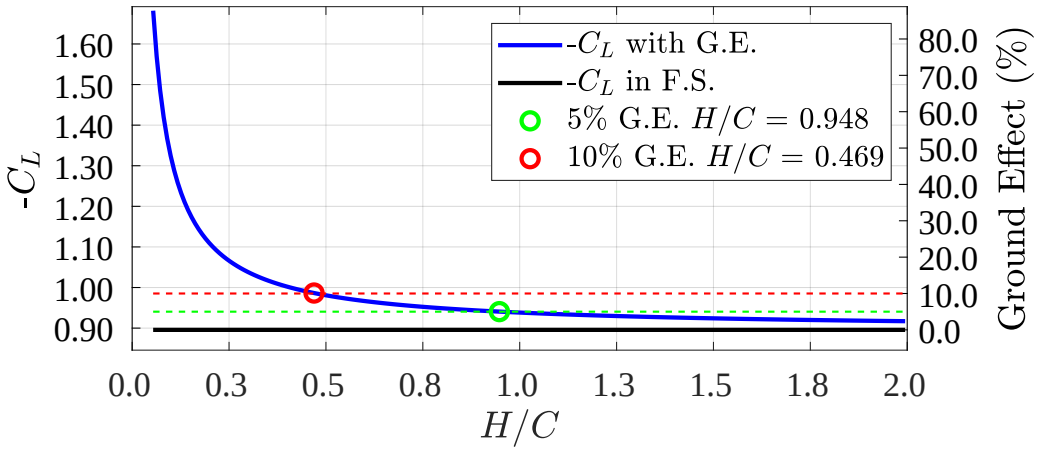

FIGURE 2.4: Inverse lift coefficient C_L with ground effect for a Joukowski wing based on Tyrrell 026's front wing at $\alpha = -6.60°$ plotted as a function of H/C. The strength of the ground effect is shown on the right y axis in percentage, compared with the lift coefficient at $\alpha = -6.60°$ in the free stream (shown in black).

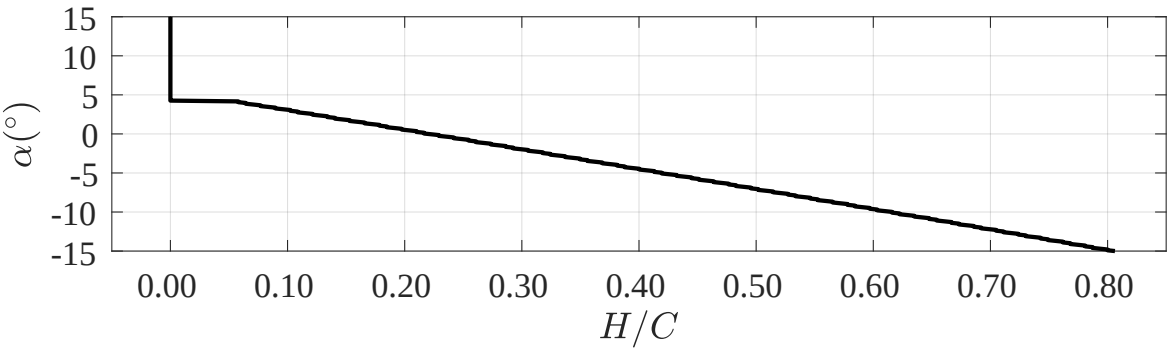

FIGURE 2.5: The angle of attack α and ground clearance & chord ratio H/C when the lift coefficient with the ground effect is 10% larger than the lift coefficient in the free stream for the Joukowski wing.

radius of the circle.

The total complex potential is calculated by adding up complex potential by uniform flow and circulation, given by (2.12),

$$W(f) = W_\Gamma(f) + W_U(f). \tag{2.12}$$

The streamlines around Tyrrell 026's front wing at $H/C = 0.054$, $\alpha = -6.60°$; $H/C = 0.469$, $\alpha = -3.45°$ and free stream ($H/C = \infty$, $\alpha = -3.45°$) are shown in Figure 2.6. The flow around the wing with ground effect can be analyzed using the panel method [20].

The streamlines around the wing have higher density in Figure 2.6a. Figure 2.6c shows the flow field around Tyrrell 026's front wing in free stream. Figure 2.6b and Figure 2.6c have similar flow field. The velocity below Tyrrell 026's wing is relatively high, corresponds to lower pressure in this region, and could introduce higher downforce.

2.1.4 Added Mass Matrix

For an object in an unsteady flow, there is a force $\underline{F_{AM}}$ necessary to accelerate the mass of fluid that is accelerating along with the object. According to Newton's second law, the added mass force $\underline{F_{AM}}$ in 6 directions (surge, sway, heave, roll, pitch and yaw) is given by Equation 2.13 [21],

$$\underline{F_{AM}} = -\underline{\underline{AM}} * \underline{ac}, \tag{2.13}$$

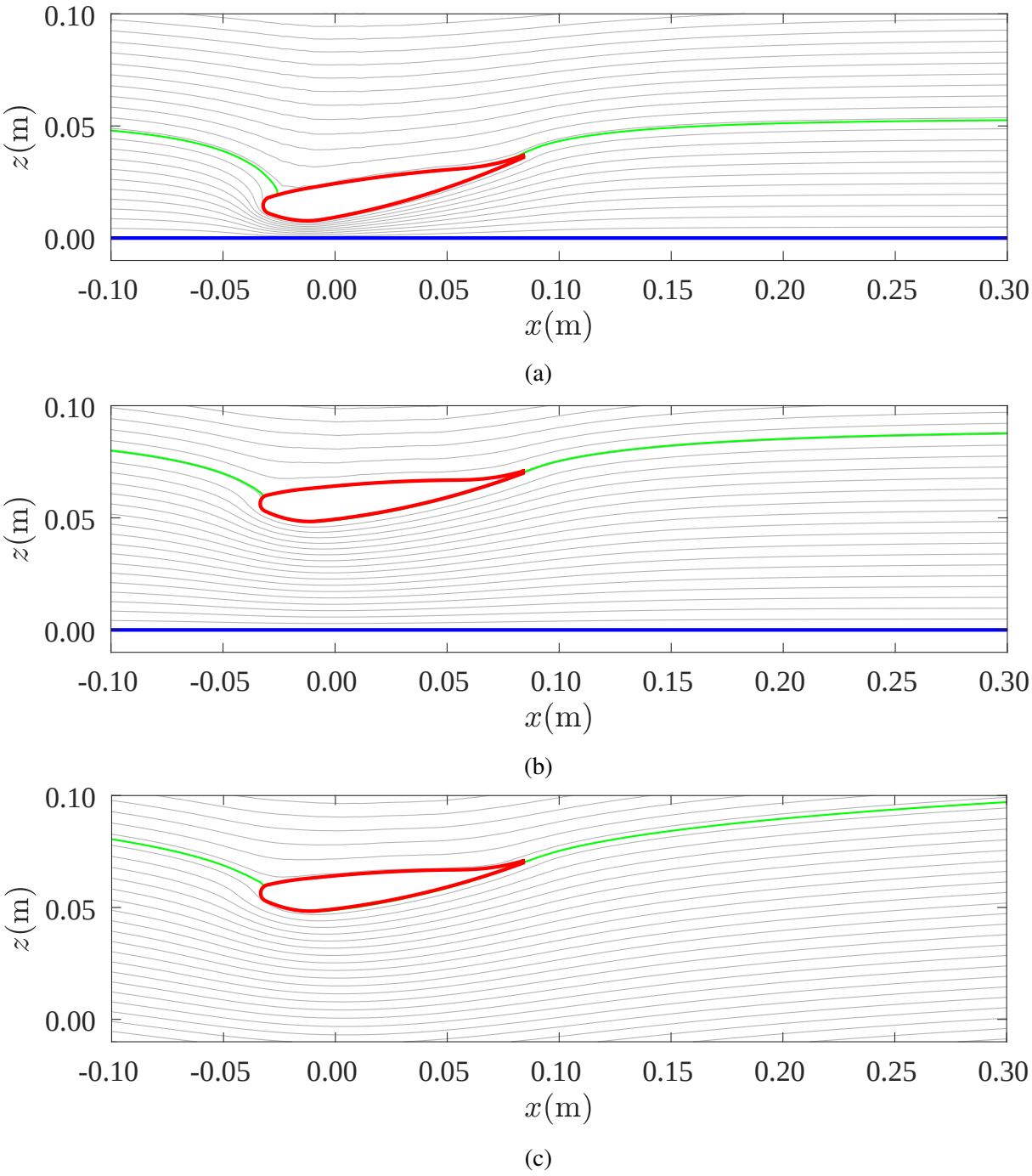

FIGURE 2.6: Visualization of the flow field of exact solutions for ground effect for Tyrrell 026's front wing at a) $\alpha = -6.60^\circ$ and $H/C = 0.054$, b) $\alpha = -3.45^\circ$ and $H/C = 0.469$, c) $\alpha = -3.45^\circ$ and the free stream. Streamlines are plotted in grey, the ground in blue, and the wing in red. In plot c), the coordinate is a reference coordinate, to be comparable with other plots. This figure is created by velocity field from *JavaFoil*. Internally, the ground effect works by creating a mirror image of the current airfoil below the ground, which is assumed to be at $z = 0$. This creates a system of multiple airfoils which is symmetrical about the $z = 0$ plane. The streamline corresponding to the wings is highlighted in green. The streamlines correspond to linearly spaced values of the streamfunction Ψ.

where $\underline{\underline{AM}}$ represents a 6×6 added mass matrix, $\underline{ac}$ represents acceleration at 6 directions, see Equation 2.14,

$$\underline{ac} = \begin{bmatrix} ac_{1_{\text{surge}}} & ac_{2_{\text{sway}}} & ac_{3_{\text{heave}}} & ac_{4_{\text{roll}}} & ac_{5_{\text{pitch}}} & ac_{6_{\text{yaw}}} \end{bmatrix}'. \tag{2.14}$$

For a single component in $\underline{F_{AM}}$ [21],

$$F_{AM_i} = -AM_{ij} * ac_j. \tag{2.15}$$

In the experiment (see section 3), the motion of the model is only in the surge (x_1 or x direction), and the interested force is in heave (x_3 or z direction). $\underline{\underline{AM}}$ is reduced to a 2×2 matrix, shown in Equation 2.16.

$$\underline{\underline{AM}} = \begin{bmatrix} AM_{11} & AM_{13} \\ AM_{31} & AM_{33} \end{bmatrix}. \tag{2.16}$$

Each component in the added mass matrix can be calculated by Equation 2.17 [21],

$$AM_{ij} = -\rho \oint_{l_{wing}} \phi_i n_j \mathrm{d}l, \tag{2.17}$$

where n_1 is the component of unit velocity at a certain point of the accelerating object, which is tangent to the local surface; n_2 is the component of unit velocity at a certain point of the accelerating object, which is normal to the local surface. ϕ_i is the velocity potential of unitized velocity around the object moving in i direction, defined by Equation 2.18 [21],

$$\phi_i = \int_{l_{wing}} \frac{q_j}{Q_\infty} \mathrm{d}x_j, \tag{2.18}$$

where q_j is local velocity in j direction on the surface of the object.
The non-dimensional added mass coefficient is defined by Equation 2.19 [21],

$$\underline{\underline{AM^{**}}} = \frac{\underline{\underline{AM}}}{\rho b C^2}. \tag{2.19}$$

As shown in section 3, the acceleration is in the x (x_1) direction. The measured downforce is in the z (x_3) direction. The term $\underline{\underline{AM}}$ relevant to F_{AM_3} is AM_{31}. Based on velocity distribution around the wing calculated by the panel method, with different clearance to the ground, calculated AM_{31} is shown in Figure 2.7.

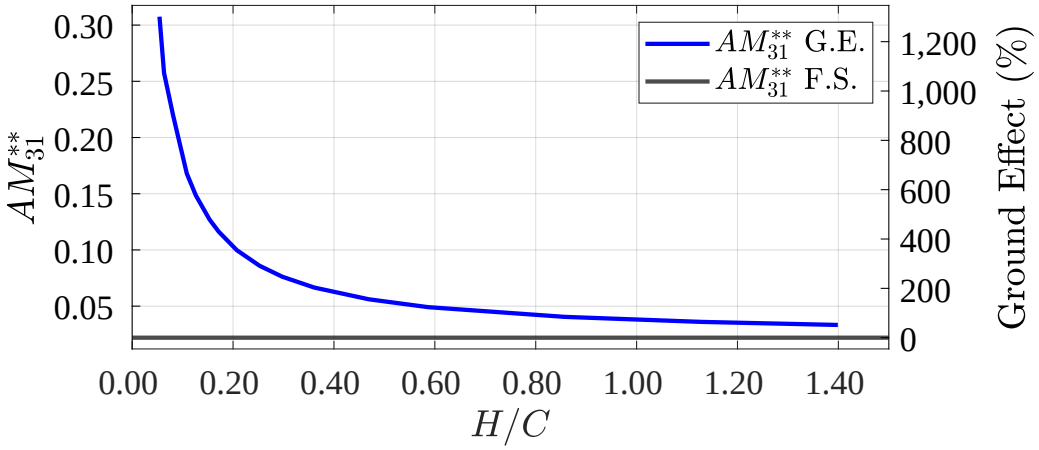

FIGURE 2.7: The added mass coefficient AM_{31}^{**} of an accelerating Tyrrell 026's front wing with ground effect at $\alpha = -6.60°$, plotted as a function of H/C. The strength of the ground effect is shown on the right y axis in percentage, compared with the lift coefficient at $\alpha = -6.60°$ in the free stream (shown in black).

As shown in Figure 2.7, the added mass has a similar "inverse function" behaviour like the lift coefficient with ground effect calculated by potential theory (as shown in Figure 2.5). At $\alpha =$

$-6.60°$, the ground effect acting on M_{31} is in $\mathcal{O}(10)$ higher than to $-C_L$.

At $H/C = 0.054$, the added mass force F_{AM_3} introduced by the wing with spanwise $b = 0.55\,\mathrm{m}$, in x direction acceleration $ac_1 = 1.64\,\mathrm{m^2\,s^{-1}}$ can be calculated to be,

$$F_{AM_3} = -AM_{31} * ac_1 * b = (-3.77 * 1.64 * 0.55)\,\mathrm{N} = -3.40\,\mathrm{N}. \tag{2.20}$$

2.2 A 2D CFD Simulation

2.2.1 Pre-processing

The CFD simulation is processed with structured mesh with 558100 to 997800 faces (depends on the ground clearance). Structured mesh is used for higher Computational efficiency [22]. A typical result at $H/C = 0.063$ is shown in Figure 2.8. In this research, the angle of attack is set to be $\alpha = -6.60°$.

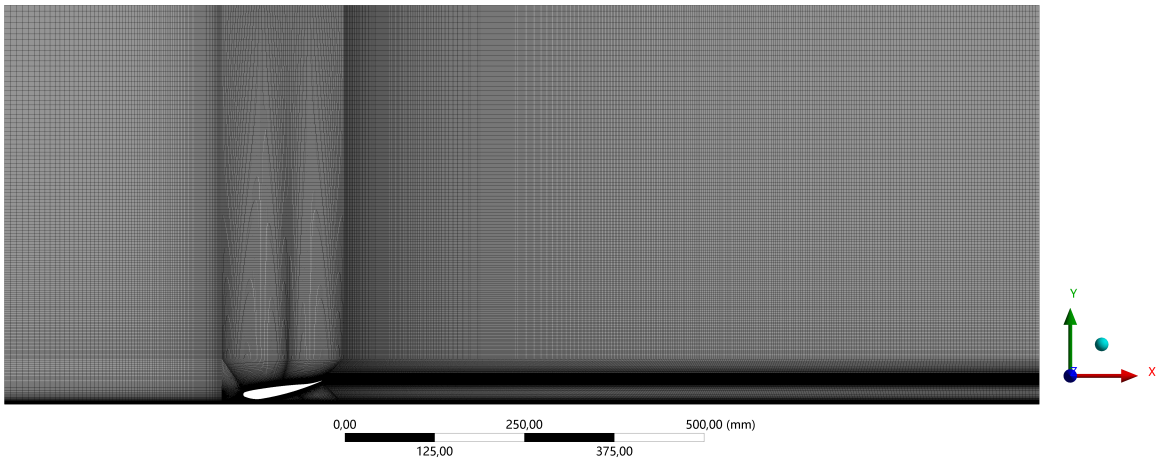

(a)

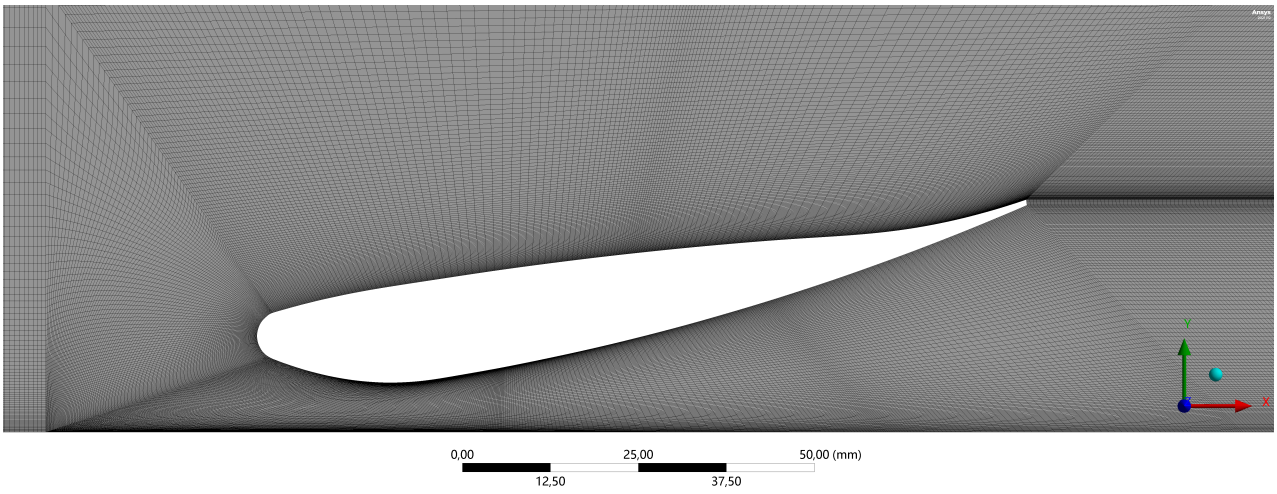

(b)

FIGURE 2.8: Structured mesh for the wing at $\alpha = -6.60°$, $H/C = 0.063$. (a) A general view. (b) A zoom-in view of mesh around the wing.

The CFD simulation is processed by the Menter's shear stress transport (SST) $k-\omega$ and detached eddy simulation (DES) turbulence models respectively. The variables used in the turbulence models are shown in Table D.1 and Table D.3 respectively. The numerical methods used in the cases with different turbulence models are shown in Table D.2 and Table D.4 respectively. The reference values used for C_L calculation is shown in Table D.5.

To simulate the experimental environment, the variables and the numerical methods used in the cases with different turbulence models are chosen by empirical conclusions [23]. To make the simulation result comparable with experimental results, the reference values in Table D.5 are set referring to the experimental set-up (see section 3).

2.2.2 Results of CFD simulation

As shown in Figure 2.9 and Figure 2.10, flow separation occurs in all cases with different clearance to the ground. Velocity field with vorticity distribution at the ground clearances of $H/C = [0.054, 0.153, 0.361, 1.128]$ are chosen to be shown. The flow separation can be found at the suction side of the wing, introducing the wake region at the suction side of the wing.

The simulation results by the SST $k-\omega$ model are shown in Figure 2.9. With the increment of ground clearance, the size of the wake region at the suction side of the wing is reduced. The flow is accelerated by the suction side of the wing and decelerated by the pressure side of the wing. At higher ground clearance, the acceleration and deceleration effect is more significant (see Figure 2.9a and Figure 2.9d), introducing the difference in the converged downforce (lift coefficient) as shown in Figure 2.13. Boundary layers can be found above the ground in cases at all ground clearances. At lower clearance, the interaction between the wing's wake region and the ground boundary layer can be found (see Figure 2.9a and Figure 2.9b). No clear influence on the ground boundary layer by the interaction can be found.

The simulation results by the DES model are shown in Figure 2.10. Huge vibration in downforce (lift coefficient) can be observed at low ground clearance, corresponding to the chaotic vortices distribution at $H/C = [0.054, 0.153, 0.361]$ (see Figure 2.10a, Figure 2.10b and Figure 2.10c). The flow behaviour without convergence generated by the 2D-DES model introduces a highly 3D flow structure that could be expected in experiments [14]. The highly 3D flow structure might be introduced by the boundary layer mix between the suction side boundary layer and the ground boundary layer, with non-well structured Kelvin–Helmholtz-like instability. The non-well-structured Kelvin–Helmholtz-like instability is introduced by the velocity shear between the two boundary layers [24]. At lower ground clearance, the strength of vorticity behind the wing is higher, corresponding to a more significant Kelvin–Helmholtz-like instability. At $H/C = 1.128$, 2 vortex streets generated by Kelvin–Helmholtz-like instability can be observed (see Figure 2.10d). The higher and weaker vortex street is generated by the velocity shear of the pressure side boundary layer and free stream; the lower and stronger vortex street is generated by the velocity shear of the suction side boundary layer and free stream [24].

The flow separation point can be found in Figure 2.11. In Figure 2.11, the non-dimensional length x^* calculated by Equation 2.21 is plotted as the x axle,

$$x^* = \frac{x}{C}, \tag{2.21}$$

where $x = 0$ is aligned with the leading edge of the wing.

Calculated by Equation 2.22, the wall shear stress coefficient $C_{\tau_x} < 0$ represents the flow separation by introducing a negative x direction wall shear stress. The wall shear stress coefficient C_{τ_x} is designed to be comparable with the pressure coefficient C_P (see Equation 2.23 [20]). The negative x direction wall shear stress at $x^* > 0.2$ is generated by the wake region vortex, which has a negative x direction velocity component at the suction side of the wing (see Figure 2.9).

$$C_{\tau_x} = \frac{\tau_x - P_\infty}{\frac{1}{2}\rho Q_\infty^2}, \tag{2.22}$$

where τ_x represents the x direction wall shear stress, P_∞ represents the static pressure in the free stream. The value of static pressure in the free stream is set to be $P_\infty = 0\,\text{Pa}$.

At the suction side, at $x^* < 0.2$, the higher ground clearance introduces lower x direction wall

shear stress τ_x (see Figure 2.11a). At $x^* > 0.2$, for $H/C > 0.153$ the higher ground clearance introduces lower negative τ_x, corresponding to weaker wake region vorticity (see Figure 2.11b and Figure 2.9). A trend of re-attachment of the flow can be found around $x^* = 0.4$. For $H/C \geq 0.361$, the flow is re-attached after the initial separation around $x^* = 0.4$. (see Figure 2.11b). At $0.2 < x^* < 0.4$, $H/C < 0.153$, the higher ground clearance introduces higher negative τ_x. At $x^* > 0.4$, $H/C < 0.153$, no clear difference on τ_x can be observed among cases with different ground clearances. At the pressure side, no clear difference on τ_x can be observed among cases.

The position of the stagnation point on the wing can be found in Figure 2.12.

Calculated by Equation 2.23 [20], the pressure coefficient $C_P = 1$ represents the velocity at the outer boundary of the boundary layer around the wing equal to 0.

$$C_P = \frac{P_s - P_\infty}{\frac{1}{2}\rho Q_\infty^2}, \tag{2.23}$$

where P_s represents the static pressure at a certain point. The point with $C_P = 1$ is defined to be the stagnation point. The point with $C_P > 1$ corresponds to the velocity at that point is negative. The point with $0 < C_P < 1$ corresponds to the velocity at that point lower than the mean flow velocity Q_∞. The point with $C_P < 0$ corresponds to the velocity at that point higher than the mean flow velocity Q_∞.

As shown in Figure 2.12b, from low to higher ground clearance, the stagnation point moves away from the leading edge of the wing. As shown in Figure 2.9, the stagnation point is moving from the leading edge to the pressure side. The simulation result on the stagnation point opposites the flow field calculated by potential flow (see Figure 2.6), corresponding to the opposite calculation result of the circulation around the wing. The conflict results on circulation lead to the opposite distribution of simulated (calculated) downforce at different ground clearances as shown in Figure 2.13. The observed opposition is introduced by the difference in flow theory. No turbulence model is used in the potential flow [20]. A mismatch between potential flow results and CFD simulation results can be expected.

The integration of pressure distribution around the wing introduces the downforce $-L$ applying on the wing, as shown in Equation 2.24,

$$L = \oint_{\text{wing}} P_s \mathrm{d}x, \tag{2.24}$$

where the integration route is direction irrelevant. To be comparable with the results by potential flow, the calculation result is shown in lift coefficient C_L (see Figure 2.13).

As shown in Figure 2.12a, the upper lines represent the pressure coefficient distribution at the pressure side of the wing; the bottom lines represent the pressure coefficient distribution at the suction side of the wing. At higher ground clearance, the deceleration effect of the flow at the pressure side is more significant. From $H/C = 0.054$ to $H/C = 0.469$, at $x^* < 0.2$, at higher ground clearance, the acceleration effect of the flow at the suction side is more significant, due to the reduction in the suction side wall shear stress (see Figure 2.11a). At the ground clearance from $H/C = 0.054$ to $H/C = 0.298$, the reduction of acceleration effect is lower than in cases with higher ground clearance. This behaviour in pressure distribution corresponds to the downforce variants with ground clearance as shown in Figure 2.13. The mismatch between two different predictions at $H/C > 0.298$ is due to the difference in flow separation condition at the suction side of the wing. The mismatch at $H/C < 0.298$ is due to the boundary layer mix between the suction side and the ground, which reduced the flow acceleration effect.

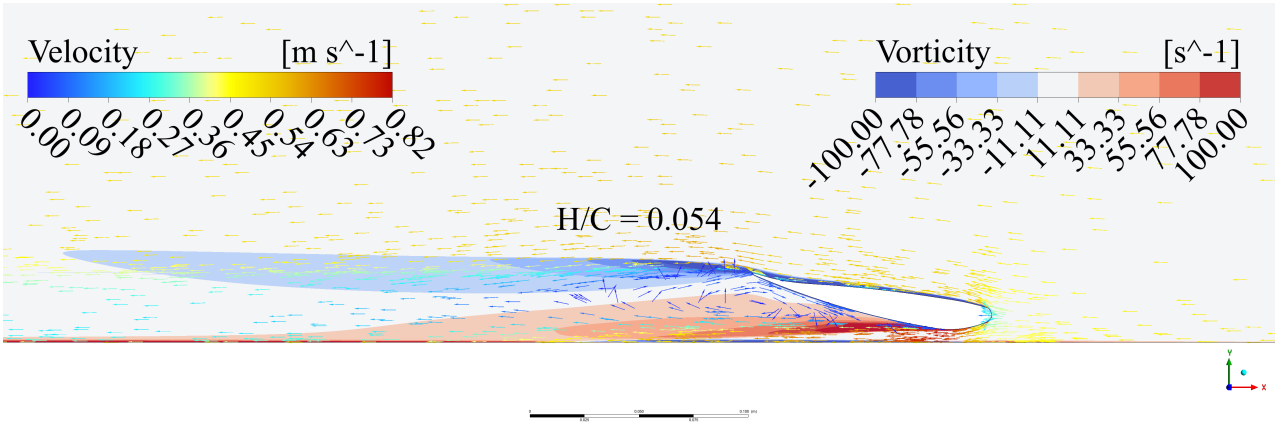

(a)

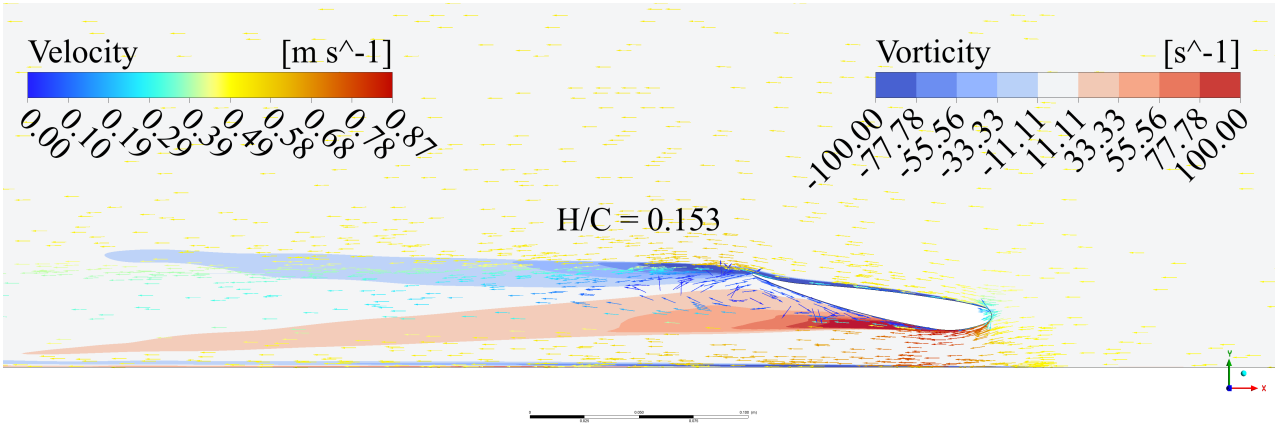

(b)

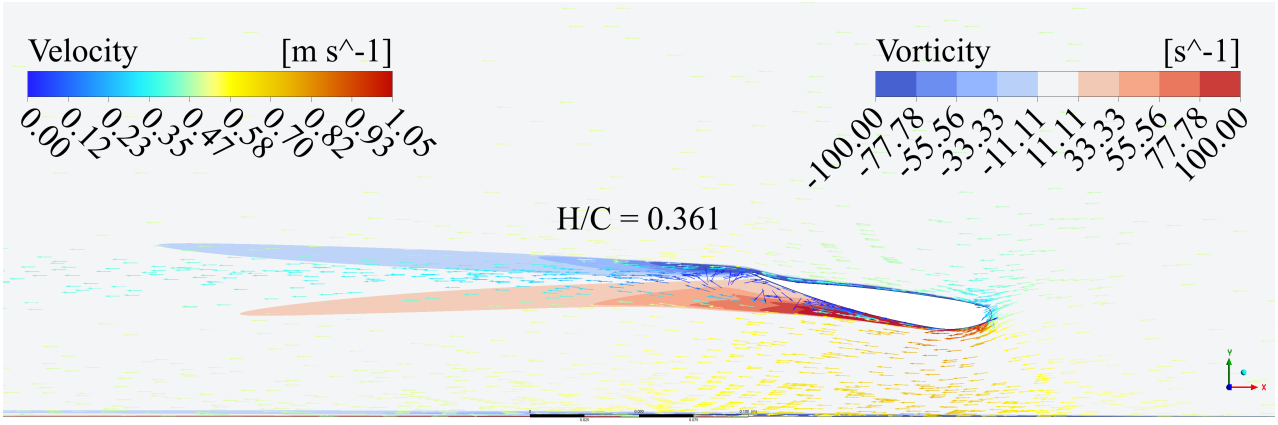

(c)

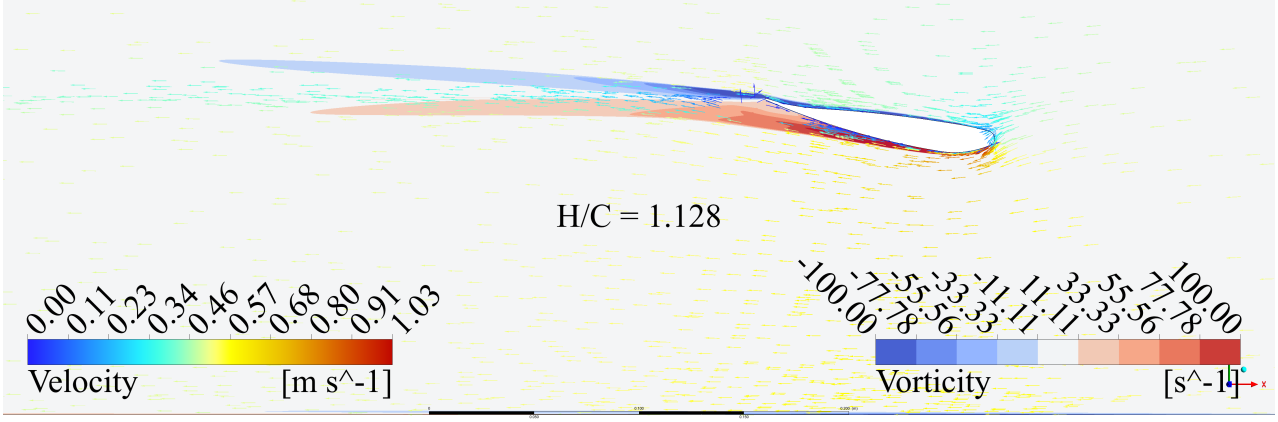

(d)

FIGURE 2.9: Vorticity and velocity around the wing at $\alpha = -6.60°$ (by SST $k-\omega$).

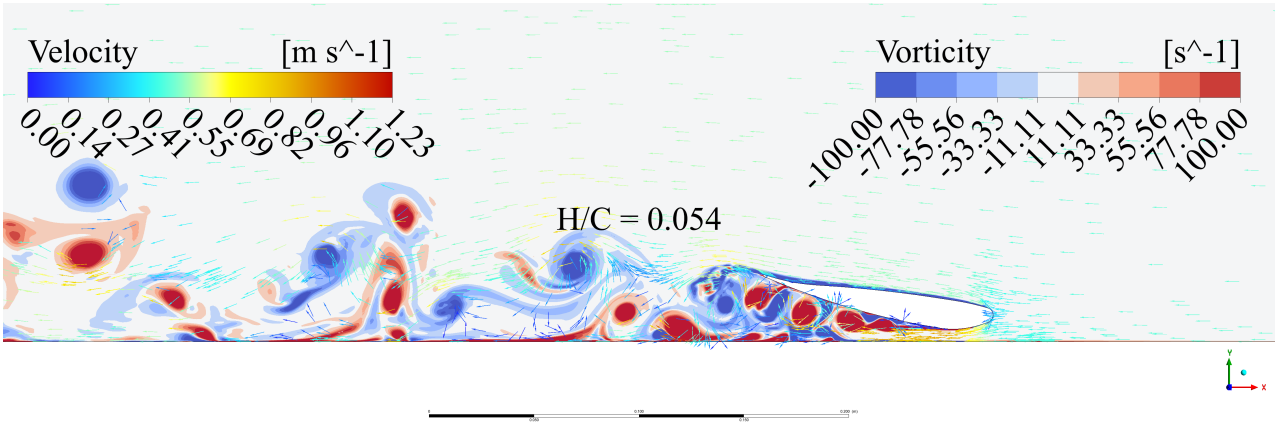

(a)

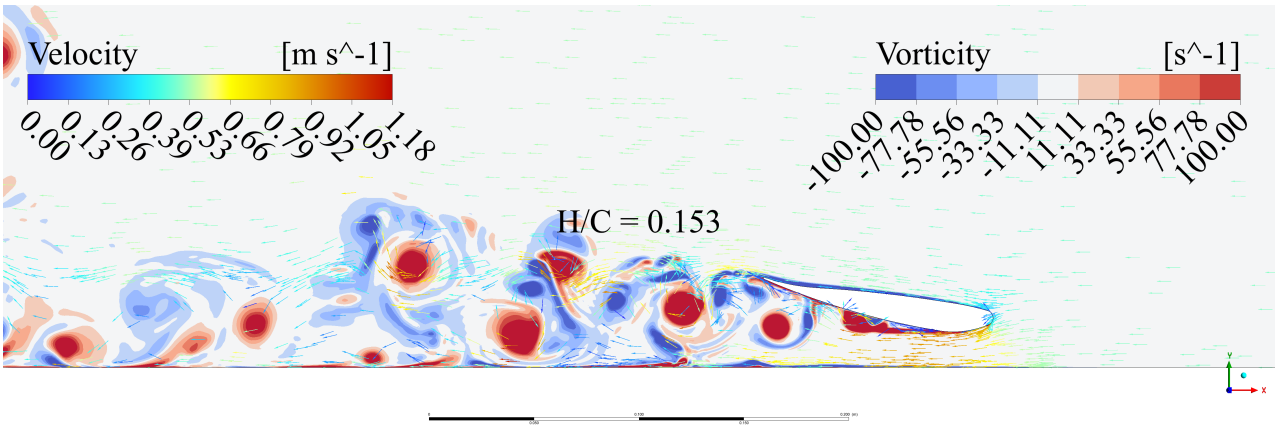

(b)

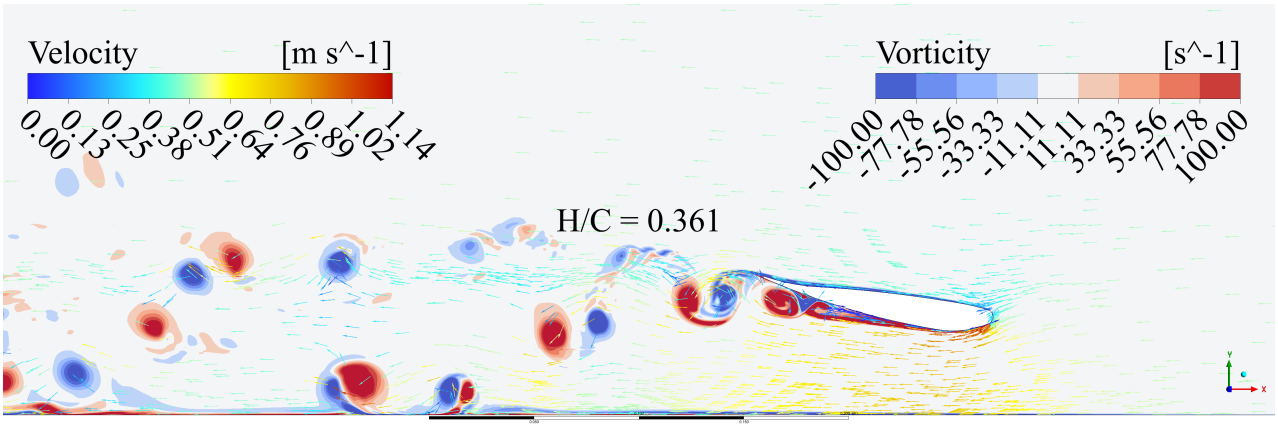

(c)

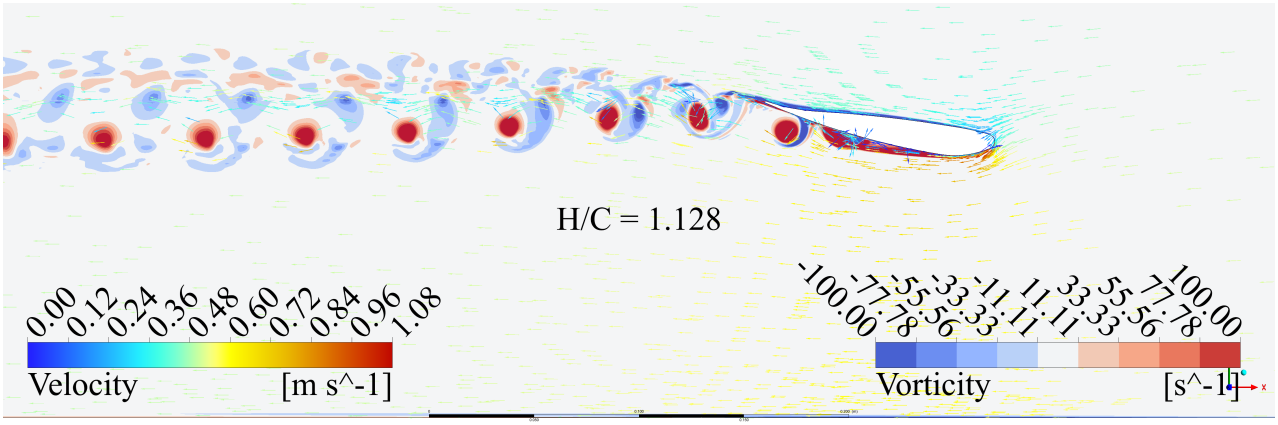

(d)

FIGURE 2.10: Vorticity and velocity around the wing at $\alpha = -6.60°$ (by DES).

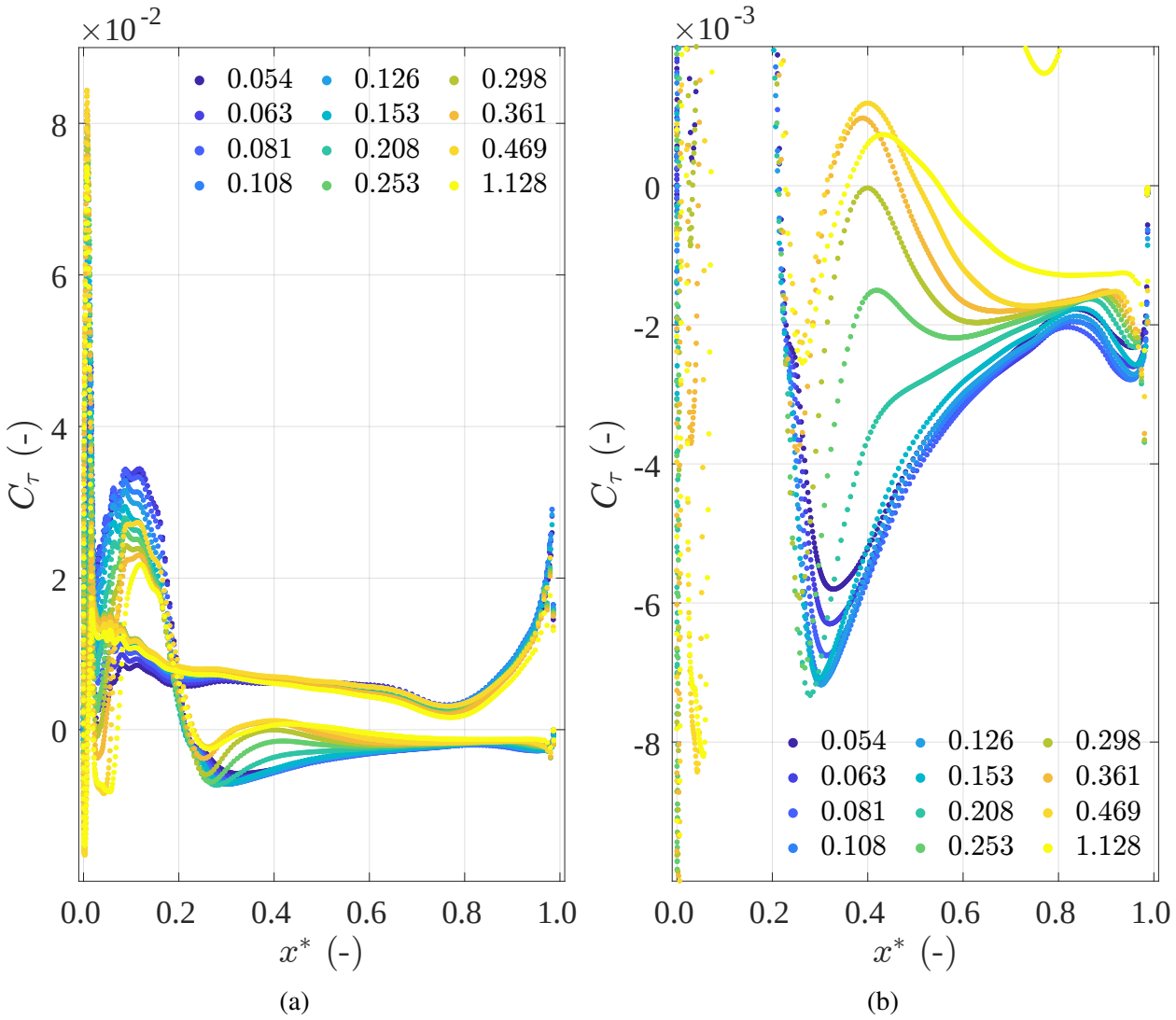

FIGURE 2.11: x direction wall shear stress distribution around the wing at different ground clearances, simulated by SST $k-\omega$ and plotted in non-dimensional form. The clearance is shown in legend from $H/C = 0.054$ to $H/C = 1.128$. $x^* = 0$ and $x^* = 1$ align with the leading edge and trailing edge of the wing respectively. (a) A general view. (b) A zoom-in view on the area with $C_{\tau_x} < 0$, representing the area with flow separation.

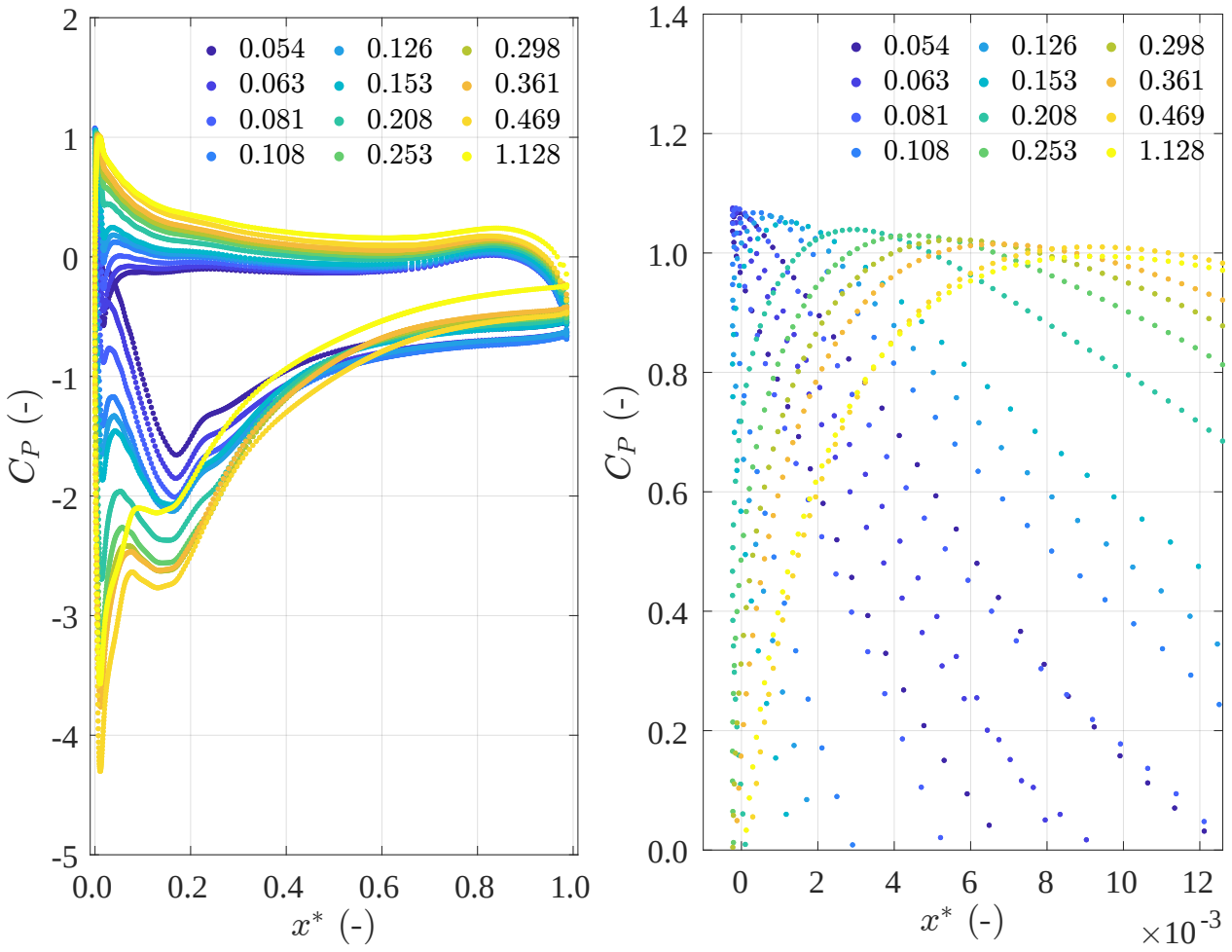

FIGURE 2.12: Pressure distribution around the wing at different ground clearances, simulated by SST $k-\omega$ and plotted in non-dimensional form. The clearance is shown in legend from $H/C = 0.054$ to $H/C = 1.128$. $x^* = 0$ and $x^* = 1$ align with the leading edge and trailing edge of the wing respectively. (a) A general view. (b) A zoom-in view at the leading edge.

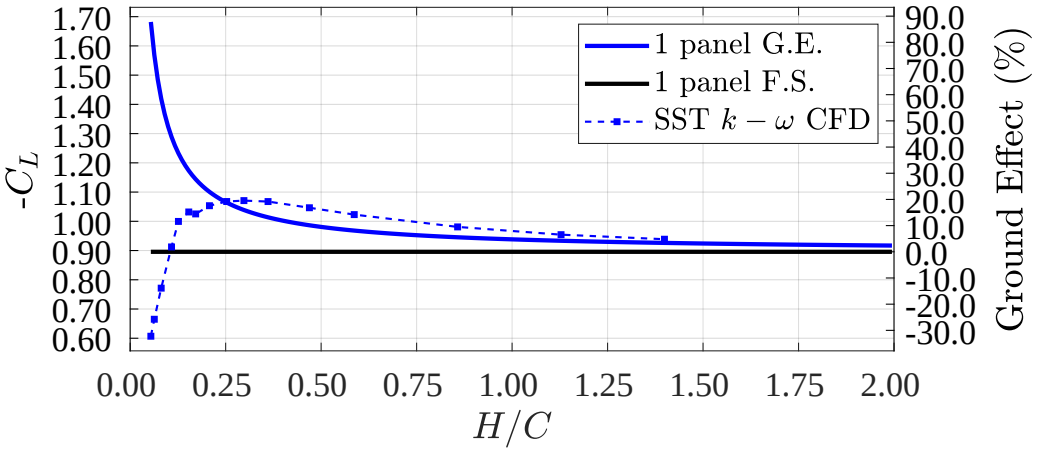

FIGURE 2.13: A comparison between C_L prediction result by SST $k-\omega$ CFD and potential theory, plotted by non-dimensional ground clearance H/C. The prediction by potential theory (in blue and black) is corrected by the Wagner function at $t^* = 10$ [25]. Similar inverse function behaviour can be found in experimental results at $H/C > 0.298$. For cases at $H/C < 0.298$, the lift coefficient is a positive correlation with clearance, which is against the potential theory prediction.

3 Experimental Set-up

3.1 Introduction

Figure 3.1 shows the experimental set-up used in this study. All experiments are done in an open-top glass tank with a horizontal cross-section of 2 m × 2 m and a height of 0.6 m with water depth of 0.5 m (to avoid spilling over the edge of the tank). The dimensions of the tank are chosen to be as large as practically possible to avoid blockage effects and wall effects. The wing used in this study has a Spanwise width $b = 550$ mm and a chord length $C = 110.8$ mm. The dimension of the wing is chosen to match the Reynolds' number of a F1's front wing in racing. The wing is aligned such that its major dimensions b and C are parallel to the y and x direction, respectively, see Figure 3.1b. The wing is mounted to an industrial robot arm (Reis Robotics RL50) with a cylinder strut. A force/torque transducer (AMTI 6-DOF F/T transducer) with recording rate 10 kHz is installed between the robot arm and the strut to measure the hydrodynamic forces acting on the plate. The hydrodynamic forces on the cylinder strut are considered to be negligible compared to those on the wing.

3.2 Kinematics

The robot moves the wing along a straight line in the x-direction, from x_1 to x_2, over a distance of 1.15 m (Figure 3.1), starting and stopping at a distance of three times chord length from the walls, such that the walls do not affect the flow around the wing. The velocity fields obtained from the PIV measurements show that the flow is unperturbed, i.e. a flow velocity magnitude ¡1% of the wing velocity Q, at $3C$ ahead of the wing. To investigate the ground effect on the lift, the clearance H, defined as the distance between the bottom edge of the wing and false bottom, as shown in Figure 3.1a, is varied from 0 to 155 mm.

The robot itself provides the data on the position $x(t)$ and the velocity $Q(t)$ at a default rate of 92 Hz. The robot position data are within 0.1 mm repeatable, with a resolution of 1μm [12]. Figure 3.2 shows a typical recorded data.

The wing is linearly accelerated to a velocity $Q_\infty = 0.5\,\mathrm{m\,s^{-1}}$; see Figure 3.2. The acceleration of the robot is set to $ac = 1.64\,\mathrm{m\,s^{-2}}$. Due to the non-linear behaviour of the robot's acceleration, the prescribed velocity is reached in 0.45 s. At $Q_\infty = 0.5\,\mathrm{m\,s^{-1}}$ the Reynolds number (using the chord C as a characteristic length) is $Re = 55 \times 10^3$, which is well into the turbulent regime. Higher velocities would complicate the experiments by increasing the settling time of the turbid water in the tank between experiments. As shown in Figure 3.3, the acceleration phase is until $t^* = 1$. t^* is non-dimensional number defined by Equation 3.1.

$$t^* = \frac{1}{C}\int_0^t Q(t)\mathrm{d}t \tag{3.1}$$

3.3 Particle image velocimetry

To quantify the flow field, planar particle image velocimetry (PIV) with 2 side-by-side cameras and 1 fixed camera was used.

The field of view is in the vertical $x-z$ plane through 3 different spanwise position on the wing (P_1, P_2, P_3). A 4-megapixel high-speed camera (LaVision Imager Pro HS, C_3 in Figure 3.1) was used to capture the flow through the glass wall in the positive y-direction at a frame rate of 1278 f.p.s. To capture the entire run of the wing over 1.15m, 2 cameras (Phantom VEO 640L with a 55 mm Nikon lens) were attached to the robot, looking at the wing's leading edge and trailing edge respectively with the field of view (FOV) approximately 180 mm × 112.5 mm. A typical result of a de-wrapped raw image will be shown in subsubsection 4.1.2.

Neutrally buoyant fluorescent spherical tracer particles (Cospheric UVPMS-BR-0.995, 53 – 63μm diameter) were added to the flow (30 g) and were illuminated using a 532 nm Nd-YAG 150 W

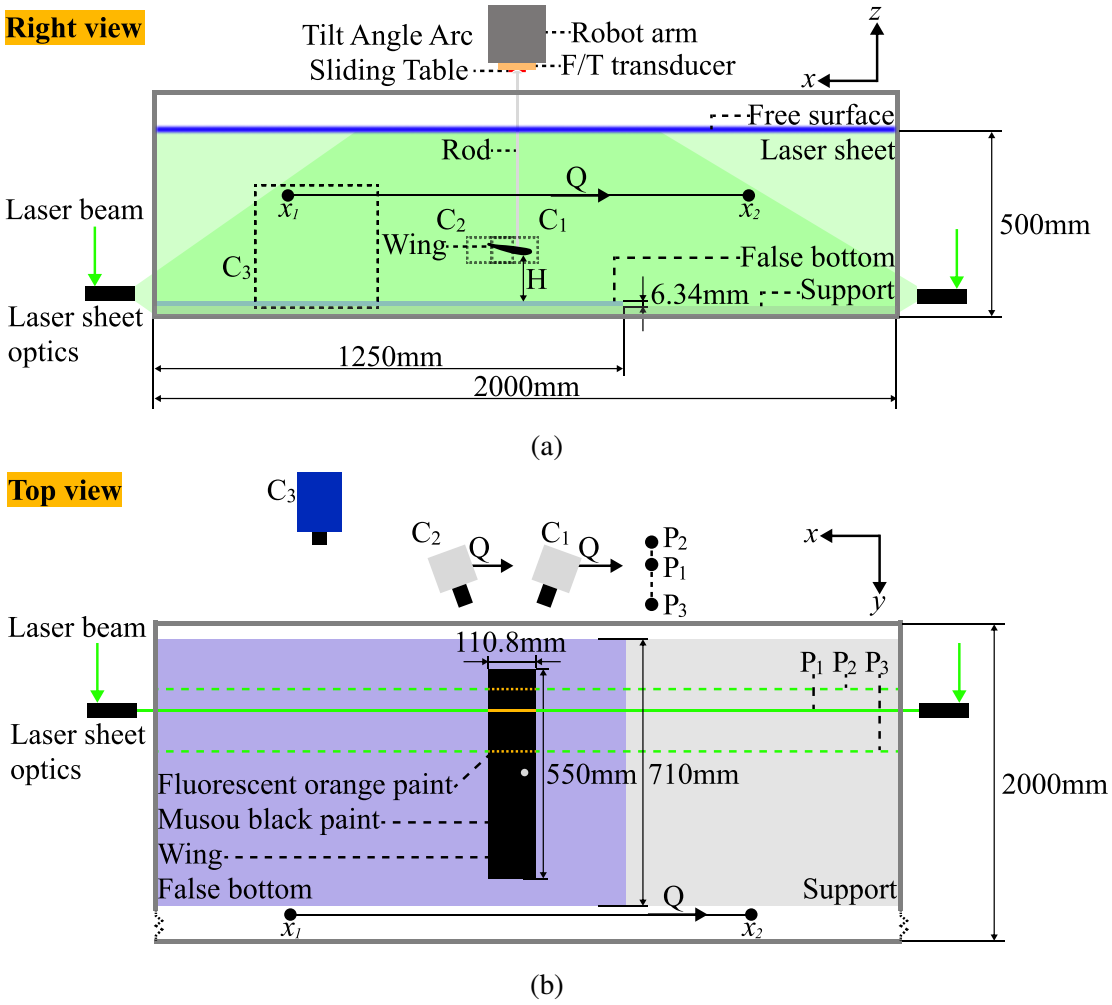

FIGURE 3.1: Schematic of the experimental set-up. The false bottom was introduced to ensure a plane parallel to the robot arm's x and y direction. (Constant clearance H) (a) Right view of the set-up with the robot arm holding the wing moving from x_1 to x_2 at velocity Q at a distance from the ground H. The vertical laser sheet used for particle image velocimetry (PIV) was shown in transparent green. The field of view (FOV) of the 3 cameras was shown in black dashed rectangle, labelled C_1, C_2 and C_3 (b) Top view showing the 3 positions of laser sheet (P_1: 110 mm to the spanwise edge, P_2: 50 mm to the spanwise edge, P_3: 175 mm to the spanwise edge). The position of the laser sheet was shifted by moving the robot arm's $y-$axis. Both cameras were positioned at the left of the tank. Camera C_1 and C_2 were attached to robot arm. To maintain the same magnification, their distance to the laser sheet was maintained constant. Camera C_3 has a fixed position.

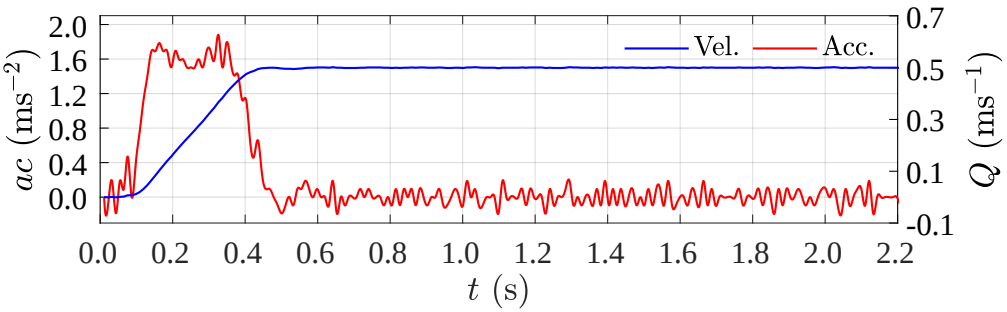

FIGURE 3.2: A typical robot-recorded result of Wing velocity Q and wing acceleration ac as a function of time t at $H/C = 0.153$.

laser (Litron LDY304-PIV). The acquired images were analysed using commercial software (LaVi-

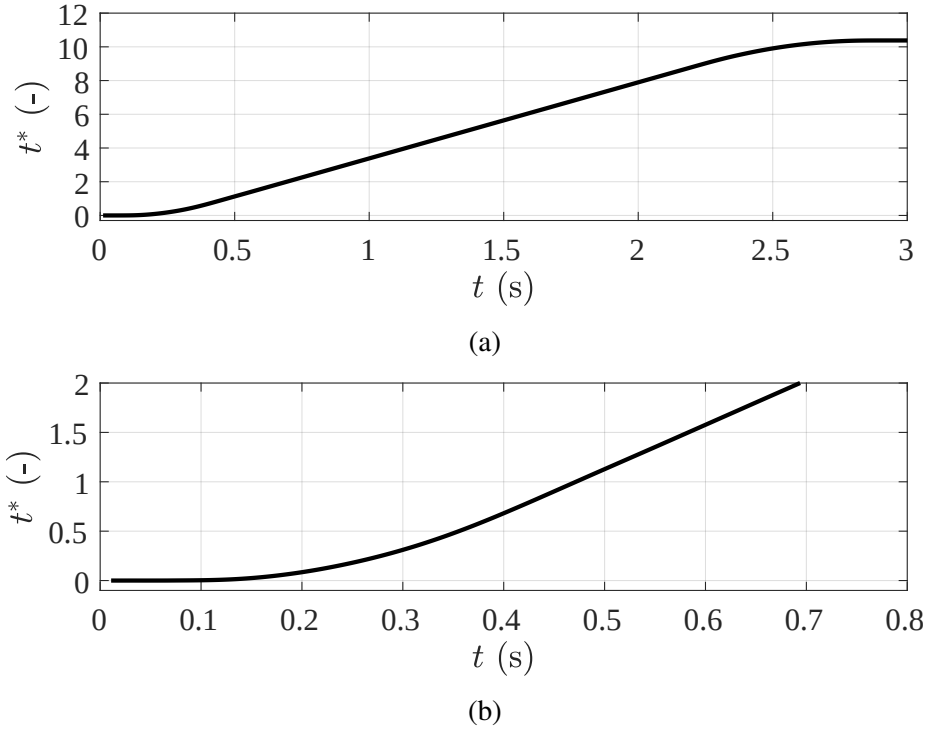

FIGURE 3.3: A typical robot displacement integrated by the robot-recorded result of Wing velocity Q. The displacement was non-dimensionalized and plotted as a function of time t at $H/C = 0.153$. (a) A general view from steady to the end of the movement route. (b) A zoomed-in view at the acceleration phase.

sion DaVis 8.4 and LaVision DaVis 10.2). A multi-pass correlation-based PIV algorithm was used to obtain the flow velocity field from the image pairs. The interrogation windows of the double subsequent passes were 48×48 pixels for the first pass and 24×24 pixels for the second pass. A 50% overlap between adjacent interrogation positions was used. This resulted in velocity vector fields with a vector spacing of 0.65 mm and a cumulative first and second vector choice of $> 98\%$ in the area of interest, i.e. in the wake of the wing. To stitch the recorded results, self-calibration was applied to images at the same frame from C_1 and C_2.

The results of position P_1 is shown in subsection 4.3; the results of position P_2 and P_3 is shown in Appendix F.

3.4 The model (wing)

As shown in Figure 3.1b, to reduce the influence of reflected light, the wing is painted in MOSOU black, which can absorb up to 99.4% of visible-light [26]. To see the edge on the wing lighted by laser sheet, fluorescent orange paint was applied on P_1, P_2, P_3 on the wing, which will absorb the light from laser (green), and release orange light.

To simulate a dirty/scratched wing in a race, the boundary layer is tripped by applying a z-shape sticker (with 0.5 mm in thickness) at the suction side close to the leading edge.

4 Downforce and PIV Measurement

4.1 Typical result

4.1.1 F/T transducer

All calculations and analyses are performed using unfiltered signals. However, for better readability the signal is filtered using a second-order Savitzky–Golay filter [27] with a filter width of 1001 samples, i.e. 0.1 s. For each measurement, the filter was applied twice to reduce the high-frequency oscillations. The oscillation might be caused by the vortex street at the trailing edge, introduced by Kelvin–Helmholtz-like instability, which will be discussed in subsection 4.3.

The grey line in Figure 4.1 plots F_z as a function of time formation time t^* for an experiment with a velocity $Q_\infty = 0.50\,\mathrm{m\,s^{-1}}$ accelerated from $Q = 0\,\mathrm{m\,s^{-1}}$, with an acceleration of $ac = 1.64\,\mathrm{m\,s^{-2}}$, at $H/C = 0.0542$, $\alpha = -6.60°$. This figure is plotted by $-F_z$ instead of $-C_L$ to improve the readability of the reduction of downforce after the wing reached steady velocity ($t^* = 1$). The force signal exhibits a clear peak at $t^* = 0.9$.

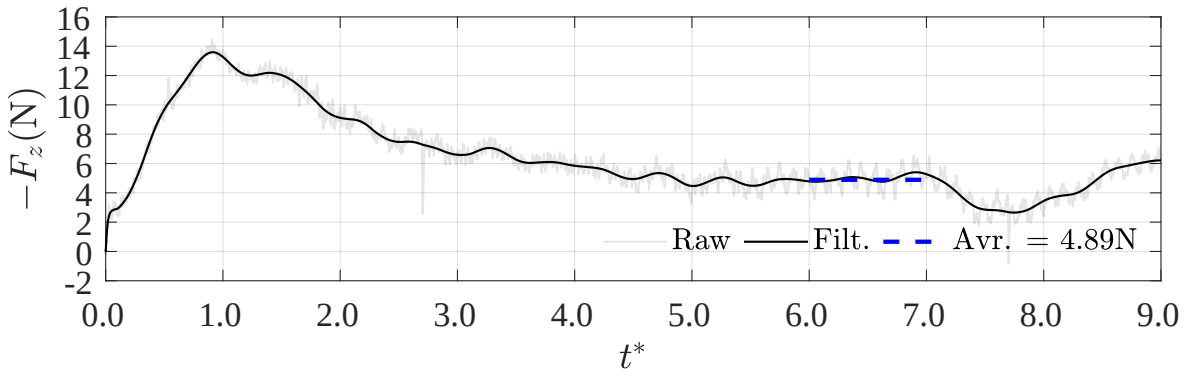

FIGURE 4.1: A typical unfiltered force signal F_z sampled at 10 kHz (grey) and the filtered force signal (black) at $Q_\infty = 0.50\,\mathrm{m\,s^{-1}}$, $H/C = 0.0542$, $\alpha = -6.60°$. The expectation of downforce from $t^* = 6$ to $t^* = 7$ is calculated as the downforce for the steady phase, to compare with the result by exact solution. In this period, the circulation could be considered to be constant and $\Gamma_{\mathrm{Exp.}} = 91\%\Gamma_\infty$ according to Wagner function [25]. The drop in downforce after $t^* = 7.4$ is due to the end of the false bottom.

4.1.2 High-speed cameras

The raw image from C_1 and C_2, de-wrapped by the calibration matrix is shown in Figure 4.2a and Figure 4.2b respectively. It can be found that the view at the wing's suction side at P_1 (the main position) is well resolved.

As shown in Figure 4.3, there is a mismatch in the airfoil's pressure side between cameras, due to the perspective difference shown in Figure 4.2.

The circulation Γ is calculated by Equation 4.1 [17],

$$\Gamma = \oint_C \mathbf{Q} \cdot \mathrm{d}\mathbf{l}, \tag{4.1}$$

where $\mathbf{Q}$ represents the velocity field, $\mathbf{l}$ represents a clockwise route on the control volume around the wing shown in Figure 4.3.

The vorticity ω is calculated by Equation 4.2 [17],

$$\omega = \nabla \times \mathbf{Q}. \tag{4.2}$$

The circulation is non-dimensionalized by Equation 4.3 [28],

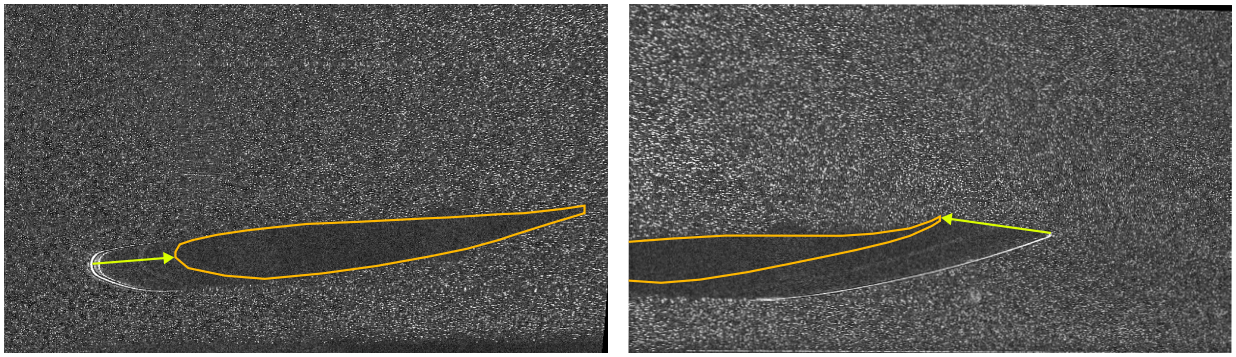

(a) (b)

FIGURE 4.2: A set of de-wrapped raw images taken by (a) camera 1, (b) camera 2, at P_1, $H/C = 0.153$, $t^* = 2$. To show the difference in perspective, (a) the leading edge and (b) the trailing edge of the wing, are shown by yellow arrows. The arrows go from the laser sheet to the spanwise edge (shown in orange).

$$\Gamma^* = \frac{\Gamma}{CQ_\infty}. \tag{4.3}$$

The vorticity is non-dimensionalized by Equation 4.4 [12],

$$\omega^* = \frac{\omega C}{Q_\infty}. \tag{4.4}$$

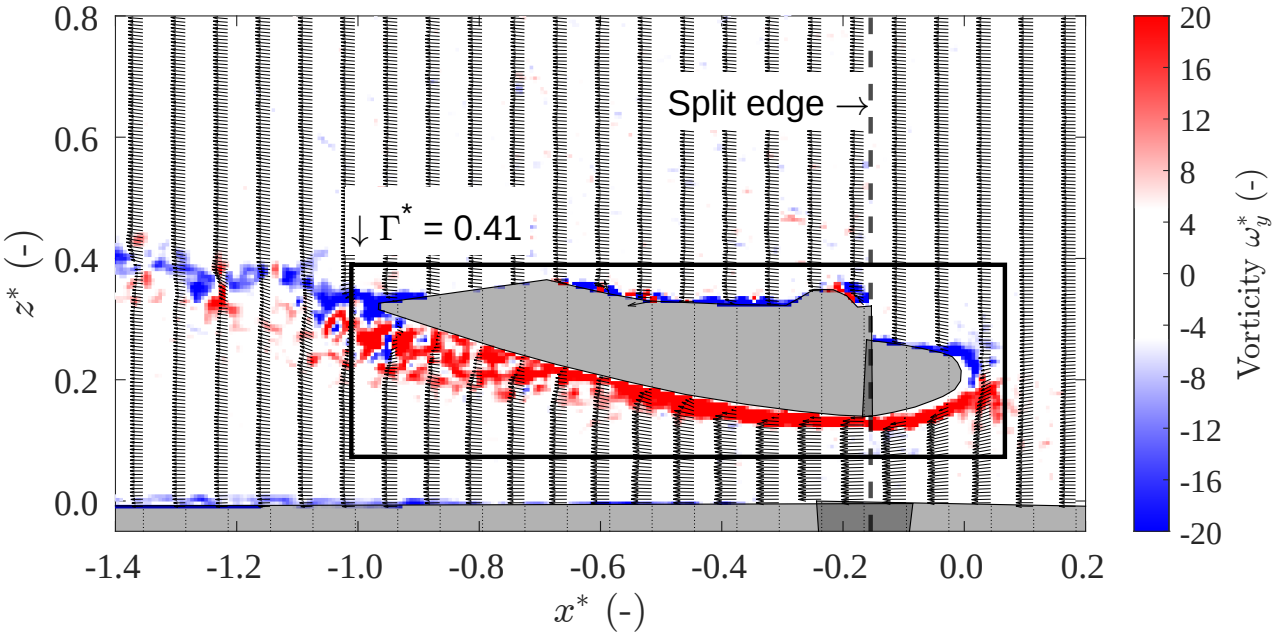

FIGURE 4.3: A typical result of PIV measurement at P_1, $H/C = 0.153$, $t^* = 2$, shown in non-dimensional coordinate. The origin point for z^* is set to be ground, and the origin point for x^* is set to be the leading edge of the wing. Flow fields measured by camera 1 and camera 2 are combined in 1 image, the split edge of cameras 1 and 2 is shown in the dash. Velocity distribution is shown in vectors by the vertical slice. Vorticity distribution is shown in contour. The area of the wing and the false bottom is masked by setting the velocity inside this area to 0. The masked area is shown in transparent grey. The control volume for defining circulation around the wing is shown in a rectangle. The circulation and vorticity are shown in non-dimensional form Γ^* and ω^* respectively.

The control volume shown in Figure 4.3 has been tested by changing the area of the control

volume. In the 4 other cases shown in Figure 4.4, one side of the control volume has been shifted with other edges holding their position. The top and bottom of the control volume have been shifted up and down respectively by 3 mm, and the left and right of the control volume have been shifted to the leading and trailing edge of the wing respectively.

As shown in Figure 4.4, different control volume shows the difference in downforce by $< 8\%$, and the error level remains the same in the whole interested timeline. The error level is considered to be acceptable. The chosen control volume (Figure 4.3) has the calculated result at around the middle value (shown in blue in Figure 4.4) of all results by other control volumes. The drop in force after $t^* = 7.4$ is due to the end of the false bottom, also shown in Figure 4.14.

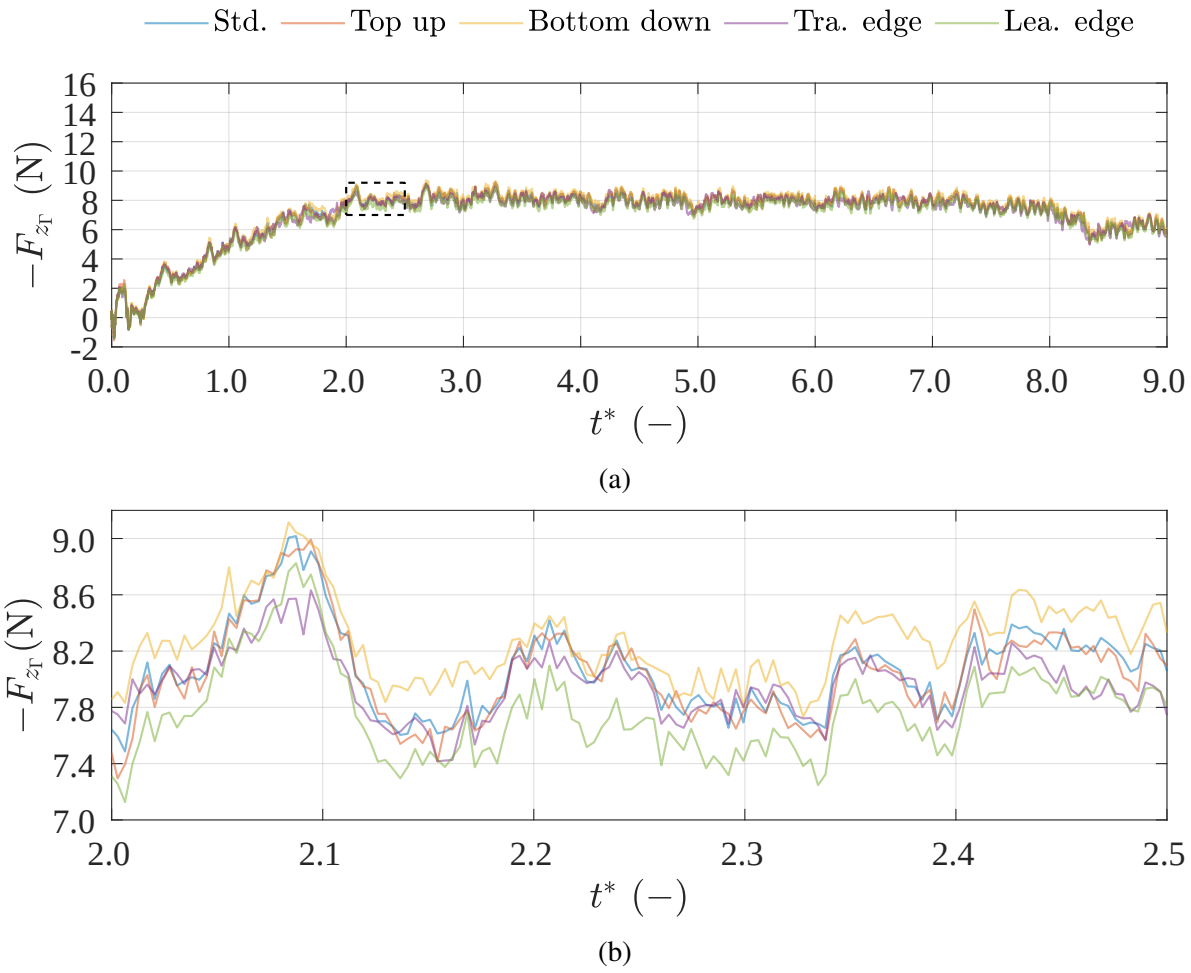

FIGURE 4.4: A typical result of downforce calculated by circulation F_{z_Γ} plotted by non-dimensional t^*. (a) F_{z_Γ} in whole interested timeline. (b) A zoomed-in plot of a rectangular area is shown in (a).

As shown in Figure 4.14, $F_{z_{\Gamma+AM}}$ shows a mismatch between $F_{z_{F/T}}$ right after acceleration phase ($t^* = 0.5$), and fits well after $t^* = 2$. Further discussion on the mismatched part will be shown in subsection 4.4.

4.2 Downforce measurement results

Downforce measurement was done at $\alpha = -6.60^\circ$ with the clearance to the ground as free parameters. 16 typical values of H/C were chosen to do experiments. For 4 clearances, the measurement was repeated by 18 times. According to the conclusion in Appendix E, the waiting time between experiments was chosen to be $T_{\text{gap}} < 1$ min to improve efficiency and reduce uncertainty with an acceptable systematic error $\mathcal{O}(1\%)$. The experiment was done with the clearance to the side wall $d_{\text{wall}}/C > 3$, which makes the wall effect negligible (further discussion see Appendix E).

Figure 4.5 shows a general view of recorded force signal.

The acceleration phase ends at $t^* = 1$, the initial peak comes later with the increment of clearance. For the free boundary layer, no obvious initial peak is observable at $H/C > 0.171$. For tripped boundary layer, the initial peak is observable for higher clearance until $H/C > 0.298$. At $t^* = 0$, there is an initial increment due to added mass shown in subsubsection 2.1.4. With higher clearance, the added mass effect is smaller, which agrees with the result shown in Figure 2.7. The drop behind the initial peak at $t^* = 1$ is also due to added mass. The drop is not obvious at higher clearance due to the reduction in added mass force, and the increment of circulation at the same moment, which could feedback the reduction in total measured force. compare with Figure 4.4a, after the drop, a secondary peak was found as a result of the increment of circulation and the vanish of added mass force.

At the transition phase (A phase between the acceleration phase and the steady phase), there is a gradual reduction in downforce for cases with an obvious initial peak. With the boundary layer tripped, the transition phase behaves very similarly among each other for clearance from $H/C = 0.054$ to $H/C = 0.126$. A similar flow field can be expected in this case. For cases with a free boundary layer, the downforce at the transition phase behaves differently in each case. A significant drop can be observed at $H/C = [0.054, 0.063, 0.081]$, and converged to a relatively small value of downforce.

At the steady phase, the downforce converges to a constant value, represents a fully developed flow. A average value of downforce at steady phase (from $t^* = 6$ to $t^* = 7$) with standard deviation is calculated to be the expectation and variance of downforce at steady phase at certain clearance. The calculation result is shown in Figure 4.6 and Figure 4.7.

At transition phase and steady phase, periodic oscillation can be found in downforce for all cases, which is due to periodic vortex which will be discussed in subsubsection 4.3.3.

As shown in Figure 4.6, the decrease of lift coefficient when moving closer to the ground when $H/C < 0.153$ could be due to the boundary layer mix [18]. The measurement result with $H/C > 0.153$ introduce the potential theory over predicts the circulation around the wing with ground effect, according to Equation 2.5, by ignoring the flow separation. Also, could be possible due to the rod used to connect the wing with the robot arm (shown in Figure 3.1a), the efficient spanwise is shorter than physical spanwise, which can introduce an under predict on the wing's lift coefficient. The wake region of the rod is visualized clearly at P_3. The Wagner effect introduced the circulation around a wing with impulsed start would generate 91% of the maximum circulation at $t^* = 6.5$ compared with at $t^* = \infty$ [25]. A correction on the Wagner effect has been done on the plots representing theoretical prediction results in Figure 4.6. Against the CFD result, the highest downforce was measured at $H/C = 0.171$, which is closer to the ground than $H/C = 0.298$ by CFD simulation. From $H/C = 0.171$ to $H/C = 1.13$, measured downforce is reducing faster with increasing clearance than CFD simulation. The error bar for lower clearance is generally higher than at higher clearance, which has relevance to the strength of vortex generated at different clearances, which will be discussed in subsubsection 4.3.3.

As shown in Figure 4.7, with tripped boundary layer, the recorded downforce is generally lower than in cases with a free boundary layer. The standard deviation of the measured downforce is larger than the free boundary later case, shown in the error bar. For $H/C = 0.054$ and $H/C = 0.063$, cases with tripped boundary layer result in a higher downforce. The constantly measured downforce at $H/C < 0.171$ with a large standard deviation could introduce a similar boundary layer mixing condition, introduced by a much higher boundary layer thickness compare with the clearance H. The generally larger standard deviation could be introduced by stronger periodic vortex, introduced by stronger boundary layer turbulence, which will be discussed in subsubsection 4.3.3.

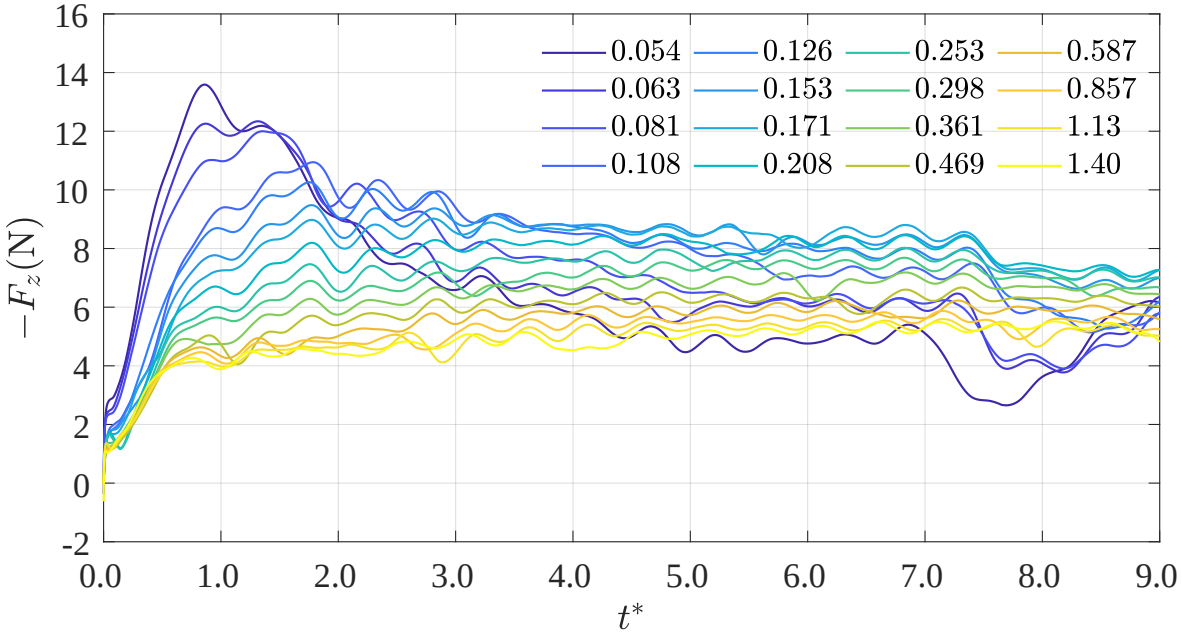

(a)

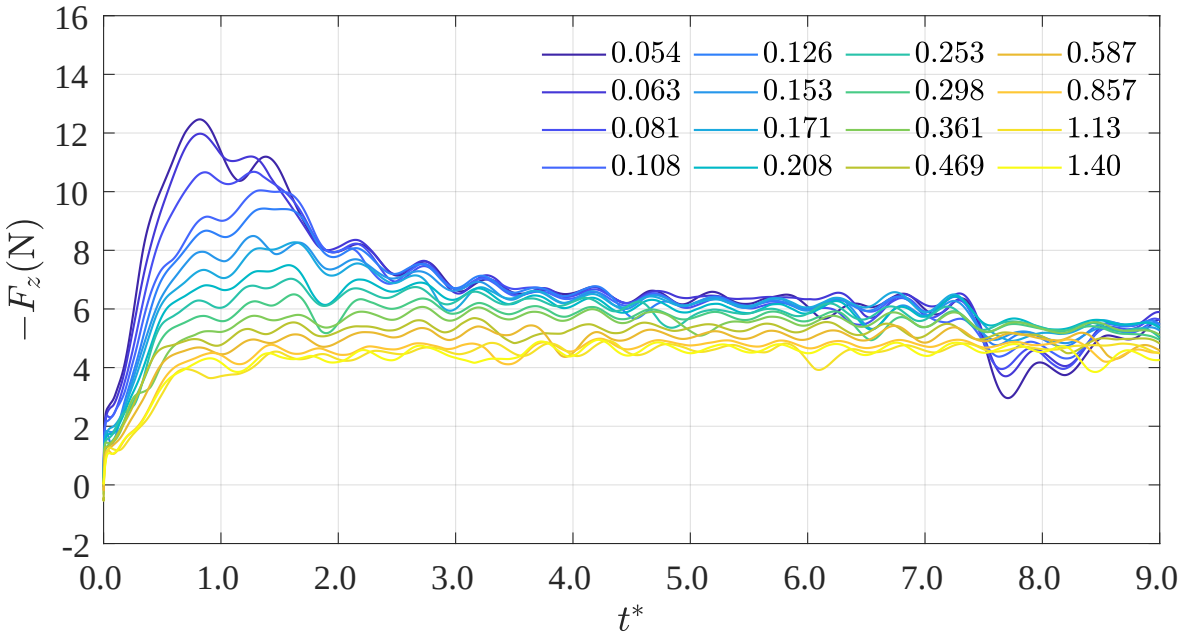

(b)

FIGURE 4.5: Measured and filtered downforce $-F_z$ during PIV measurement at all parameters in clearance with 2 boundary conditions, plotted by non-dimensional t^*. The clearance is shown in legend from $H/C = 0.054$ to $H/C = 1.40$. (a) Downforce at different clearances with a free boundary layer. (b) Downforce at different clearances with tripped boundary layer.

4.3 PIV measurement results

4.3.1 A general view of PIV measurement

Both acceleration phase, transition phase and steady phase are recorded by high speed cameras C_1 and C_2. A general view of the development of flow field with 2 different boundary layer condition is shown in Figure 4.8 and Figure 4.9. In the 2 figures, $t^* = 0.4$ (acceleration phase), $t^* = 2$, $t^* = 3.8$ (transition phase), $t^* = 5.5$ and $t^* = 7.3$ (steady phase) are chosen to shown in all chosen cases.

At the acceleration phase ($t^* = 0.4$), a starting vortex together with a stretched vortex connected with the trailing edge and pressure side of the wing can be found in all chosen cases. The strength of

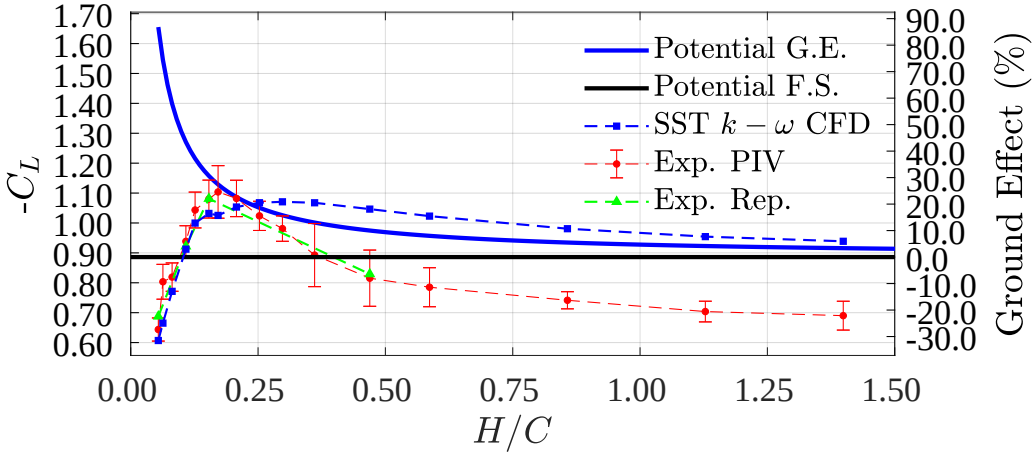

FIGURE 4.6: A comparison between the experimental result on lift coefficient C_L with different clearance to ground shown in H/C and predicted result by potential flow theory. The plots (in blue and black) were corrected by the Wagner function at $t^* = 6.5$. Similar inverse function behaviour can be found in experimental results at $H/C > 0.153$. For cases at $H/C < 0.153$, the lift coefficient is a positive correlation with clearance, which is against the prediction. The mean value of repeated measurement proves the reliability of measured results (in green). The error bar is shown by $\pm 3\sigma$. (The result by CFD was also plotted in this figure.)

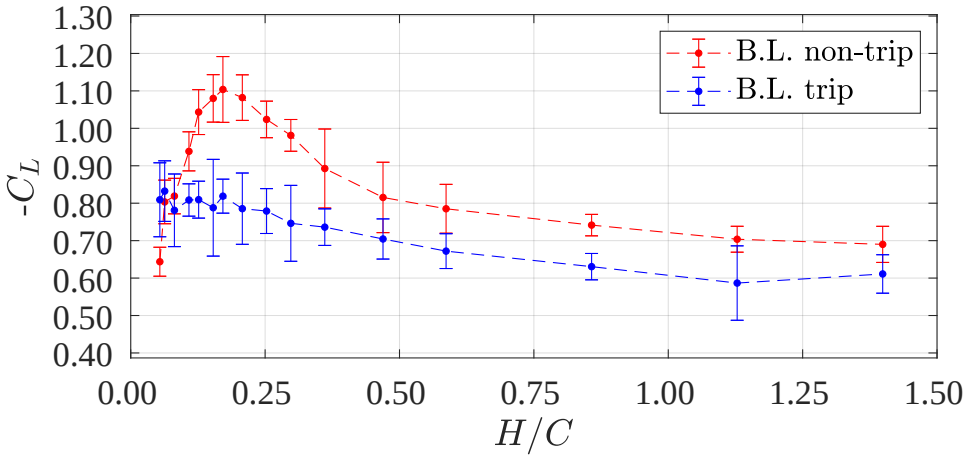

FIGURE 4.7: A comparison between downforce measurement results on lift coefficient C_L with different clearance to ground shown in H/C and different boundary layer conditions. Inverse function behaviour can be found in both results at $H/C > 0.153$. For the boundary layer tripped result at $H/C < 0.153$, the lift coefficient doesn't show a positive correlation with clearance, which is against the free boundary layer measurement. Instead, for the boundary layer tripped result, the lift coefficient stays as a constant around $C_L = -0.8$ at $H/C < 0.171$.

starting vortex remains the same in all chosen cases. The strength of the stretched vortex is reducing with the increment of clearance. The boundary layer at the suction side shows a larger thickness at lower clearance to the ground. (Can be seen in figure by non-dimensional vorticity's thickness and color shades lower than the wing's mask.) The higher vorticity shown at the boundary layer, represents higher kinetic energy in the boundary layer, which has a higher chance to develop into a turbulence boundary layer, which can be found in the future formation time ($t^* \geq 2$). At the same clearance, a boundary layer tripped case introduce stretched vortex with lower strength, which will be discussed in subsubsection 4.3.2.

At the transition phase ($t^* = 2, t^* = 3.8$), the development of wake region can be found in all chosen cases. At lower clearance, the wake region is larger in height, introduced by the flow separation point at the suction side moving from trailing side to leading side. This behavior corresponds to the

difference in suction side boundary layer at acceleration phase. The laminar boundary layer contains more energy will developed into turbulence boundary layer sooner than which contains less energy. At $H/C = 0.054$, the wake region has a strong contact with the false bottom. At $H/C = 0.108$, contact between wake region and false bottom is weaker. This kind of contact will introduce boundary layer mix, which could explain the drop in measured downforce shown in Figure 4.6 [18]. As shown in Figure 4.8a, Figure 4.8b, Figure 4.8c and Figure 4.5a, $t^* = 2$ has a higher downforce than $t^* = 3.8$, due to the stretched vortex is tangent to the suction side trailing edge, rather than the pressure side trailing edge. For the tripped boundary layer cases, flow separation point stick around a same point at suction side. The boundary layer mix between suction side boundary layer and the ground boundary layer is more unrecognizable compare with cases with free boundary layer at the same clearance, introduced by the tripped separation point and shape of wake region. Higher circulation around the wing can be investigated by less flow separation. The development of wake region will be discussed in subsubsection 4.3.3.

At the steady phase ($t^* = 5.5$, $t^* = 7.3$), the wake region of both cases are fully developed, and behaves close to $t^* = 3.8$ with larger wake region. Compare among Figure 4.8 and Figure 4.9, with boundary layer tripped, the wake region will be developed sooner, corresponding to a sooner convergence to a steady measured downforce as shown in Figure 4.5b. As shown in Figure 4.8, wing at a higher clearance has a smaller wake region. A clear boundary layer mix could be found in Figure 4.8a and Figure 4.8b. This behavior is due to Venturi effect under the wing, accelerates the flow to a different maximum speed at different clearance. A lower clearance expects a higher maximum speed. A higher maximum speed in flow, will introduce more energy in the wing's boundary layer, leads separation point closer to the leading edge, and a larger wake region is formed. If the separation point moved too far to leading edge, will lead to the boundary of wake region pointing to the ground downstream and finally interact with the boundary layer on the ground (also developed by Venturi effect). This kind of boundary layer mix will destroy the low pressure region right above the ground, which tents to "suck" the wing to it. As shown in Figure 4.8, Figure 4.6 and Figure 4.5a, this kind of boundary layer mix happens at $H/C < 0.153$, corresponding with the measured downforce drop at $H/C < 0.153$. As shown in Figure 4.9a, Figure 4.9b and Figure 4.9c, with tripped boundary layer, the wake region at $H/C = 0.054$, $H/C = 0.108$ and $H/C = 0.153$ has a similar behavior and no clear boundary layer mix can be found, corresponding to the similar measured downforce as shown in Figure 4.5b and Figure 4.5. At higher clearance, (as shown in Figure 4.9d and Figure 4.9e), more significant flow separation can be found compared with cases at the same height and free boundary layer, which will introduce lower downforce due to higher static pressure at the suction side, corresponding to measured downforce shown in Figure 4.5.

4.3.2 The acceleration phase

A zoom-in view of the acceleration phase, at $H/C = 0.054$, $H/C = 0.108$, $H/C = 0.153$, $H/C = 0.253$ and $H/C = 0.469$ is shown in Figure 4.10 and Figure 4.11 for cases with a free and tripped boundary layer respectively.

As shown in Figure 4.10a, Figure 4.10d, Figure 4.10g, Figure 4.10j and Figure 4.10m, the starting vortex is formed as a dipole around $t^* = 0.1$ by the mix of developing boundary layer at pressure side and suction side. The characteristic diameter of starting vortex is around $d_s = 0.1C = 11.08\,\text{mm}$ at $H/C = 0.054$, and reduced to around $d_s = 0.07C = 7.76\,\text{mm}$ at $H/C = 0.469$ with reduced strength, due to the reduced energy in boundary layer discussed in subsubsection 4.3.1. Similar behaviour can be found in cases with tripped boundary layer (as shown in Figure 4.11a, Figure 4.11d, Figure 4.11g, Figure 4.11j and Figure 4.11m).

Figure 4.10b, Figure 4.10e, Figure 4.10h, Figure 4.10k and Figure 4.10n show the development of starting vortex and the connected stretched vortex at $t^* = 0.45$. Forced by the stretched vortex, the position of starting vortex goes down by $0.05C$ from $t^* = 0.13$ to $t^* = 0.45$. The stretched vortex is formed by mixing the pressure side and suction side boundary layer. The boundary layer at the

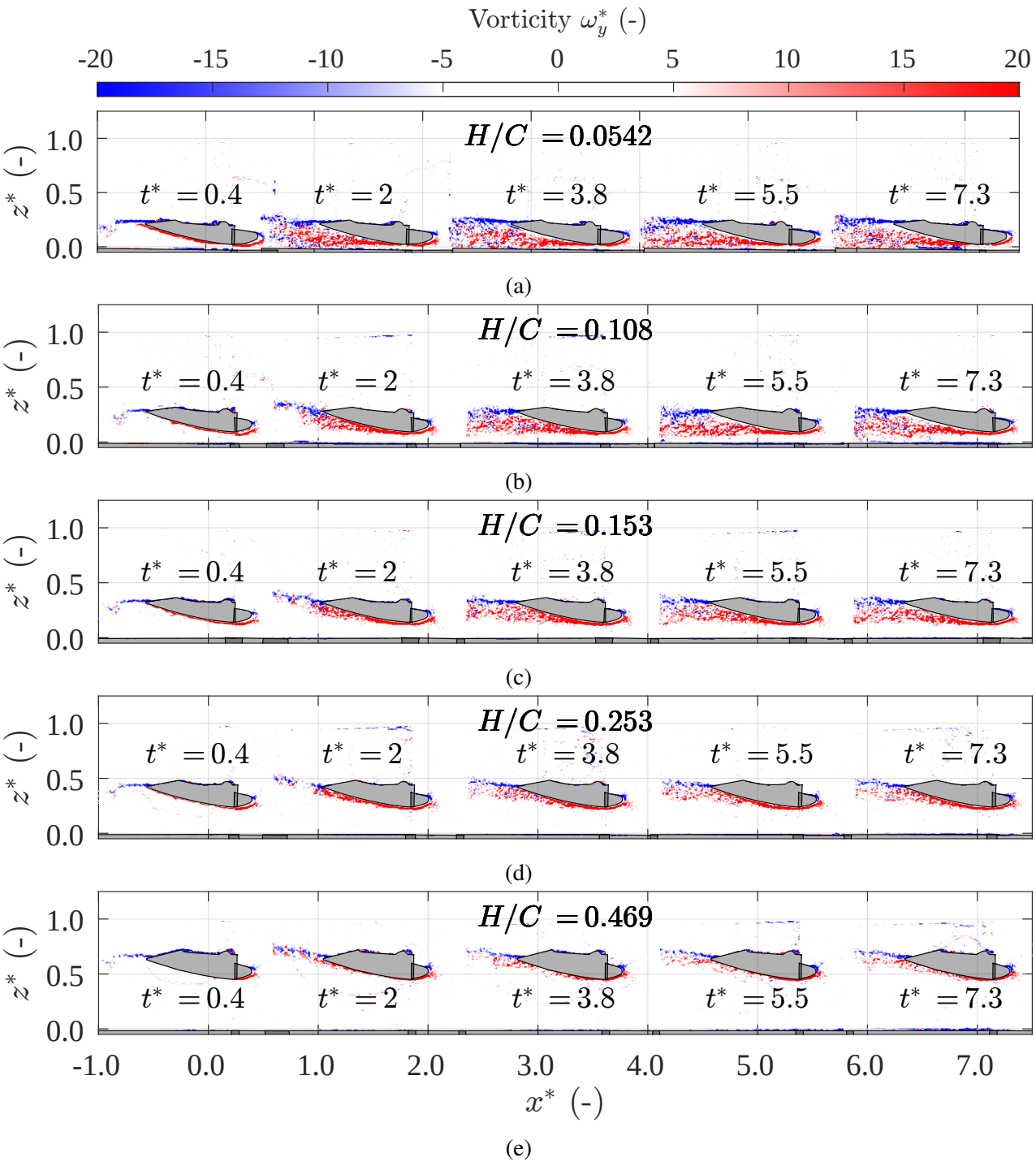

FIGURE 4.8: Dimensionless vorticity ω_y^* for different instances with free boundary layer in formation time t^* at the selected clearance (a) $H/C = 0.054$, (b) $H/C = 0.108$ and (c) $H/C = 0.153$, (d) $H/C = 0.253$ and (e) $H/C = 0.469$. The wing location x^* is based on the wing's leading edge matching the formation time t^*, i.e. $x^*(t^*) = t^*$. $x^* = 0$ is aligned with the leading edge at $t^* = 0$. $z^* = 0$ is aligned with the level of the false bottom for all cases.

pressure side is developed before the suction side boundary layer, due to the difference in geometry. The boundary layer at the suction side trailing edge tends to separate at the trailing edge. The flow velocity at the pressure size is larger than at the suction side trailing edge in magnitude. In this way, the stretched vortex is guided by the boundary layer at the pressure side. The boundary layer at the suction side is being developed and only tends to separate right before the trailing edge. In both cases, a trend of boundary layer dissipation has been shown by the non-linear vorticity distribution at the top of the boundary layer. The thickness of the suction side boundary layer is increasing in

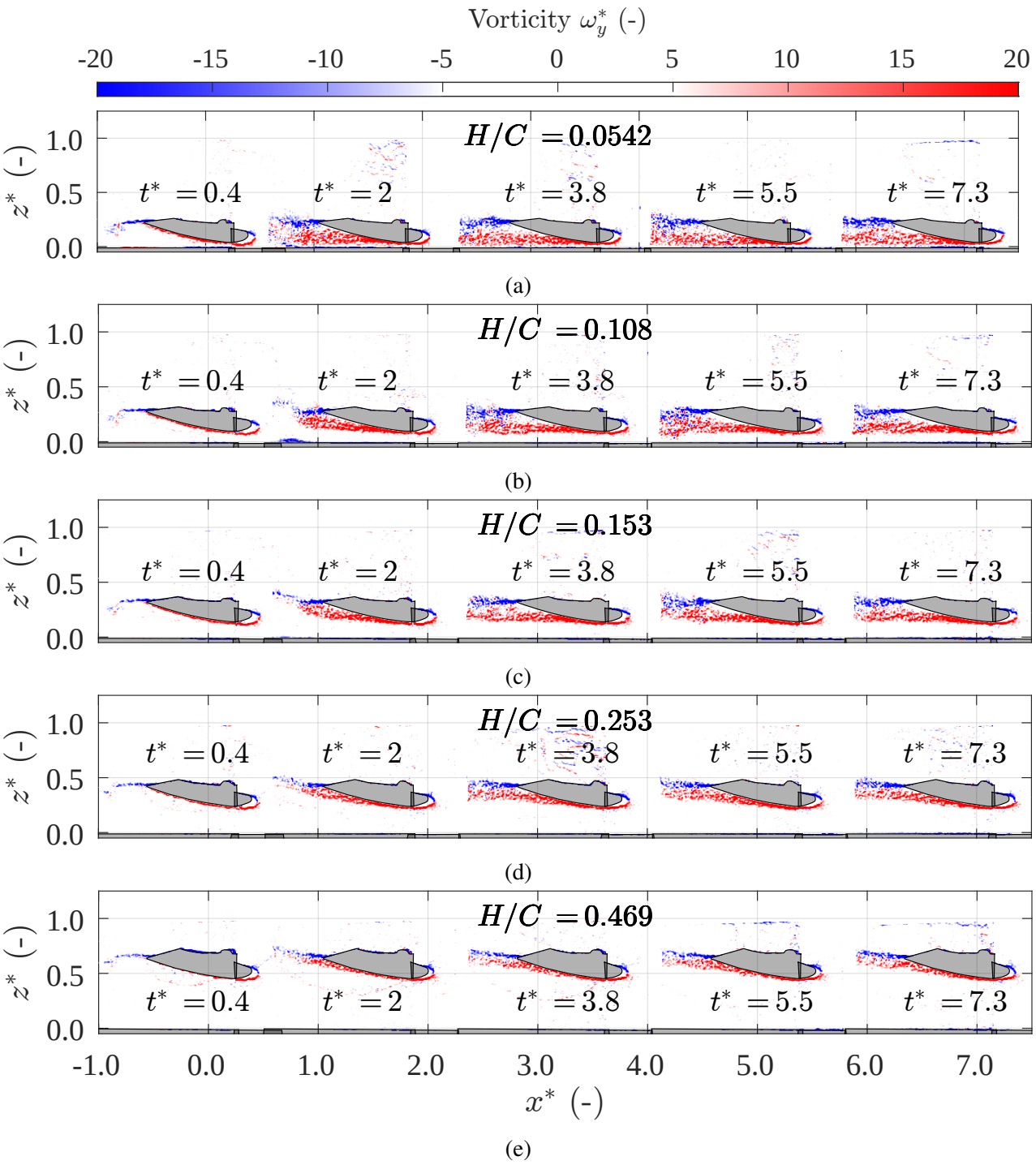

FIGURE 4.9: Dimensionless vorticity ω_y^* for different instances with tripped boundary layer in formation time t^* at the selected clearance (a) $H/C = 0.054$, (b) $H/C = 0.108$ and (c) $H/C = 0.153$, (d) $H/C = 0.253$ and (e) $H/C = 0.469$. The wing location x^* is based on the wing's leading edge matching the formation time t^*, i.e. $x^*(t^*) = t^*$. $x^* = 0$ is aligned with the leading edge at $t^* = 0$. $z^* = 0$ is aligned with the level of the false bottom for all cases.

both cases. At lower clearance, the boundary layer has a higher thickness, and the thickness of the boundary layer develops faster. At $H/C = 0.054$ and $H/C = 0.108$, a clear development of boundary layer on the false bottom can be seen, combined with 2 parts. The boundary layer under the wing has the same velocity direction as the wing's motion, due to the Venturi effect; the boundary layer behind the wing has an opposite velocity direction as the wing's motion, due to the low-pressure region created by the Venturi effect (under the wing) and developing wake region.

As shown in Figure 4.11b, Figure 4.11e, Figure 4.11h, Figure 4.11k and Figure 4.11n, with

tripped boundary layer, the starting vortex has a higher dissipation rate, due to higher turbulence energy contained. The suction side boundary layer shows a quicker development, introducing an instability of stretched vortex. As shown in Figure 4.11b, Figure 4.11e and Figure 4.11h, the stretched vortex dissipates into vortices with smaller characteristic diameters, due to higher turbulence energy contained, corresponding to the lower measured downforce at $H/C = 0.054$, $H/C = 0.108$ and $H/C = 0.153$ in Figure 4.5b comparing with Figure 4.5a. For higher clearance, no obvious difference in the stretched vortex can be found, corresponding to the similarly measured downforce in Figure 4.5b compared with Figure 4.5a.

Figure 4.10c, Figure 4.10f, Figure 4.10i, Figure 4.10l, Figure 4.10o show the development of wake region at the end of acceleration phase with free boundary layer at $t^* = 1$ respectively. At $t^* = 1$, the suction side boundary layer becomes thicker, and the boundary layer on the false bottom under the wing becomes longer with higher velocity, than at $t^* = 0.45$. The boundary layer on the false bottom behind the wing (in red) is being destroyed by the boundary layer in front of it. At $t^* = 1$ only the boundary layer under the wing can be seen, with a longer structure, and higher velocity, due to the increment in the wing's velocity, leading to a stronger Venturi effect (larger velocity difference in magnitude between the model and the flow at suction side geometrically lowest point). A significant dissipation of the suction side boundary layer is observed at $H/C = 0.054$ (Figure 4.10c), corresponding to the drop in force at $t^* = 1$ (shown in Figure 4.5a). With tripped boundary layer, a more significant flow separation can be found in Figure 4.11c, together with a reduced vortex on the false bottom. The more significant flow separation corresponds to the higher drop in force at $t^* = 1$ shown in Figure 4.5b, compared with Figure 4.5a. The restrain on the building of boundary layer on the false bottom introduces a less significant boundary layer mix with the suction side boundary layer, leading to a higher downforce at steady phase at low clearance as shown in Figure 4.5. The situation of the boundary layer mix will be further discussed in subsubsection 4.3.3.

For cases with higher clearance, no obvious boundary layer separation and dissipation is observed, corresponding to increment in measured downforce at $t^* = 1$ (shown in Figure 4.5a). The increment of velocity in the suction side boundary layer due to acceleration is higher than the velocity in the pressure side boundary layer, due to the Venturi effect. Due to the increment of velocity in the suction side boundary layer, at $t^* = 1$, the stretched vortex is influenced by the suction side boundary layer and starts to dissipate. This kind of dissipation starts with the forming of a vortex street, combined with a parallel same-direction vortex group spaced by a larger vortex opposite to the parallel same-direction vortex group. This flow structure is formed by Kelvin–Helmholtz instability at the both side of the stretched vortex. At higher clearance, the parallel same-direction vortex group has higher strength and characteristic diameter. The reduced flow separation introduced higher energy left in the boundary layer mixed with the pressure side boundary layer, forming a larger and stronger parallel same-direction vortex group. This kind of vortex could lead to the vibration in measured force as shown in Figure 4.5a, and will be discussed in subsubsection 4.3.3.

As shown in Figure 4.11c, Figure 4.11f, Figure 4.11i, Figure 4.11l, Figure 4.11o, similar vortex street can be found with lower strength in parallel same-direction vortex group, due to the higher dissipation rate in suction side boundary layer, turbulence energy at the suction side trailing edge is lower. By the higher dissipation rate, a trend of more significant flow separation can be found with tripped boundary layer, corresponding to the flow shown in Figure 4.9 at $t^* = 5.5$ and $t^* = 7.3$.

4.3.3 The transition phase

A zoom-in view of the transition phase, at $H/C = 0.054$, $H/C = 0.108$, $H/C = 0.153$, $H/C = 0.253$ and $H/C = 0.469$ is shown in Figure 4.12 and Figure 4.13 for cases with free and tripped boundary layer respectively.

Figure 4.12a, Figure 4.12d, Figure 4.12g, Figure 4.12j and Figure 4.12m show the development of vortex street at $t^* = 1.3$ with free boundary layer. In both cases, the parallel same-direction vortex group have a larger characteristic diameter and vortex strength with further distance in motion.

The suction side boundary layer develops thicker in time, representing higher velocity still being developed after acceleration. The higher clearance has a longer delay, which corresponds to the delay in the peak of downforce shown in figure Figure 4.5a. At $H/C = 0.054$, a clear boundary layer mix procedure between the suction side boundary layer and false bottom boundary layer can be found in $t^* = 1.3$ (Figure 4.12a), which reduces the circulation around the wing, introducing the huge drop in downforce. For other cases, a less significant boundary layer mix can still be seen, introducing less drop in downforce after the peak, as shown in Figure 4.5a.

With tripped boundary layer (as shown in Figure 4.13a, Figure 4.13d, Figure 4.13g, Figure 4.13j and Figure 4.13m) at $t^* = 1.3$, the vortex street has higher dissipation rate, with lower strength in parallel same-direction vortex group, due to the higher turbulence level at the forming wake region. At $H/C = 0.054$, the interaction between the suction side boundary layer and false bottom boundary layer is less, by the tripped suction side boundary layer having restrained on the development of false bottom boundary layer (as shown in Figure 4.13a). This effect can also be found at $H/C = 0.108$ with weaker strength, compared with Figure 4.12d and Figure 4.13d. At $H/C = 0.054$ and $H/C = 0.108$, less 3D flow structure can be found in Figure 4.13a and Figure 4.13d, comparing with cases at the same clearance with the free boundary layer. This can be observed by less opposite vortex in the suction side wake region for both cases.

Figure 4.12b and Figure 4.12c, Figure 4.12e and Figure 4.12f, Figure 4.12h and Figure 4.12i, Figure 4.12k and Figure 4.12l, Figure 4.12n and Figure 4.12o show transition of vortex street with parallel same-direction vortex group at $t^* = 2$ and $t^* = 2.2$ with free boundary layer respectively. A wake region with the shape at the steady phase is finally formed and will develop into the steady phase wake region by moving the flow separation point further to the front. At $H/C = 0.054$ and $H/C = 0.108$ the vortex street vanished by dissipation of the initial opposite direction vortex (in blue), and the pressure side boundary layer is decelerated more than the suction side. The flow from the pressure side is led to the suction side at $t^* = 2$, $H/C = 0.054$, as shown in Figure 4.12b. At $H/C = 0.153$ and $H/C = 0.253$, a clear gap between the end of the vortex street and the development of the final wake region can be found. (As shown in Figure 4.12h,Figure 4.12i, Figure 4.12k,Figure 4.12l.) This is due to the deceleration of the suction side boundary layer more than the pressure side boundary layer. At $H/C = 0.469$ the final wake region is developed by gradual delay of the forming of the bottom vortex in the parallel same-direction vortex group. In all cases, the transition of the vortex street is due to the deceleration of the boundary layers on both sides. The vortex of the mixing boundary layer shows a lower and lower frequency and converges to a constant frequency which corresponds to the periodic oscillation frequency in measured downforce as shown in Figure 4.5a.

Figure 4.13b and Figure 4.13c, Figure 4.13e and Figure 4.13f, Figure 4.13h and Figure 4.13i, Figure 4.13k and Figure 4.13l, Figure 4.13n and Figure 4.13o show transition of vortex street with parallel same-direction vortex group at $t^* = 2$ and $t^* = 2.2$ with tripped boundary layer respectively. A wake region with the shape at the steady phase is finally formed. At $H/C = 0.054$ and $H/C = 0.108$, less 3D flow structure can be found, and the boundary layer mix occurs less compared with the case at the same clearance and with free boundary layer (as shown in Figure 4.13c, Figure 4.12c, Figure 4.13f and Figure 4.12f). A fixed flow separation point is introduced by the tripped boundary layer. With different strengths of the Venturi effect, the separated flow goes at different velocities and develops different wake regions. With tripped boundary layer, the maximum strength of Venturi effect is fixed, introducing similar wake region structure and measured downforce at transition phase and steady phase at $H/C = 0.054$, $H/C = 0.108$ and $H/C = 0.153$, as shown in Figure 4.13f, Figure 4.13f, Figure 4.13c, Figure 4.5b and Figure 4.5. For higher clearance, the flow separation point is moved forward compared with cases at the same clearance with a free boundary layer, introducing a larger wake region, which will introduce higher static pressure at the suction side of the wing, leading to a lower generated downforce, corresponding to results shown in Figure 4.5.

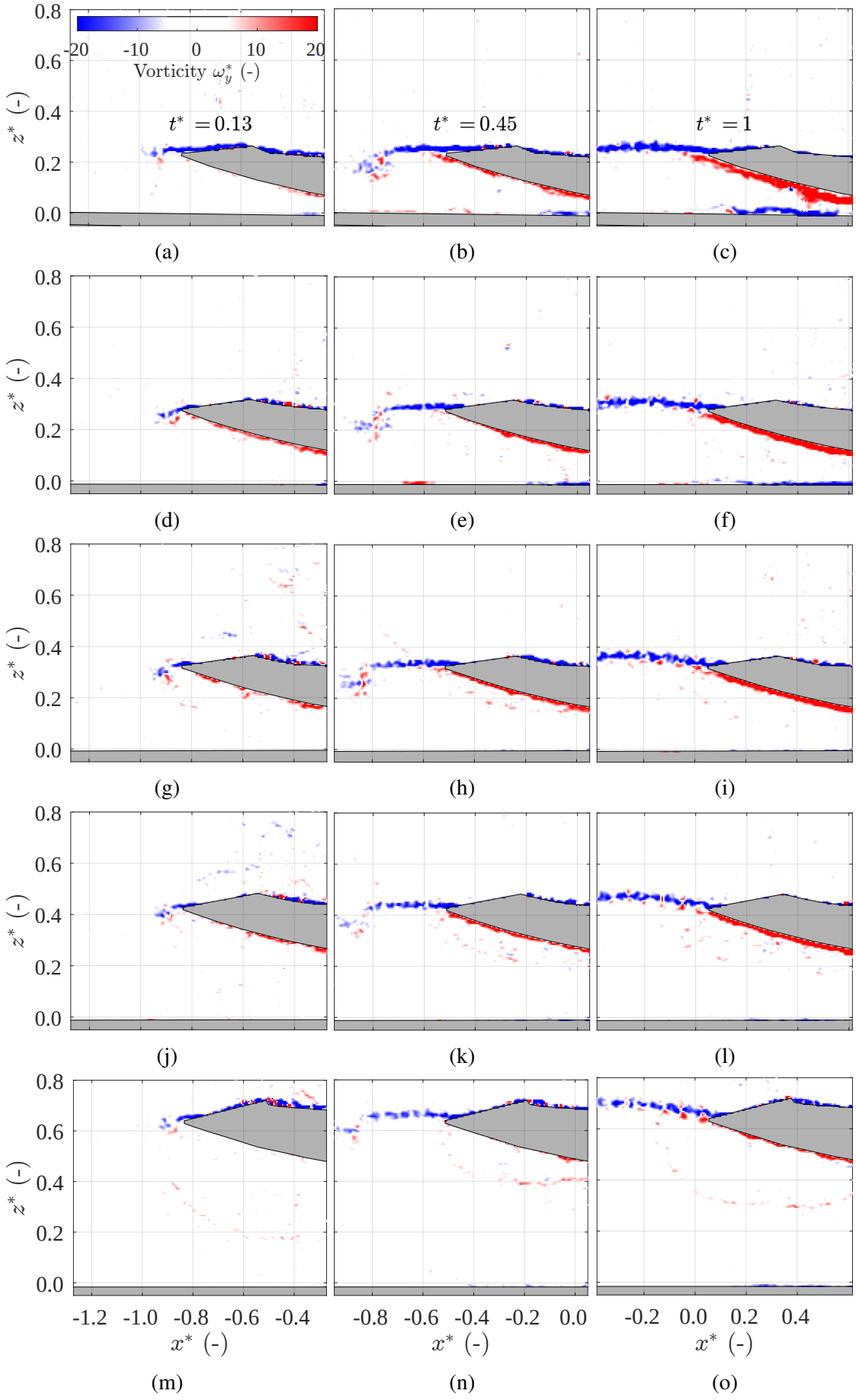

FIGURE 4.10: A zoom-in view of dimensionless vorticity ω_y^* in wake region with a free boundary layer at $H/C = [0.054, 0.108, 0.153, 0.253, 0.469]$ in the acceleration phase ($t^* < 1$). $x^* = 0$ is aligned with the leading edge at $t^* = 0$. $z^* = 0$ is aligned with the level of the false bottom.

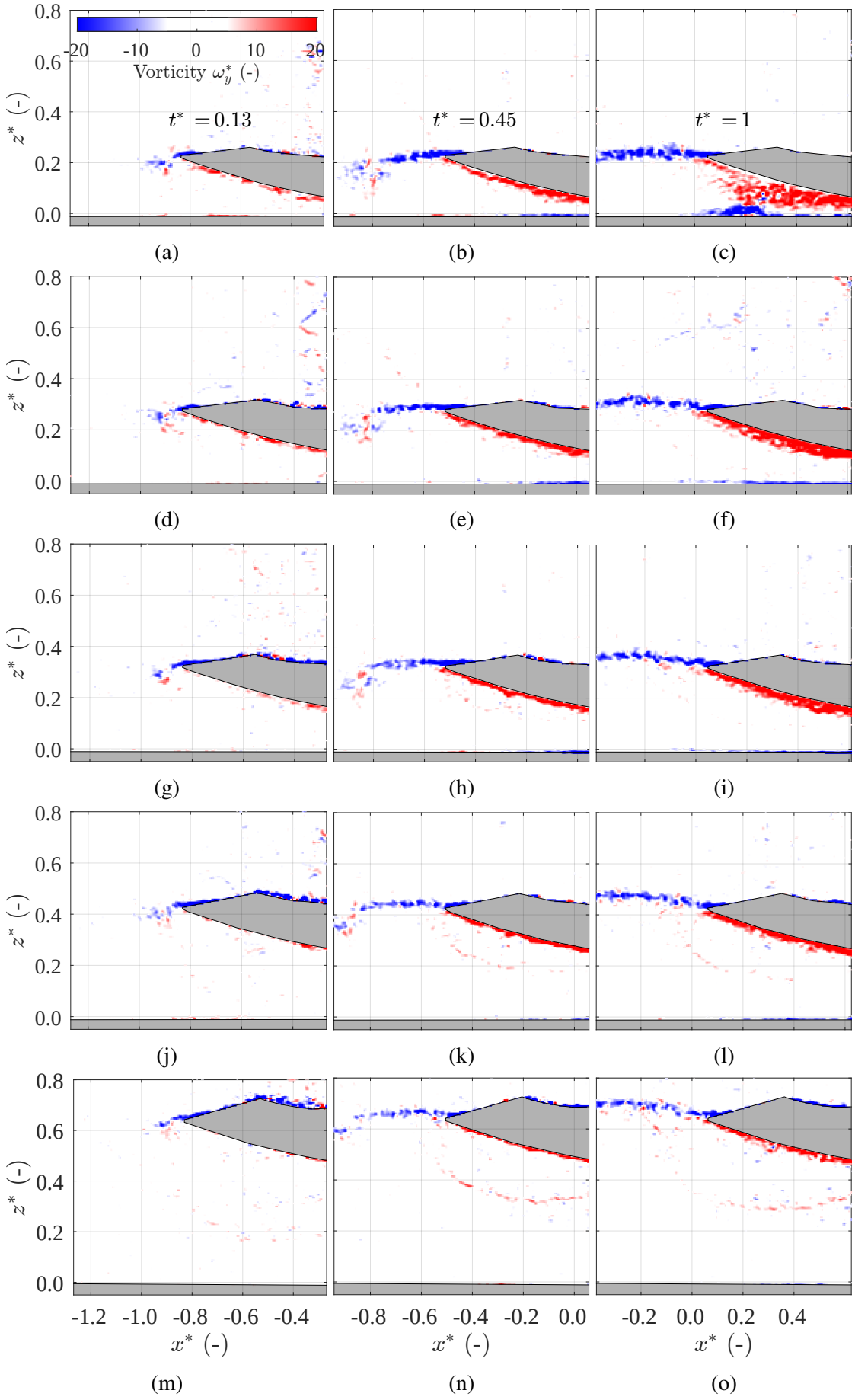

FIGURE 4.11: A zoom-in view of dimensionless vorticity ω_y^* in wake region with tripped boundary layer at $H/C = [0.054, 0.108, 0.153, 0.253, 0.469]$ in acceleration phase ($t^* < 1$). $x^* = 0$ is aligned with the leading edge at $t^* = 0$. $z^* = 0$ is aligned with the level of the false bottom.

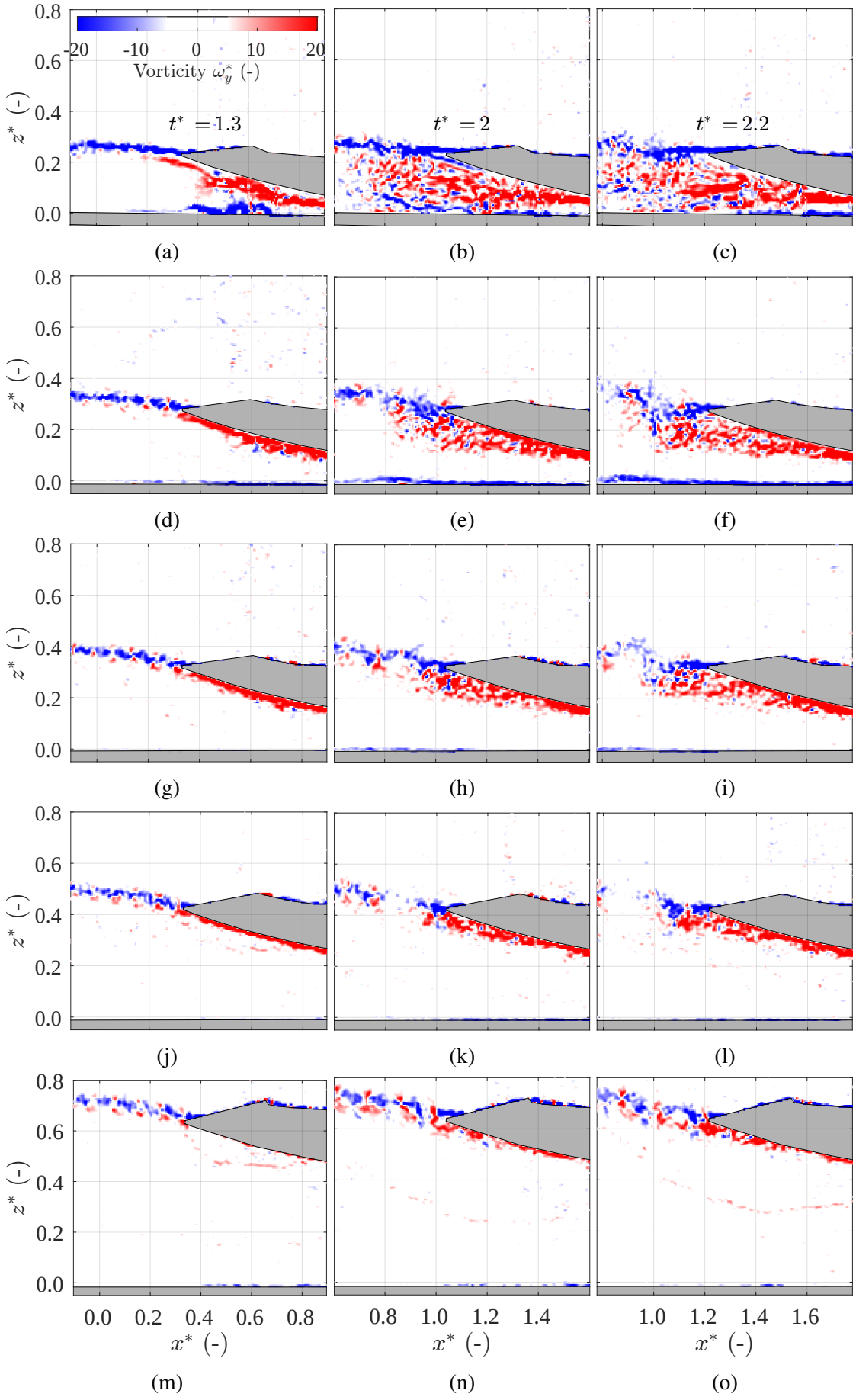

FIGURE 4.12: A zoom-in view of dimensionless vorticity ω_y^* in wake region with a free boundary layer at $H/C = [0.054, 0.108, 0.153, 0.253, 0.469]$ in transition phase ($t^* > 1$). $x^* = 0$ is aligned with the leading edge at $t^* = 0$. $z^* = 0$ is aligned with the level of the false bottom.

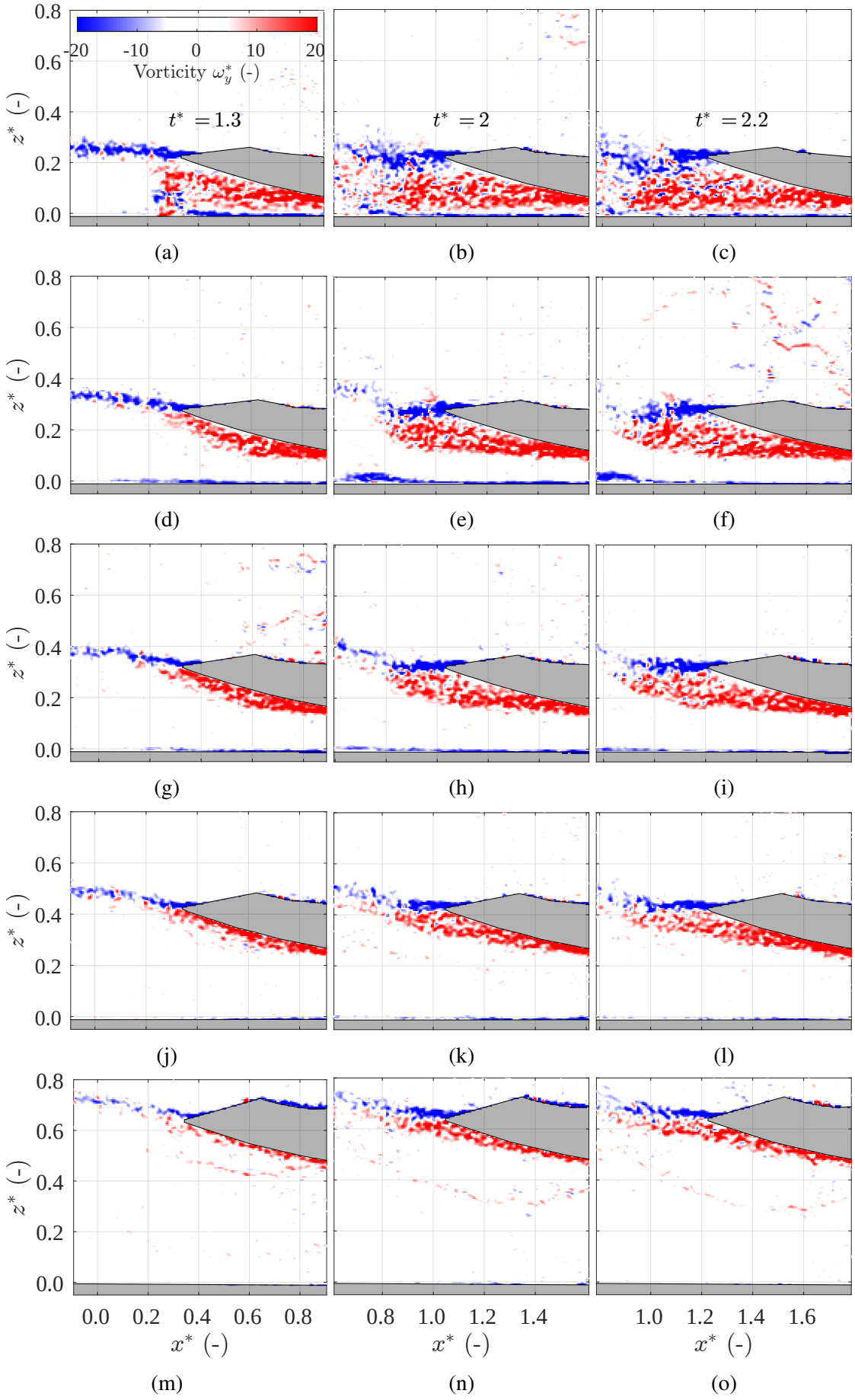

FIGURE 4.13: A zoom-in view of dimensionless vorticity ω_y^* in wake region with tripped boundary layer at $H/C = [0.054, 0.108, 0.153, 0.253, 0.469]$ in transition phase ($t^* > 1$). $x^* = 0$ is aligned with the leading edge at $t^* = 0$. $z^* = 0$ is aligned with the level of the false bottom.

4.4 The residual force (added mass force)

Based on the circulation Γ calculated from PIV measured velocity field, downforce $-F_{z_\Gamma}$ can be calculated by Equation 2.4, replacing the mean flow velocity Q_∞ by the recorded current velocity Q,

$$F_{z_\Gamma} = \rho Q \Gamma b_{\text{corrected}}, \tag{4.5}$$

where $b_{\text{corrected}}$ represents the corrected spanwise of the wing, calculated by Equation 4.6 [18],

$$b_{\text{corrected}} = \text{AR}C, \tag{4.6}$$

where AR is the corrected aspect ratio for the wing calculated by Equation 2.6[18].

As shown in Figure 4.14 and Figure 4.16, downforce calculated by circulation $-F_{z_\Gamma}$ is plotted by formation time t^* at P_1, $H/C = [0.054, 0.108, 0.153, 0.253, 0.469]$ (in green), together with added mass force $F_{z_{AM}}$ (in blue), added up of downforce calculated by circulation and added mass force $F_{z_{\Gamma+AM}}$ (in red), and unfiltered downforce signal recorded by F/T transducer $F_{z_{F/T}}$ (in black). The step response in $-F_{z_\Gamma}$ from $t^* = 0.05$ to $t^* = 0.10$ is due to the step response, which introduces vibration on the cameras C_1 and C_2.

At the steady phase ($t^* > 4$), $F_{z_{\Gamma+AM}}$, F_{z_Γ} and $F_{z_{F/T}}$ align well with each other at $H/C = [0.054, ... 0.108, 0.153]$ (see Figure 4.14a, Figure 4.14b, Figure 4.14c, Figure 4.16a, Figure 4.16b and Figure 4.16c). At higher ground clearance, a mismatch between $F_{z_{\Gamma+AM}}$ and $F_{z_{F/T}}$ can be found, with $F_{z_{\Gamma+AM}}$ and $-F_{z_\Gamma}$ align well with each other and smaller than $F_{z_{F/T}}$ (see Figure 4.14d, Figure 4.14e, Figure 4.16d and Figure 4.16e). The mismatch is due to the perspective of cameras C_1 and C_2 (see Figure 4.2), which introduces the missing of information close to the pressure side boundary layer of the wing.

At the acceleration and transition phase ($t^* < 4$), a mismatch between $F_{z_{\Gamma+AM}}$, F_{z_Γ} and $F_{z_{F/T}}$ can be found in all cases. A significant mismatch can be found in the acceleration phase ($t^* < 1$). The mismatch is shown as residual force $F_{mh_{\text{exp}}}$ calculated by Equation 4.7 (see Figure 4.15 and Figure 4.17),

$$F_{mh_{\text{exp}}} = F_{z_\Gamma} - F_{z_{F/T}}. \tag{4.7}$$

The mismatch is comparable with the added mass force introduced in subsubsection 2.1.4 with the time-dependent acceleration recorded by the robot arm (see Figure 3.2, in red). The time-dependent added mass force is plotted in Figure 4.15 and Figure 4.17 as another form of residual force $F_{mh_{\text{Brennen}}}$ [21] with formation time t^*, comparing with the residual force $F_{mh_{\text{exp}}}$. At the acceleration phase (after the step response, $0.5 < t^* < 1$), a plateau of residual force $F_{mh_{\text{exp}}}$ can be found. At the transition phase ($1 < t^* < 2$), the plateau value is reducing to a value around 0, and oscillating around this value at $t^* > 2$. Compare with the added mass force $F_{mh_{\text{Brennen}}}$, the residual force from experiments $F_{mh_{\text{exp}}}$ shows a delay of $|t^*| = 1$ with $Q = Q_\infty$ in reduction to 0. The reduction only occurs after the acceleration phase ($t^* > 1$).

At $H/C = [0.054, 0.108, 0.153]$, the plateau value of $F_{mh_{\text{Brennen}}}$ is within an error of ± 1 N comparing with the plateau value of $F_{mh_{\text{exp}}}$ (see Figure 4.15a, Figure 4.15b, Figure 4.15c, Figure 4.17a, Figure 4.17b and Figure 4.17c). At $H/C = [0.253, 0.469]$, the plateau value of $F_{mh_{\text{Brennen}}}$ is within an error of ± 1 N, comparing with the gap between the plateau value and the reduced value at $t^* > 2$ of $F_{mh_{\text{exp}}}$.

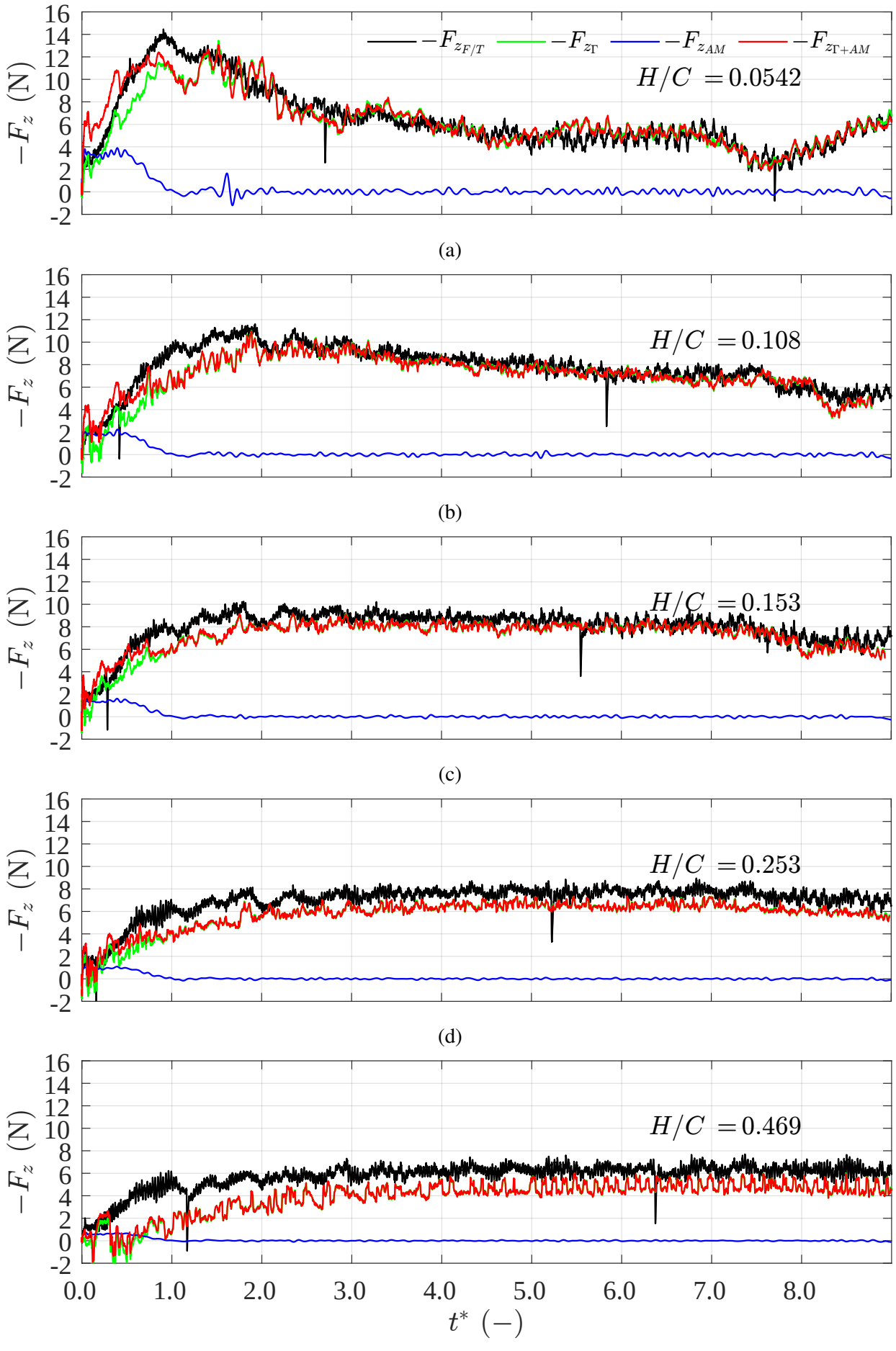

FIGURE 4.14: Downforce at different H/C in cases with a free boundary layer.

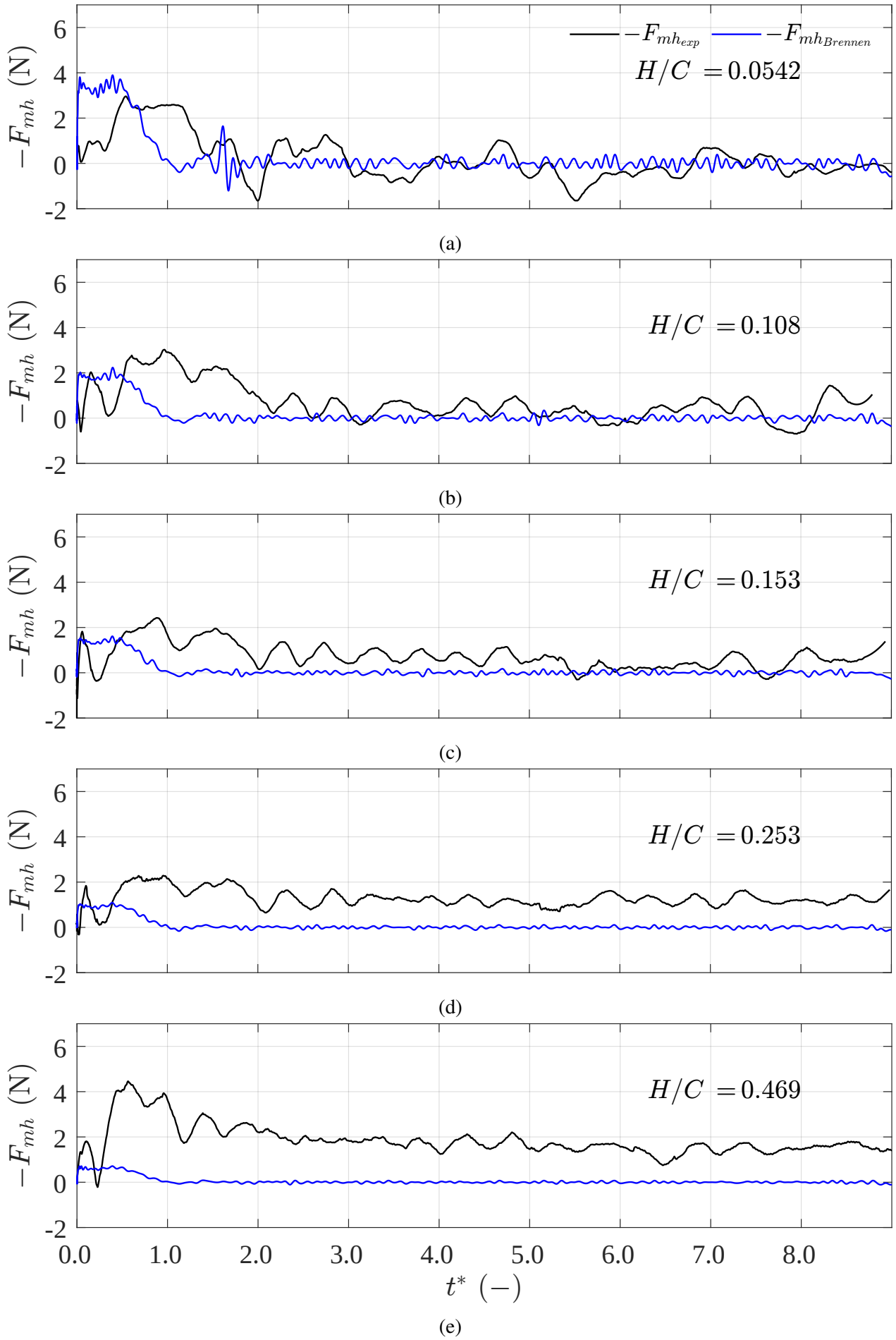

FIGURE 4.15: The residual force in dimensional form (cases with a free boundary layer).

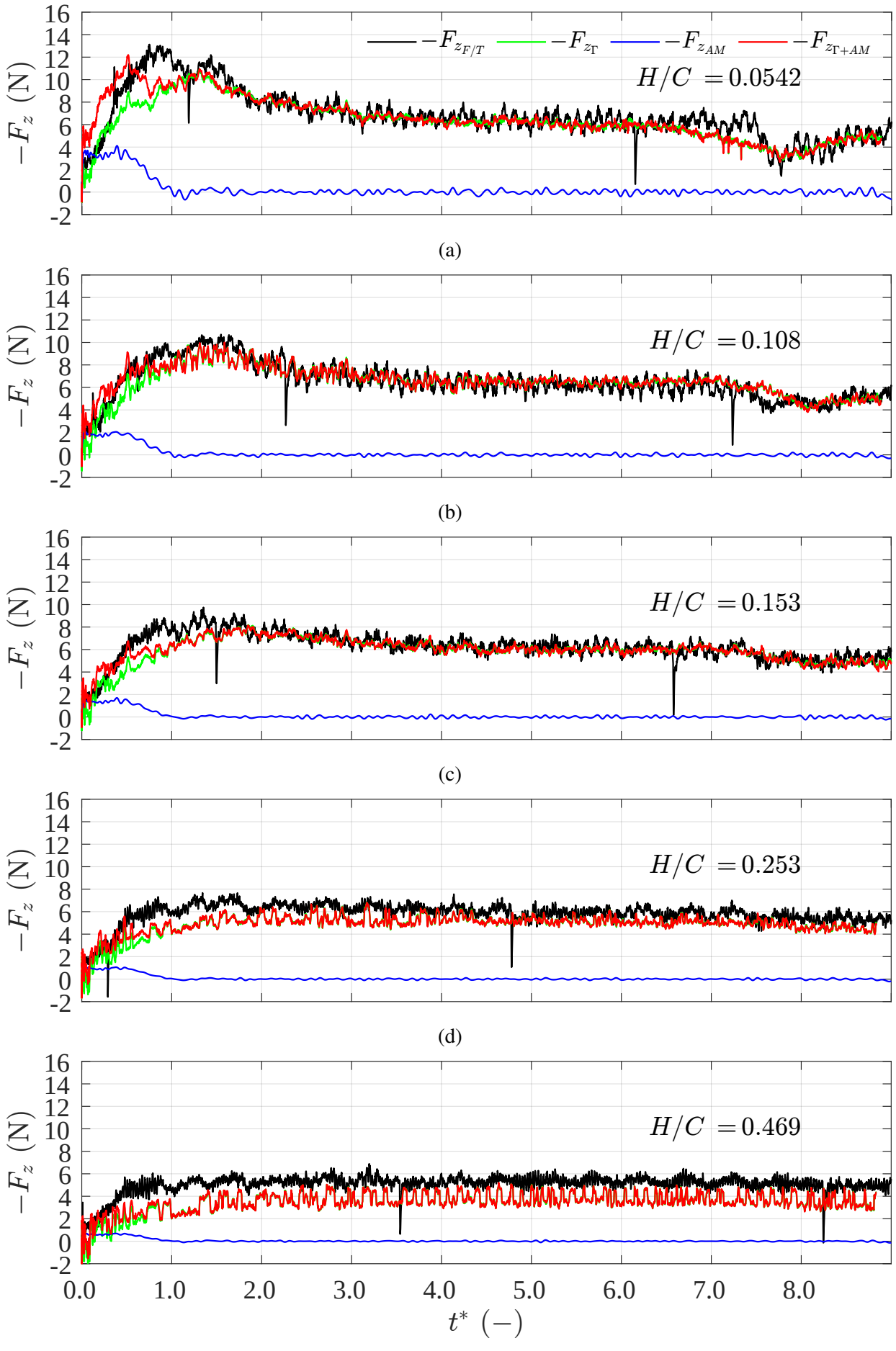

FIGURE 4.16: Downforce at different H/C in cases with tripped boundary layer.

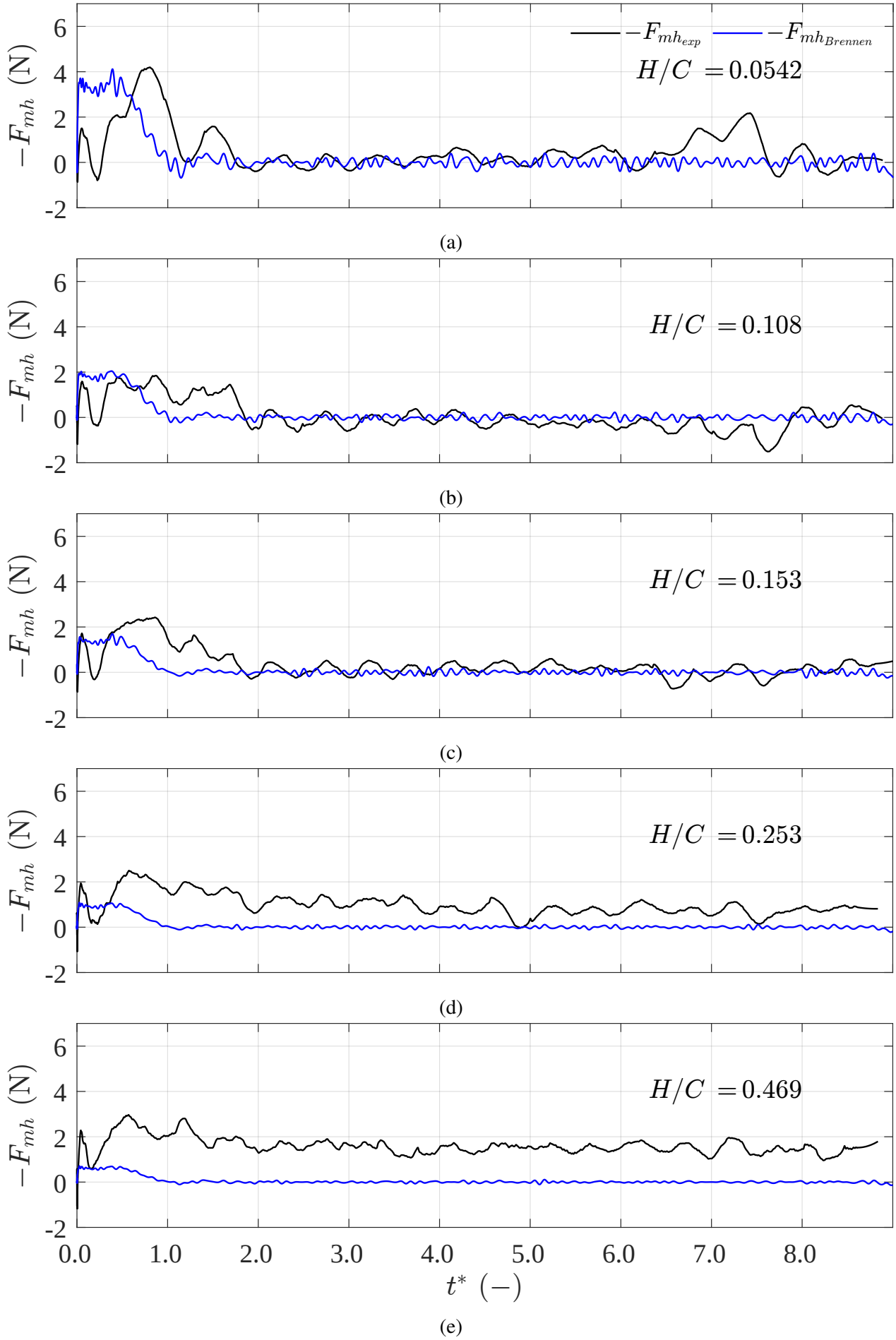

FIGURE 4.17: The residual force in dimensional form (cases with tripped boundary layer).

5 Discussion

The flow field around the wing is predicted by potential flow theory and CFD simulation with two different turbulence models. Compare with the flow field by PIV measurement, Figure 2.6 shows the distribution of streamlines around the wing with ground effect. At low ground clearance, a significant flow acceleration can be found at the suction side of the wing, which is opposite to the flow behaviour observed in CFD simulation and PIV measurement. In potential flow, viscosity effect is ignored, boundary layer is not applied to the wing. The flow behaviour introduced by boundary layer can not be predicted. No flow separation can be found in the flow field introduced by potential flow theory. The difference in the prediction of boundary layer, introduces the opposite behavior in the steady phase down force at low ground clearance (see Figure 4.6). Without any flow separation, the potential flow theory predicts flow fields close to the PIV-measured accelerating flow field (see Figure 4.10 and Figure 4.11), providing reliable results in added mass matrix shown in subsubsection 2.1.4.

The 2D-CFD with the SST $k-\omega$ turbulence model predicts similar flow separation and the wake region behaviour at the ground clearance $H/C < 0.253$, comparing with the PIV measurement results (see Figure 2.9 and Figure 4.8), corresponding to the alignment in CFD predicted and F/T transducer measured steady phase downforce (see Figure 4.6). At the ground clearance $H/C > 0.253$, the over-prediction of the flow acceleration effect (the Venturi effect) at the suction side of the wing, introduces the over-prediction in steady phase downforce (see Figure 4.6). The over-prediction of the Venturi effect is introduced by the SST $k-\omega$ model suppressing the turbulence diffusion [29]. The matching trend and values between SST $k-\omega$ and downforce measurement, prove similarity in the trend of pressure distribution and wall shear stress distribution between CFD and PIV results (see Figure 2.12 and Figure 2.11).

The 2D-CFD with DES turbulence model predicts the mixture between the suction side and the ground boundary layers at the ground clearance $H/C < 0.253$; and the Kevin-Helmholtz-like instability at higher ground clearance, introduced by the pressure side and suction side boundary layer (see Figure 2.10). The non-converging 2D DES simulation introduces a highly 3D flow structure that could be expected in experiments [14]. The predicted flow behaviour is matched by PIV measurement results shown in subsection 4.3.

In the flow field measured by PIV, compare with the SST $k-\omega$ and DES CFD results, a smaller turbulence structure can be observed, corresponding to a homogeneous turbulence flow (highly 3D flow structure) at the wake region of the wing (see Figure 4.8).

At the acceleration and transition phase, Kevin-Helmholtz-like instability can be observed, developing from a stretched vortex connected to the trailing edge of the wing, introducing the vibration in measured downforce F_z at $t^* < 2$ (see Figure 4.10, Figure 4.12 and Figure 4.5a). The measured residual force $F_{mh_{\text{exp}}}$ is not matching well with the added mass force introduced by Brennen $F_{mh_{\text{Brennen}}}$ [21]. With downforce calculated by circulation F_{z_Γ} matching well with the downforce measured by F/T transducer $F_{z_{F/T}}$ at $t^* > 2$, the mismatch is introduced by the misalignment in the model of residual force (see Figure 4.15).

With the tripped boundary layer, at ground clearance $H/C \leq 0.063$, higher downforce and less significant boundary layer mixture between the suction side and the ground boundary layer can be observed. Due to the fixed flow separation point, which is closer to the trailing edge compared with the case at the same ground clearance, a free boundary layer (see Figure 4.9). The fixed flow separation point introduces the steady phase downforce is higher than without tripping the boundary layer, by the reduction of boundary layer mix (see Figure 4.5). At the ground clearance $H/C > 0.063$, a reduction in steady phase downforce is observed compared with cases with a free boundary layer, introduced by the fixed flow separation point moving further to the trailing edge. For cases at $0.063 < H/C < 0.361$, the reduction on steady phase downforce is also introduced by the reduction of boundary layer mix (see Figure 4.5). Introduced by higher turbulence dissipation rate around the wing, the turbulence level around the wing is higher, introducing a more significant vibration

in measured downforce and a larger error bar in the steady phase downforce (see Figure 4.5b and Figure 4.5).

6 Conclusion

In this research, PIV measurements with the acceleration and the ground effect around an F1 car's front wing are done. Potential flow theory and CFD results are used to predict and explain the flow and downforce behaviour around the wing.

With the increment of the ground clearance H/C, a peak of the steady flow downforce is measured around $H/C = 0.153$ with a free boundary layer. With tripped boundary layer, no peak of the steady flow downforce is measured. In the acceleration phase, at lower ground clearance, the observed higher peak in downforce, occurs earlier in time. The initial peak in time is aligned with the end of acceleration phase, due to the transition from laminar to turbulence boundary layer at the suction side of the wing (see Figure 4.10 and Figure 4.11). This introduces a lower ground clearance could make a larger advantage in downforce for an accelerating F1 car. On track, the effect of steady flow can be ignore (see Figure 3.2 and Figure A.1).

The added mass force given by potential flow theory [21] shows a trend matches with the measured residual force F_{mh} in value, with an error of ± 1 newton. In time series, a mismatch can be seen, with measured residual force F_{mh} last for a longer time (until $t^* = 2$, in stand of $t^* = 1$ or at the end of acceleration phase). Due to the step response in cameras, residual force measured before $t^* = 0.5$ is unreliable.

For the future research on the accelerating flow, the step response should be avoid on all components relevant to the measurement. To get a more completed flow field around the wing, cameras looking at the pressure side of the wing should be applied to the measurement system. Since 3D structure has been found (see Appendix F), stereo-PIV or 3D-PIV should be applied on this topic. To get a better prediction on the residual force, higher order function should be applied, considering the historical effect in time series after the end of acceleration.

Apart from the acceleration effect, the deceleration effect and cornering effect are other topics to do research on.

To improve the racing performance, the acceleration, deceleration and cornering effect on the drag force should be taken into account.

A The Relative Importance of Aerodynamic for F1

Enzo Ferrari has a famous quote,"Aerodynamics are for people who can't build engines [30]."

In someway Enzo's quote is true. There are 6 main performance parameters for F1 cars, shown in the following list[3].

- Grip from tyres, suspension, etc.
- Vehicle mass
- Centre of gravity
- Engine and transmission of power
- Electronics, hydraulics, pneumatics
- Aerodynamics

From modern lap-time simulation, teams have learned that, very roughly, if they could change the performance parameters by a percentage, then they would have roughly the following effects on lap times as shown in Table 1.1. The starting point is a 2013 generation of F1 car on an average 2013 race track. If the race track or the start point changes, these values will change.

According to Table 1.1, it's clear that aerodynamic is not the most effective performance parameter to the general performance of a F1 car. (Also not engine and transmission of power.)

However it also depends on what you are permitted to change and on how much effort it takes to make the change. In fact, F1 racing is governed and sanctioned by a world organization called the Fédération Internationale de l'Automobile (FIA) or the International Automobile Federation (in English) [4]. There is not much room to differentiate in the design of the engine, tyres, electronics or mass of F1 cars [5].

Aerodynamics affect the F1 car's performance in a different way from other performance parameters. As shown in Figure A.1, shows how downforce and drag can influence the limit speed of a 2013 Sauber Ferrari F1 car, over part of a lap of the Barcelona track (including from the entering turn 1 and turning out of turn 5), from normal to no downforce or normal to 25% of normal drag. The curves are created using lap-time simulation software, which is regularly validated and improved against real-car performance. It is assumed that other parameters such as suspension and tyres are at the same performance level.

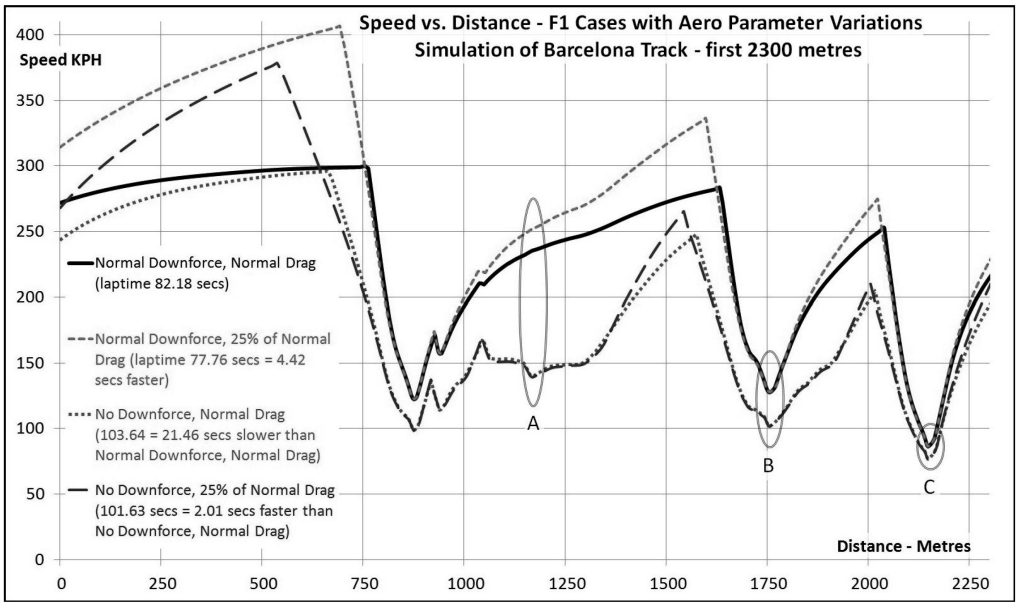

FIGURE A.1: Influence of drag and downforce on the limit speed of an F1 car [3].

In Figure A.1, 3 typical sections were pointed out. Section A represents a high speed corner, section B represents a middle speed corner and section C represents a low speed corner. It can be seen that the influence of downforce becomes significant at high speed corners. Also, the influence

of drag or downforce don't have a significant effect on accelerating rate. Since most modern F1 race track has lots of high speed corners, where are quite often an overtaking point, the high speed corner performance is important in most case for a F1 car. (A good example is shown in Figure A.2a, Circuit de Barcelona-Catalunya.) So that the research on aerodynamics is important.

This also proved Enzo Ferrari was right in an opposite way. He said that famous quote at the 24 Hours of Le Mans, where the race track was almost straight lines (shown in Figure A.2b), which made aerodynamic not as important as engine performance. And the truth is Ferrari won the race, by Ferrari 250 TR with a very vertical windshield (could expect a bad aerodynamic performance).

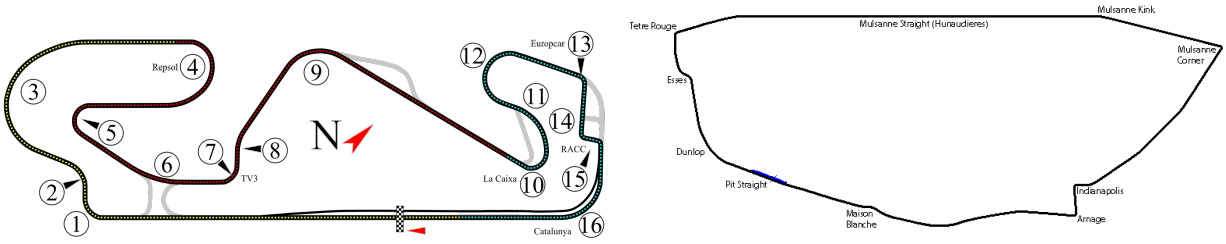

(a) (b)

FIGURE A.2: a) F1 Circuit de Barcelona-Catalunya 2021 [31]. b) Le Mans Circuit de la Sarthe 1932-1967 [32].

In conclusion, aerodynamic is important for F1 cars in three ways. Technically, the aerodynamic is ranked the forth important performance parameter, refer to Table 1.1. Realistically, due to the rule of F1 racing, aerodynamic has the most room to differentiate in the design among racing teams, which means the aerodynamic part is far more important than "the forth important" in real case. Practically, high speed corners are common is F1 racing, aerodynamics have a significant effect on high speed cornering performance of F1 cars. Realizing the importance of aerodynamic, since the 1960s, teams have used downforce-creating wings to push cars into the track to create more grip. The goal of aerodynamic development is to create more downforce without a corresponding increase in drag [6].

B Flow Measurement Methods

B.1 Comparison of Flow Visualization/Measurement Methods

As shown in Table B.1, several flow visualization/measurement methods were analyzed. As a result, small particle method is considered to be the most suitable method and chosen to apply for this research. The specific name of method will be used is Particle Image Velocimetry (PIV) method, since the information of flow parameter is considered to be important. PIV is the only method can directly get the velocity field.

B.2 Particle Image Velocimetry (PIV) Method

The goal of PIV is to measure instantaneous planar (2D) or volumetric (3D) velocity distribution (time-resolved) in a flow.

PIV uses the images of the displacement of tracer particles to represent local fluid velocity. It first divide image pair in interrogation regions, where the flow motion is considered to be approximately uniform. The computation of 'average' displacement is done within interrogation window to get a velocity data (magnitude and direction) [44].

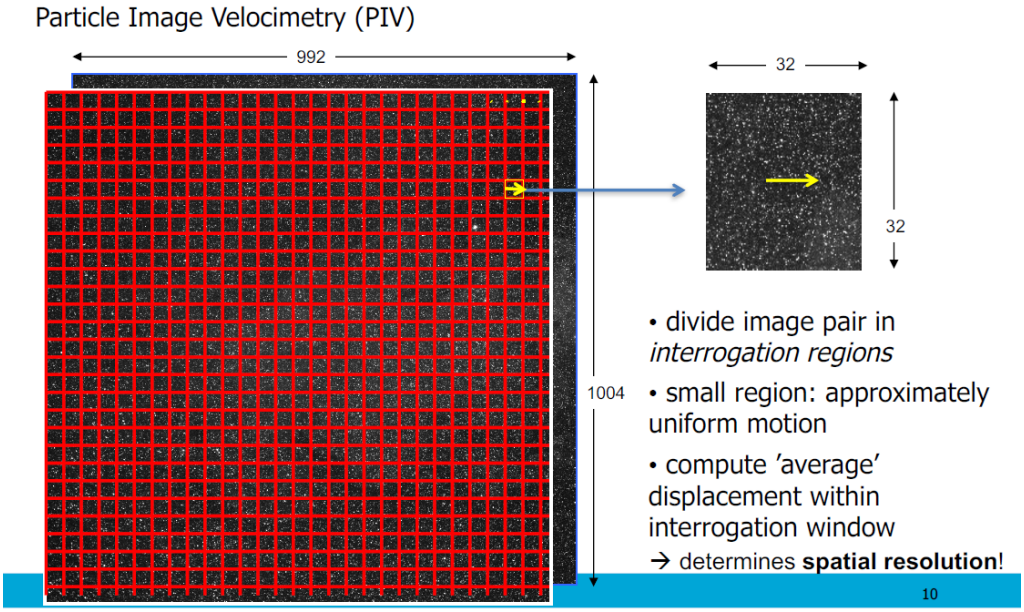

FIGURE B.1: Get local fluid velocity from imaging of the displacement of tracer particles

The PIV data can be also used for force, pressure measurement and flow structure detection.

TABLE B.1: A advantages and drawback analysis of flow visualization/measurement methods for this research.

Type		Name	Advantage	Drawback
Off-surface Methods	Tracer Methods	Smoke Method	• Volumetric light source [33]	• Hard to get velocity information
		Dye Method	• Easy to visualize in water [34]	• Need stability with respect to diffusion [34]
		Small Particles Method	• Accurate velocity measurement • Non-intrusive[35]	• Need to use optical equipment [35]
		Gas Bubble Method	• Volumetric light source [36]	• Limited observation time [36]
	Optical Methods	Shadowgrath Method	• Compressible air field as an optical object [37] (Don't need tracer)	• More suitable for compressible flow (flow medium density difference larger than 2%) with $M_\infty > 0.2$ [37]
		Schlieren Method		
		Interfero--metry Method		
Tuft Method		Tuft Method	• Easy to visualize • Unrestricted Experimental Environment (outside of wind tunnels) [38]	• Hard to get quantitative analysis of transient flows and the dynamic structures [39] • Significant influence from buoyancy in water
Surface Method		Surface Oil Film Method	• Shows information on separation and reattachment of the flow [40]	• Can't be used in water
		Liquid Crystals & Temperature Sensitive Paint (TSP) Method	• Liquid crystals method is sensitive to small temperature change • TSP allows more temperature span [40]	• Liquid crystals apply in high temperature environment [40] • TSP is not sensitive to small temperature change (less than 1 °C) [41]
		Pressure Sensitive Paint (PSP) Method	• Low response time, can be used to unsteady flow measurement • High resolution (= resolution of camera) [42]	• Not sensitive to small pressure gradient [43] • Based on oxygen quenching of luminescence from the paint [42]

C Exact Solution of a 2D Airfoil

C.1 Conformal Mapping by Van de Vooren wing

To generate exact solution of the Tyrrell front wing, mapping from the airfoil on Y plane (physical plane $Y = x + iz$) to circle on f plane (virtual plane $f = g + ih$) is the first step. The mapping process is conformal mapping.

There are several numerical methods to do conformal mapping, Van de Vooren transformation as shown in Equation C.1, which are single domain conformal mapping.

$$Y = \frac{(f-a)^k}{(f-\varepsilon a)^{k-1}} + l, \tag{C.1}$$

where a is the radius of circle in f plane, ε is a thickness parameter, l determines chord length, and k controls the trailing edge angle τ as shown in Equation C.2 [45].

$$\tau = \pi(2-k) \tag{C.2}$$

The Van de Vooren transformation generates airfoils with finite trailing edge angle τ. For Tyrrell 026's front wing, $\tau = 0.0845\text{rad} = 4.839°$.

The result of conformal mapping by Van de Vooren transformation with different transition angles were shown in Figure C.1. Except for the surface near leading edge and trailing edge, the airfoil matches Tyrrell 026's front wing.

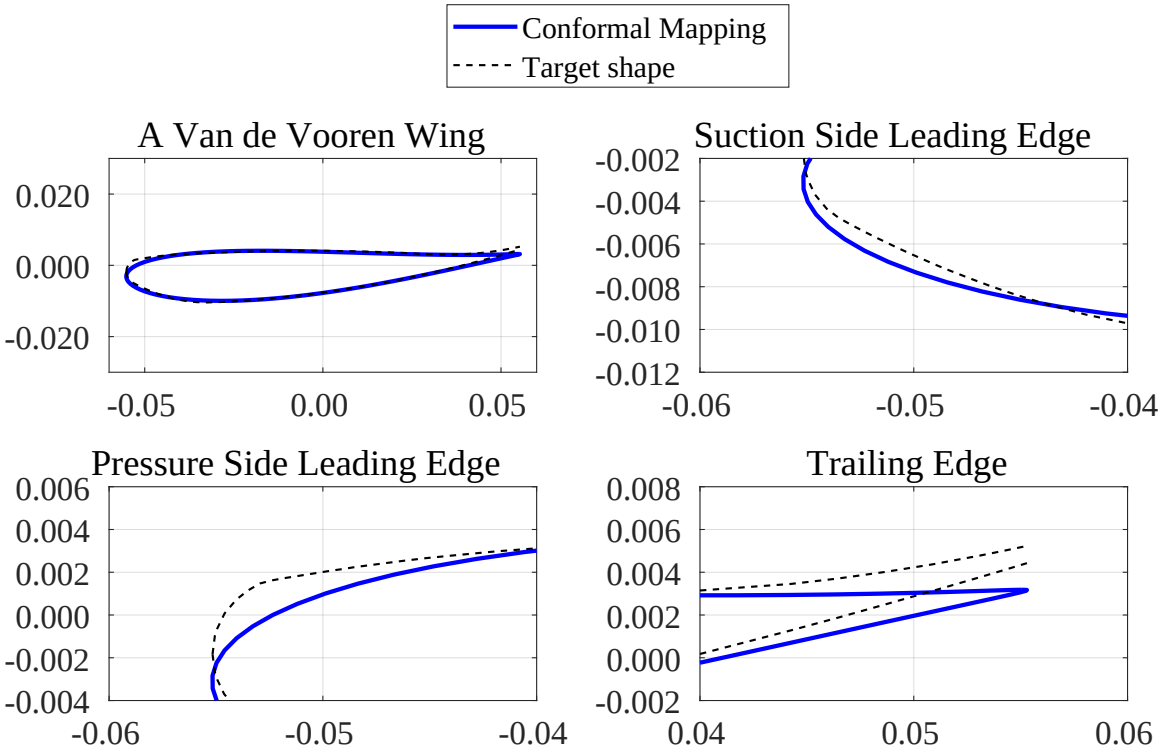

FIGURE C.1: An airfoil created by Van de Vooren transformation to match the profile of Tyrrell 026's front wing with $a = 0.0277\text{m}$, $R = 0.00297\text{m}$, $\varepsilon = -0.005$, $\tau = 0.0845\text{rad}$, and $\theta = \pi/8$. The length unit in this figure is m. The horizontal axis represents x axis in Y plane with the vertical axis represents z axis.

In addition to Joukowski transformation and Van de Vooren transformation, a method to do conformal mapping of doubly-connected domains was introduced by Crowdy & Marshall in 2006 as shown in Equation C.3 for any $\gamma \in f$ plane [46]. This transformation will transform annular to circular arc and ground.

$$Y = A\frac{P(f\overline{\gamma})}{P(f/\gamma)P(\overline{\gamma}) - P(1/\gamma)P(f\overline{\gamma})} + s, \tag{C.3}$$

where A is constant used to rotate or rescale the domain, s is constant used to shift the domain and $P(f)$ is prime function given by Crowdy in 2010 as shown in Equation C.4 [47],

$$P(f) = (1-f)\prod_{k=1}^{\infty}\left(1-q^{2k}f\right)\left(1-q^{2k}f^{-1}\right), \tag{C.4}$$

where q is the radius of inner circle of the annular in f plane.

As shown in Figure C.2, the Crowdy & Marshall transformation transform circle with unit radius to real axis as ground, and inner circle of the annular to circular arc.

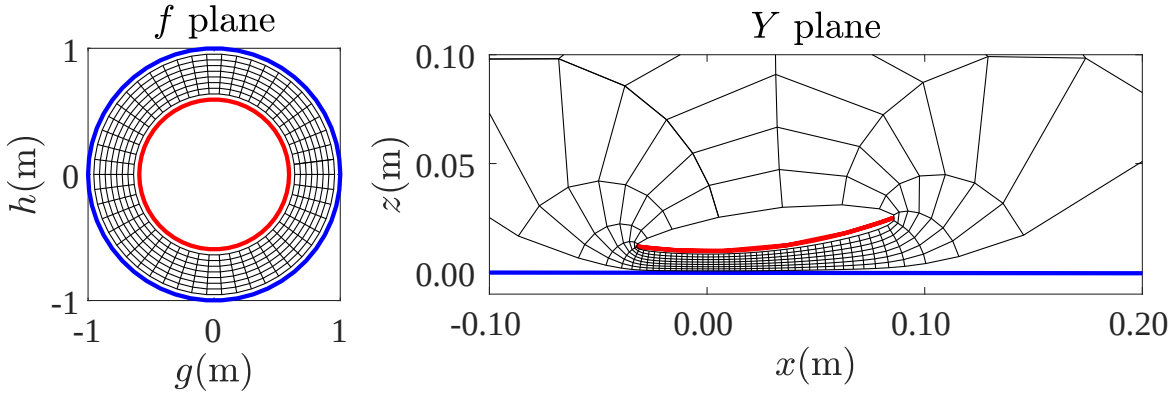

FIGURE C.2: Crowdy & Marshall transformation: mapping from annular (shown at left) to ground (real axis in blue) and a circular arc (red, shown at right), with $C = 0.118$m, $\alpha = -7.45°$ and $H = 0.009$m, $(H/C = 0.0763)$, where H is distance from wing to ground.

The numerical method of mapping a annular to ground and 2D certain wing needs further research.

C.2 A 3D correction of a wing's lift coefficient

In 3D case, circulation around the rectangular wing is not a constant, but a function of spanwise location [16]. The downforce for a inverse wing with ground effect has similar behavior to the downforce distribution of elliptic wing [13]. The lift force for a elliptic wing is calculated by Equation C.5,

$$L = \rho Q_\infty \int_{-b/2}^{b/2} \Gamma(y)\mathrm{d}y = \frac{\pi b}{4}\rho Q_\infty \Gamma_{\max}, \tag{C.5}$$

where b is spanwise location for the elliptic wing. For an untwisted elliptic planform with constant airfoil shape, the value of $\Gamma_{\max}$ is given by Equation C.6,

$$\Gamma_{\max} = \frac{2bQ_\infty(\alpha - \alpha_{L0})}{1 + 4b/m_0 C_0}, \tag{C.6}$$

where C_0 is the root chord, m_0 is the local lift slope.

C.3 Flow field prediction of a circular arc

The camber line of Joukowski wing is approximately circular arc. Flow field around circular arc should have similar behavior to flow field around Joukowski wing. In this section, flow field around a circular arc from camber line in the Joukowski wing as shown in Figure 2.2 is used to predict the

behavior of experimental flow field around Tyrrell 026's front wing. The transformation introduced in Equation C.3 is used to map the circular arc.

The complex potential for circulation and uniform flow around the circular arc mapped by Equation C.3 is calculated by Equation C.7 and Equation C.8 [48],

$$W_\Gamma(f) = \frac{\Gamma}{2\pi i}\log(f), \tag{C.7}$$

$$W_U(f) = f a_\infty \frac{P'(f)}{P(f)}, \tag{C.8}$$

where a_∞ is residue of the conformal map,

$$a_\infty = \frac{\gamma A P(\overline{\gamma})}{P'(1/\gamma)P(\overline{\gamma}) - |\gamma|^2 P'(\overline{\gamma})P(1/\gamma)}. \tag{C.9}$$

The complex potential for circulation and uniform flow around a Joukowski wing is calculated by Equation C.10 and Equation C.11 [16],

$$W_\Gamma(f) = \frac{i\Gamma}{2\pi}\log(f/a), \tag{C.10}$$

$$W_U(f) = Q_\infty\left(f + \frac{a^2}{f}\right). \tag{C.11}$$

The total complex potential is calculated by adding up complex potential by uniform flow and circulation.

$$W(f) = W_\Gamma(f) + W_U(f). \tag{C.12}$$

As shown in Figure C.3, with decreasing absolute value of negative circulation, the stagnation point around leading edge will move anti-clockwise. The density of streamline at suction side in Figure C.3a is higher than in Figure C.3b, means the velocity of flow is faster when the wing moves close to ground. The pressure is lower in this area. The downforce should be higher when the wing is close to the ground. The streamline in Figure C.3b should have less than 5% difference comparing with streamline around this circular arc in free stream. The streamline above ground is almost homogeneous in Figure C.3b. The density of streamline at pressure side is similar in both case. The pressure distribution should also be similar.

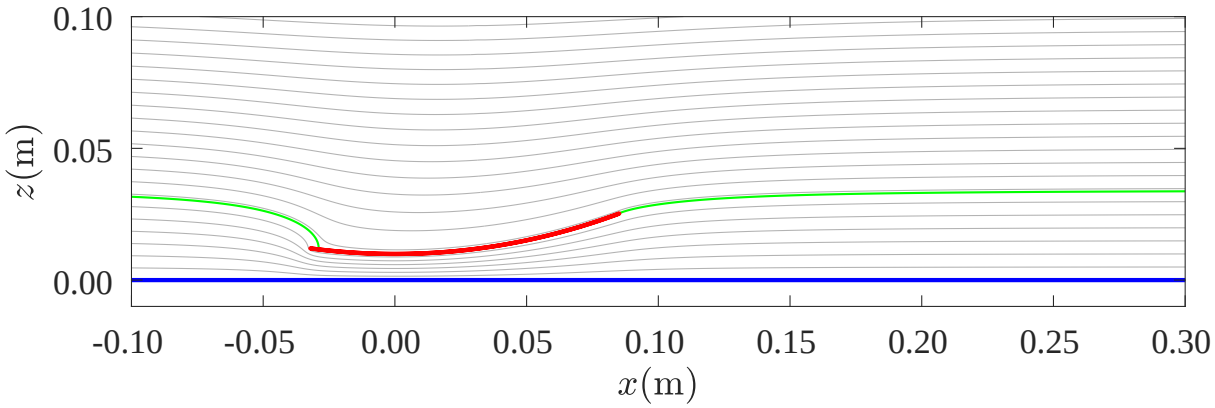

(a)

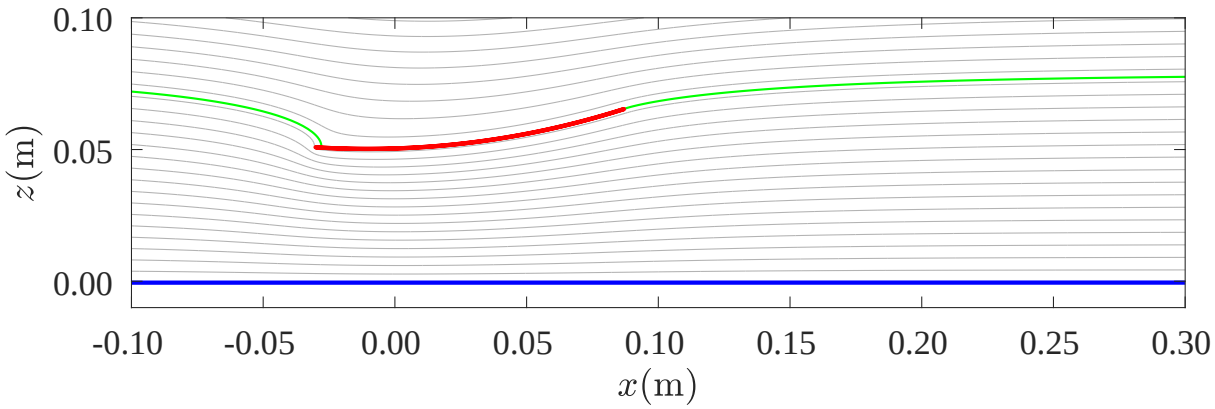

(b)

FIGURE C.3: Visualization of the flow field of exact solutions for ground effect for a circular arc at $\alpha = -7.45^\circ$ and different distance to ground. Streamlines are plotted in gray, the ground in blue, and the wings in red. The plots show uniform flow pass a circular arc with Kutta condition applied at the trailing edge a) at $H/C = 0.0763$, b) at $H/C = 0.4153$. The streamline corresponding to the wings is highlighted in green. The streamlines correspond to linearly spaced values of the streamfunction Ψ.

D Settings in 2D CFD simulation

TABLE D.1: Variables in SST $k-\omega$ viscous model.

RANS Model	**SST $k-\omega$**
Scale-Resovling Simulation options	**none**
Model Constants	**Value**
α^*_∞	1.00
α_∞	0.52
β^*_∞	0.09
a_1	0.31
β_i (Inner)	0.075
β_i (Outer)	0.083
TKE (Inner) Prandtl number	1.18
TKE (Outer) Prandtl number	1.00
SDR (Inner) Prandtl number	2.00
SDR (Outer) Prandtl number	1.17
Energy Prandtl number	0.85
Wall Prandtl number	0.85
Production limiter clip factor	10.00
Options	**Status**
Low-*Re* Corrections	off
Delayed DES	on
Viscous Heating	off
Curvature Correction	on
Corner flow Correction	off
Production Kato-Launder	off
Production limiter	on
Transition model	none
CCURV	constant, 1

TABLE D.2: Numerical methods used in SST $k-\omega$ CFD simulation.

Variable	**Method**
Pressure velocity coupling method	Coupled
Pressure velocity coupling flux	Rhie-Chow: momentum based
Spatial discrete gradient	Least Square Cell Based
Spatial discrete pressure	PRESTO!
Spatial discrete momentum	Second Order Upwind
Spatial discrete turbulent kinetic energy	Second Order Upwind
Spatial discrete specific dissipation rate	Second Order Upwind
Spatial discrete energy	Second Order Upwind
Transient formation	Second Order Implicit
Time discrete Warped Face Gradient Correction (WFGC)	On
Time discrete higher order relaxation	Flow variable, factor 0.75

TABLE D.3: Variables in DES viscous model.

RANS Model	**SST $k-\omega$**
Shielding Fuctions	**DDES**
Model Constants	**Value**
C_{des} (Inner)	0.78
C_{des} (Outer)	0.61
C_{d1}	20.00
α^*_∞	1.00
α_∞	0.52
β^*_∞	0.09
a_1	0.31
β_{i} (Inner)	0.075
β_{i} (Outer)	0.083
TKE (Inner) Prandtl number	1.18
TKE (Outer) Prandtl number	1.00
SDR (Inner) Prandtl number	2.00
SDR (Outer) Prandtl number	1.17
Energy Prandtl number	0.85
Wall Prandtl number	0.85
Production limiter clip factor	10.00
Options	**Status**
Low-*Re* Corrections	off
Delayed DES	on
Viscous Heating	off
Curvature Correction	on
Corner flow Correction	off
Production Kato-Launder	off
Production limiter	on
Transition model	none
CCURV	constant, 1

TABLE D.4: Numerical methods used in DES CFD simulation.

Variable	**Method**
Pressure velocity coupling method	Coupled
Pressure velocity coupling flux	Rhie-Chow: momentum based
Spatial discrete gradient	Least Square Cell Based
Spatial discrete pressure	PRESTO!
Spatial discrete momentum	Bounded Central Differencing
Spatial discrete turbulent kinetic energy	Second Order Upwind
Spatial discrete specific dissipation rate	Second Order Upwind
Spatial discrete energy	Second Order Upwind
BCD Scheme Boundedness	1
Transient formation	Second Order Implicit
Time discrete Warped Face Gradient Correction (WFGC)	On
Time discrete higher order relaxation	Flow variable, factor 0.75

TABLE D.5: Reference values used in SST $k-\omega$ and DES CFD simulation.

Variable	**Value**
Area(m^2)	0.06094
Density($\mathrm{kg\,m^{-3}}$)	998.2
Depth(m)	0.55
Entropy($\mathrm{J\,kg^{-1}}$)	0
Length(m)	0.1108
Pressure(Pa)	0
Temperature(K)	300
Velocity($\mathrm{m\,s^{-1}}$)	0.5
Kinematic Viscosity($\mathrm{kg\,m^{-1}\,s^{-1}}$)	0.001003
Specific heat ratio	1.4

E Repeatability in downforce measurement

A statistic analyze of downforce measurement was done at $\alpha = -6.60°$ and $H/C = 0.0763$. Free parameters were chosen to be waiting time between experiments T_{gap} and the distance to the side wall of tank d_{wall}.

As shown in Figure E.1, the measurement of downforce at steady phase with $T_{\text{gap}} < 1\text{min}$ has the mean value μ 0.8% larger, R.M.S.E. σ 72.7% larger than measurement with $T_{\text{gap}} > 15\text{min}$. The measurement is done at the middle of the tank, to reduce the wall effect. The σ value in this case corresponds to the uncertainty of single measurement. By repeating the experiment, the level of uncertainty should be reduced.

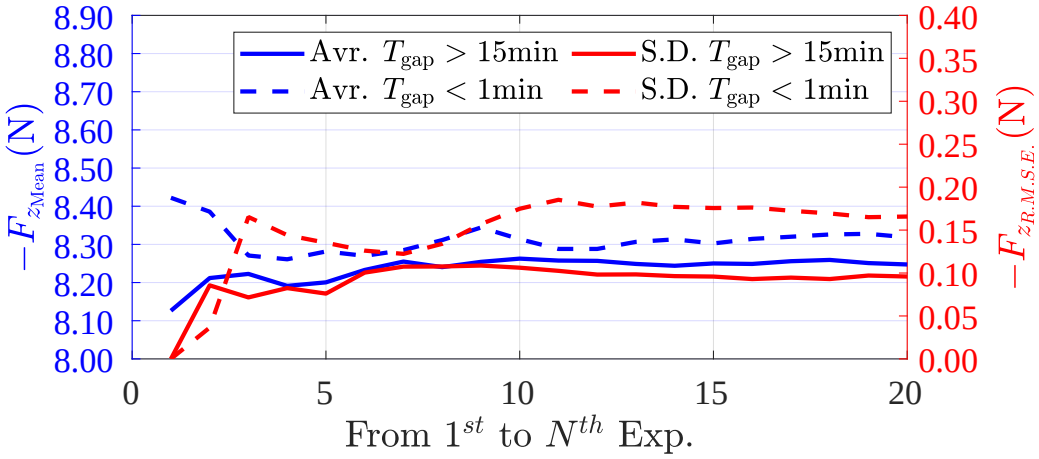

FIGURE E.1: Convergence of downforce at steady phase with increasing number of repeating experiments. 20 repeating experiments were done with $T_{\text{gap}} < 1\text{min}$. Same amount of experiments were done with $T_{\text{gap}} > 15\text{min}$. The expectation and standard deviation is taken in order of experiments. The mean and Root Mean Square Error (R.M.S.E.) calculated by Monte-Carlo method are used to represent expectation and standard deviation (uncertainty) in this case. The mean and R.M.S.E. with $T_{\text{gap}} < 1\text{min}$ convergence after 13 repeating. The mean and R.M.S.E. with $T_{\text{gap}} > 15\text{min}$ convergence after 7 repeating.

Take the mean and R.M.S.E. with 20 samples as the expectation and uncertainty, assuming the force measurement result obey normal distribution, 10000 downforce data was generated obeying the normal distribution to be a new data set. Randomly choose 10 samples out of the new data set, and take the mean of the 10 samples as the measurement result by repeating 10 measurements. Repeat this random process for 1000 times, 1000 measurement result by repeating the measurement for 10 times will be generated. The R.M.S.E σ of this 1000 measurement result represents the uncertainty of the mean value of repeating 10 measurements in a certain case.

As shown in Figure E.2, if the systematic error of 0.8% could be accepted, doing downforce measurement with $T_{\text{gap}} < 1\text{min}$ would have higher efficiency than with $T_{\text{gap}} > 15\text{min}$, and with lower uncertainty level. In this case, repeating experiment with $T_{\text{gap}} > 15\text{min}$ needs larger than 45 minutes with $\varepsilon = 4.2\%$. Repeating experiment with $T_{\text{gap}} < 1\text{min}$ needs less than 18 minutes with $\varepsilon = 2.9\%$.

As shown in Figure E.3, the measurement of downforce at steady phase with $d_{\text{wall}} = a$ has the mean value μ 1.2% larger, R.M.S.E. σ 34.1% smaller than measurement with $d_{\text{wall}} = b$. $d_{\text{wall}} = a$ was chosen to be at the middle of the tank, and $d_{\text{wall}} = b$ was chosen to be close to the side wall of the tank, which is easier to do PIV measurement. The waiting time between experiments was chosen to be $T_{\text{gap}} > 15\text{min}$, to reduce the uncertainty of each measurement.

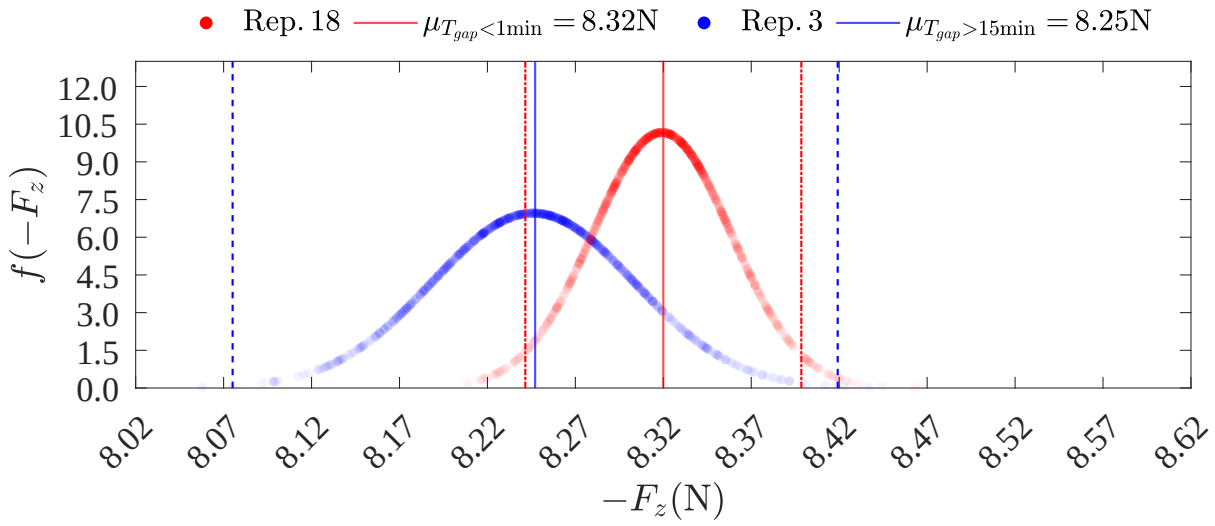

FIGURE E.2: Probability Density Function (PDF) of measured downforce. With repeating 20 times, $T_{\text{gap}} < 1\text{min}$ and repeating 3 times, $T_{\text{gap}} > 15\text{min}$, the confidence level is larger than 97.5% to assume $[\mu_{T_{\text{gap}}<1\text{min}} \pm 2\sigma_{T_{\text{gap}}<1\text{min}}] \subseteq [\mu_{T_{\text{gap}}>15\text{min}} \pm 3\sigma_{T_{\text{gap}}>15\text{min}}]$. The dash line represent the uncertainty of measurement results by $\mu \pm 3\sigma$ for $T_{\text{gap}} > 15\text{min}$. The dotted line represent the uncertainty of measurement results by $\mu \pm 2\sigma$ for $T_{\text{gap}} < 1\text{min}$. The red dotted line (for repeating 18 times with $T_{\text{gap}} < 1\text{min}$) are within the range of the blue ones (for repeating 3 times with $T_{\text{gap}} > 15\text{min}$).

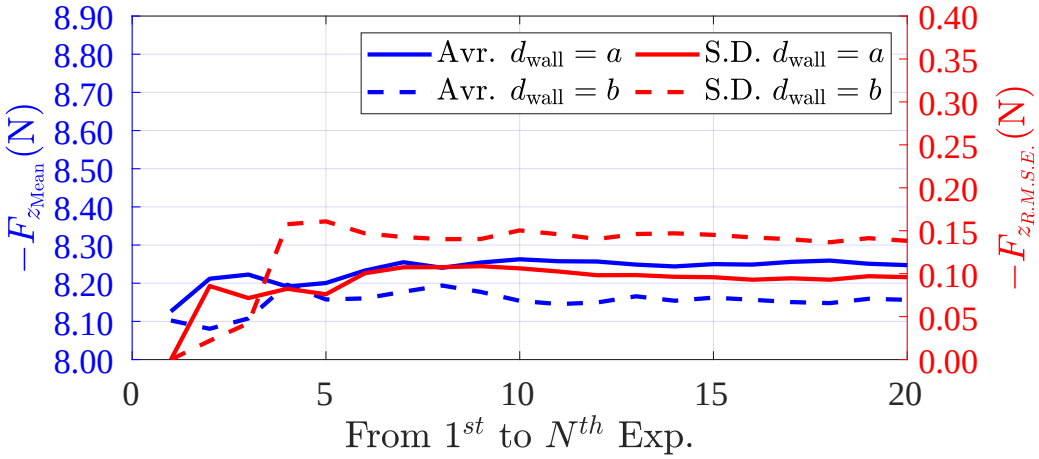

FIGURE E.3: Convergence of downforce at steady phase with increasing number of repeating experiments. 20 repeating experiments were done with $T_{\text{gap}} > 15\text{min}$ for each parameter. The expectation and standard deviation is taken in order of experiments. The mean and Root Mean Square Error (R.M.S.E.) calculated by Monte-Carlo method represent the expectation and standard deviation in this case. The mean and R.M.S.E. with $d_{\text{wall}} = a$ convergence after 7 repeating. The mean and R.M.S.E. with $d_{\text{wall}} = b$ convergence after 5 repeating.

F PIV results at different positions

As shown in Figure F.1, a difference on the vortex's structure can be found at the wake region of the wing and the non-dimensional circulation Γ^*. The difference represents a 3D flow structure around the wing. Information of the flow around the ground is missing due to the limit by perspective.

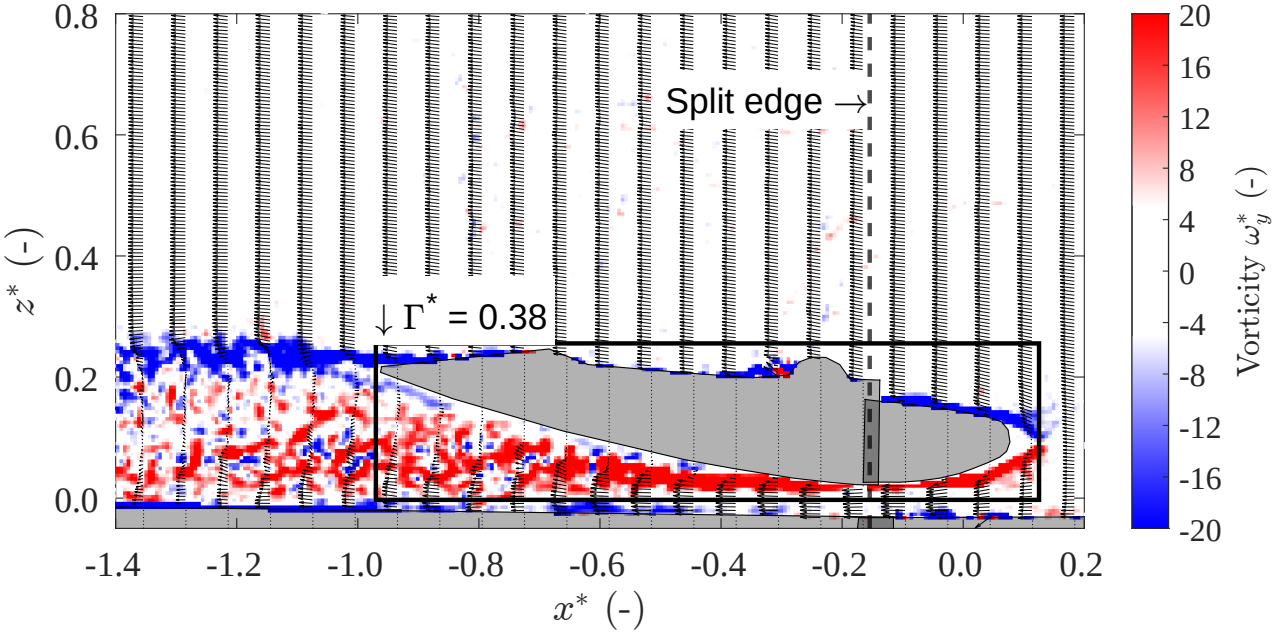

(a)

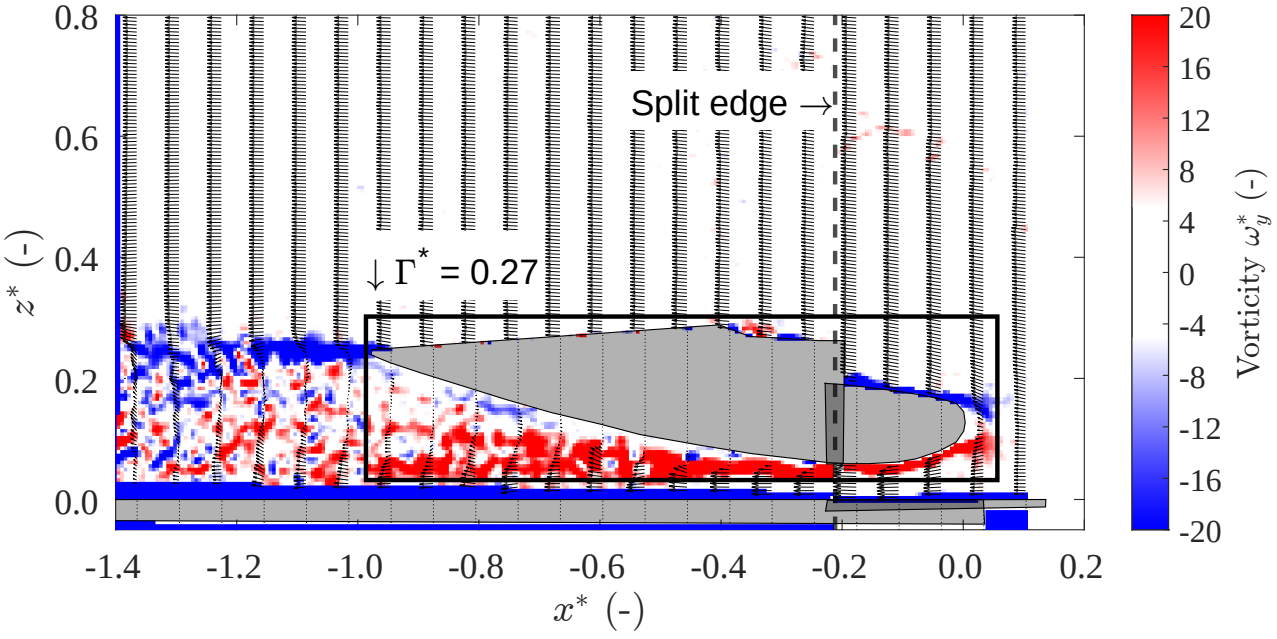

(b)

FIGURE F.1: A typical result of PIV measurement at (a) P_1 and (b) P_2, $H/C = 0.054$, $t^* = 6$, shown in non-dimensional coordinate. The origin point for z^* is set to be ground, and the origin point for x^* is set to be the leading edge of the wing. The circulation and vorticity are shown in non-dimensional form Γ^* and ω^* respectively.

References

[1] E. Preosti, "Data analysis for formula 1," *Berkeley Scientific Journal*, vol. 25, no. 2, 2021.

[2] T. Gasparetto, M. Orlova, and A. Vernikovskiy, "Same, same but different: analyzing uncertainty of outcome in formula one races," *Managing Sport and Leisure*, pp. 1–15, 2022.

[3] W. Toet, "Aerodynamics and aerodynamic research in formula 1," *The Aeronautical Journal*, vol. 117, no. 1187, pp. 1–26, 2013.

[4] J. Noble and M. Hughes, *Formula One racing for dummies*. John Wiley & Sons, 2003.

[5] A. Pandit and G. Day, "The aerodynamics of f1 car design: A survey and analysis," *Journal of Student Research*, vol. 10, no. 2, 2021.

[6] M. Racing. F1 playbook-for drifters, pacers and armchair racers. [Online]. Available: https://www.mclaren.com/racing/f1-playbook

[7] R. Smedley. Testing explained: Rob smedley on correlation, aero rakes and flow-vis paint. [Online]. Available: https://www.formula1.com/en/latest/article.testing-explained-rob-smedley-on-correlation-aero-rakes-and-flow-vis-paint.5UTaH1q9iuQcXVjZXui3Fz.html

[8] B. Chanetz, "A century of wind tunnels since eiffel," *Comptes Rendus Mécanique*, vol. 345, no. 8, pp. 581–594, 2017.

[9] J. Knapik, R. Gallyamov, V. Ovchinnikov, K. Volkova, and E. Avdeev, "F1 car-front wing cfd analysis and optimization," in *Information Technology and Nanotechnology*, 2018, pp. 1875–1884.

[10] C. Pathanadka, "Translationally accelerating wings in ground effect: A numerical study," *TUDelft Master Graduation Thesis*, 2022.

[11] E. Grift, M. Tummers, and J. Westerweel, "Hydrodynamics of rowing propulsion," *Journal of Fluid Mechanics*, vol. 918, 2021.

[12] E. Grift, N. Vijayaragavan, M. Tummers, and J. Westerweel, "Drag force on an accelerating submerged plate," *Journal of Fluid Mechanics*, vol. 866, pp. 369–398, 2019.

[13] J. Zerihan, "An investigation into the aerodynamics of wings in ground effect," Ph.D. dissertation, University of Southampton, 2001.

[14] C. Roy, F. Blottner, and J. Payne, "Bluff-body flow simulations using hybrid rans/les," in *33rd AIAA Fluid Dynamics Conference and Exhibit*, 2003, p. 3889.

[15] A. M. Alm-Eldien, A. F. A. Gawad, G. Hafaz, and E. M. G. Abd El Kreim, "Aerodynamic shape-optimization of axial-compressor blades," in *Eleventh Int. Conf. of Fluid Dynamics*, 2013, pp. 1–11.

[16] J. Katz and A. Plotkin, *Low-speed aerodynamics*. Cambridge university press, 2001, vol. 13.

[17] P. K. Kundu, I. M. Cohen, and D. R. Dowling, *Fluid mechanics*. Academic press, 2015.

[18] J. Katz, *Race car aerodynamics: designing for speed*. Bentley Publishers, 1995.

[19] M. Hepperle. Java foil users' guide. [Online]. Available: https://www.mh-aerotools.de/airfoils/java/JavaFoil%20Users%20Guide.pdf

[20] ——. Wing in ground proximity (wig). [Online]. Available: https://mh-aerotools.de/airfoils/jf_wig.htm

[21] C. E. Brennen. An internet book on fluid dynamics. [Online]. Available: http://brennen.caltech.edu/fluidbook/

[22] M. M. Mathis and D. J. Kerbyson, "A general performance model of structured and unstructured mesh particle transport computations," *The Journal of Supercomputing*, vol. 34, pp. 181–199, 2005.

[23] J. E. Matsson, *An introduction to ANSYS fluent 2022*. Sdc Publications, 2022.

[24] Helmholtz, "Xliii. on discontinuous movements of fluids," *The London, Edinburgh, and Dublin Philosophical Magazine and Journal of Science*, vol. 36, no. 244, pp. 337–346, 1868.

[25] P. Walker, "Experiments on the growth of circulation about a wing and an apparatus for measuring fluid motion," *Rep. Memo. Aeronaut. Res.(Great Britain)*, vol. 1402, 1931.

[26] L. The Black Market — KOYO Orient Japan Co. Musou black paint. [Online]. Available: https://www.the-black-market.com/marketplace/musou-black-paint/

[27] A. Savitzky and M. J. Golay, "Smoothing and differentiation of data by simplified least squares procedures." *Analytical chemistry*, vol. 36, no. 8, pp. 1627–1639, 1964.

[28] V. Raghav and N. Komerath, "Advance ratio effects on the flow structure and unsteadiness of the dynamic-stall vortex of a rotating blade in steady forward flight," *Physics of Fluids*, vol. 27, 01 2015.

[29] S.-H. Peng, P. Eliasson, and L. Davidson, "Examination of the shear stress transport assumption with a low-reynolds number k-omega model for aerodynamic flows," in *37th AIAA Fluid Dynamics Conference and Exhibit*, 2007, p. 3864.

[30] S. RAVI and S. NUMER, "P04731: Advanced vehicle dynamics," *Oxford Brookes University*, 2018.

[31] G. Stella. File:formula1 circuit catalunya 2021.svg. [Online]. Available: https://commons.wikimedia.org/wiki/File:Formula1_Circuit_Catalunya_2021.svg

[32] Hmdwgf. File:le mans circuit de la sarthe 1932-1967.png. [Online]. Available: https://commons.wikimedia.org/wiki/File:Le_Mans_Circuit_de_la_Sarthe_1932-1967.png

[33] N. Gao and X. Liu, "An improved smoke-wire flow visualization technique using capacitor as power source," *Theoretical and Applied Mechanics Letters*, vol. 8, no. 6, pp. 378–383, 2018.

[34] J. Radulović and G. Ocokoljić, "Flow visualization and aerodynamical coefficients determination for the lasta-95 model in the wind tunnel t-35," *Scientific Technical Review*, vol. 56, no. 2, pp. 63–69, 2006.

[35] H. Abitan, C. M. Velta, Y. Zhang, S. L. Ribergård, and J. S. Nielsen, "Development of an optical set-up for 3d piv with a large volume," in *14th International Symposium on Particle Image Velocimetry*, vol. 1, no. 1, 2021.

[36] M. Leonte, B. Wang, S. Socolofsky, S. Mau, J. Breier, and J. Kessler, "Using carbon isotope fractionation to constrain the extent of methane dissolution into the water column surrounding a natural hydrocarbon gas seep in the northern gulf of mexico," *Geochemistry, Geophysics, Geosystems*, vol. 19, no. 11, pp. 4459–4475, 2018.

[37] S. Ristić, "Flow visualization techniques in wind tunnels–optical methods (part ii)," *Scientific Technical Review*, vol. 57, no. 2, pp. 38–49, 2007.

[38] Y. Sugaya. Tuft testing at willow springs. [Online]. Available: https://pin.it/1TyKb6V

[39] L. Chen, T. Suzuki, T. Nonomura, and K. Asai, "Flow visualization and transient behavior analysis of luminescent mini-tufts after a backward-facing step," *Flow Measurement and Instrumentation*, vol. 71, p. 101657, 2020.

[40] S. Ristić, "Flow visualisation techniques in wind tunnels part i–non optical methods," *Scientific Technical Review*, vol. 57, no. 1, pp. 39–50, 2007.

[41] Y. Zhu, C. Lee, X. Chen, J. Wu, S. Chen, and M. Gad-el Hak, "Newly identified principle for aerodynamic heating in hypersonic flows," *Journal of Fluid Mechanics*, vol. 855, pp. 152–180, 2018.

[42] J. Gregory, K. Asai, M. Kameda, T. Liu, and J. Sullivan, "A review of pressure-sensitive paint for high-speed and unsteady aerodynamics," *Proceedings of the Institution of Mechanical Engineers, Part G: Journal of Aerospace Engineering*, vol. 222, no. 2, pp. 249–290, 2008.

[43] H. Sakaue, T. Tabei, and M. Kameda, "Hydrophobic monolayer coating on anodized aluminum pressure-sensitive paint," *Sensors and Actuators B: Chemical*, vol. 119, no. 2, pp. 504–511, 2006.

[44] C. E. Willert and M. Gharib, "Digital particle image velocimetry," *Experiments in fluids*, vol. 10, no. 4, pp. 181–193, 1991.

[45] A. van Vooren and L. de Jong, *Calculation of incompressible flow about aerofoils using source, vortex or doublet distributions*. Rijksuniversiteit Groningen, Mathematisch Instituut, 1970.

[46] D. Crowdy and J. Marshall, "Conformal mappings between canonical multiply connected domains," *Computational Methods and Function Theory*, vol. 6, pp. 59–76, 2006.

[47] D. Crowdy, "A new calculus for two-dimensional vortex dynamics," *Theoretical and Computational Fluid Dynamics*, vol. 24, pp. 9–24, 2010.

[48] P. J. Baddoo, M. Kurt, L. J. Ayton, and K. W. Moored, "Exact solutions for ground effect," *Journal of Fluid Mechanics*, vol. 891, p. R2, 2020.